

**TROPOSPHERIC EMISSION  
SPECTROMETER  
(TES)**

**LEVEL 2 ALGORITHM  
THEORETICAL BASIS  
DOCUMENT**

Version 1.15  
April 4, 2002

Jet Propulsion Laboratory  
California Institute of Technology  
Pasadena, California  
JPL D-16474

# TROPOSPHERIC EMISSION SPECTROMETER (TES)

## LEVEL 2 ALGORITHM THEORETICAL BASIS DOCUMENT

Reinhard Beer	Jet Propulsion Laboratory
Kevin W. Bowman	Jet Propulsion Laboratory
Patrick D. Brown	Atmospheric and Environmental Research Inc.
Shepard A. Clough	Atmospheric and Environmental Research Inc.
Annmarie Eldering	Jet Propulsion Laboratory
Aaron Goldman	University of Denver
Daniel J. Jacob	Harvard University
Michael Lampel	Raytheon
Jennifer A. Logan	Harvard University
Mingzhao Luo	Jet Propulsion Laboratory
Frank J. Murcray	University of Denver
Gregory B. Osterman	Jet Propulsion Laboratory
David M. Rider	Jet Propulsion Laboratory
Curtis P. Rinsland	NASA Langley Research Center
Clive D. Rodgers	University of Oxford
Stanley P. Sander	Jet Propulsion Laboratory
Mark Shepard	Atmospheric and Environmental Research Inc.
Susan Sund	Jet Propulsion Laboratory
Eugene Ustinov	Jet Propulsion Laboratory
Helen M. Worden	Jet Propulsion Laboratory
John Worden	Jet Propulsion Laboratory

---

Approved by:  
Reinhard Beer  
TES Principal Investigator

Version 1.16  
June 27, 2002

Jet Propulsion Laboratory  
California Institute of Technology  
Pasadena, California

## **TES Level 2 Algorithm Theoretical Basis Document**

---

This document was prepared at the Jet Propulsion Laboratory, California Institute of Technology, under a contract from the National Aeronautics and Space Administration

# TABLE OF CONTENTS

<b>TABLE OF CONTENTS</b>	<b>II</b>
<b>I LIST OF ACRONYMS</b>	<b>VI</b>
<b>II TES NOTATION AND STANDARD UNITS</b>	<b>VIII</b>
<b>III LIST OF FIGURES</b>	<b>XIII</b>
<b>IV LIST OF TABLES</b>	<b>XIII</b>
<b>1 INTRODUCTION</b>	<b>1</b>
<b>1.1 PURPOSE</b>	<b>1</b>
<b>1.2 SCOPE</b>	<b>1</b>
<b>1.3 APPLICABLE DOCUMENTS</b>	<b>1</b>
1.3.1 Controlling Documents	1
1.3.2 Project Reference Documents	1
<b>1.4 REVISION HISTORY</b>	<b>1</b>
<b>2 BACKGROUND</b>	<b>2</b>
<b>2.1 EXPERIMENT OBJECTIVES</b>	<b>2</b>
<b>2.2 RELEVANCE TO EARTH SYSTEM SCIENCE</b>	<b>3</b>
<b>2.3 INSTRUMENT CHARACTERISTICS</b>	<b>3</b>
<b>2.4 STANDARD PRODUCTS</b>	<b>4</b>
<b>2.5 SPECIES INCLUDED IN RETRIEVALS</b>	<b>8</b>
<b>3 ALGORITHM DESCRIPTION</b>	<b>13</b>
<b>3.1 ALGORITHM OVERVIEW</b>	<b>13</b>
3.1.1 TES Retrieval Algorithm: Earth Limb and Nadir Operational Retrieval (ELANOR)	14
<b>3.2 STATE VECTORS</b>	<b>16</b>

3.2.1	Terminology	16
3.2.2	Full State Vector Elements	16
3.2.3	Pressure Level Grids	17
3.2.4	Spectral Grids	18
<b>3.3</b>	<b>FORWARD MODEL: ATMOSPHERE</b>	<b>19</b>
3.3.1	Radiative Transfer	19
3.3.1.1	Ray Tracing and Path Integrals	21
3.3.1.2	Ray Tracing (Surface Layer)	21
3.3.1.3	Optical Depth	22
3.3.1.4	Atmospheric Radiance	22
3.3.1.5	Non-LTE	24
3.3.1.6	Radiative Transfer for the Solar Contribution	25
3.3.1.7	Surface Contribution	25
3.3.1.8	Simultaneous Multiple Rays	26
3.3.1.9	Horizontal Inhomogeneity	27
3.3.2	Surface Model	28
3.3.2.1	Surface Radiative Properties	28
3.3.2.2	Map of Earth Surface Composition	28
3.3.2.3	Digital Elevation Model	29
3.3.3	Radiative Transfer for Clouds and Aerosols	30
3.3.3.1	Radiative Transfer for Aerosol in Nadir View	31
3.3.3.2	Radiative Transfer with Scatterers in the Limb	31
3.3.4	Solar Source Function	32
3.3.5	Instrumental Line Shape Spectral Convolution and Apodization	33
3.3.6	Field-of-View Spatial Integration	34
3.3.7	Absorption Coefficient (ABSCO) Tables	38
3.3.7.1	ABSCO Table Generation (Using LBLRTM)	38
3.3.7.2	TES Line-by-Line Optical Depth Code	39
3.3.7.3	Cross-Section Code	41
3.3.7.4	Pressure Interpolation	41
3.3.8	ABSCO Databases	42
3.3.8.1	Line Parameters	42
3.3.8.2	Cross-Sections	42
3.3.8.3	Aerosols	44
3.3.8.4	CKD 3.0 Continuum	45
<b>3.4</b>	<b>JACOBIANS</b>	<b>46</b>
3.4.1	Finite Difference	46
3.4.2	Analytical	46
3.4.2.1	Temperature and Gas Concentrations	47
3.4.2.2	Surface and Opaque Cloud Boundary Properties	48
3.4.2.3	Pointing	48
<b>3.5</b>	<b>RETRIEVAL</b>	<b>49</b>
3.5.1	General Strategy	49

3.5.1.1	Strategy Table Selection	49
3.5.1.2	Target-level Suppliers	49
3.5.1.3	Step-level Suppliers	50
3.5.1.4	Operational Support Products	52
3.5.1.4.1	Initial Guess	52
3.5.1.4.2	Climatology	52
3.5.1.4.3	Meteorological Data	52
3.5.1.4.4	A priori Climatology Covariance Matrices	53
3.5.1.4.5	Microwindows	53
3.5.1.4.6	Land Characteristics and Surface Emissivity Properties Databases	53
3.5.1.4.7	Other OSP's	53
3.5.1.5	Retrieval Step Scenarios	53
3.5.1.6	Strategy for Limb Pointing Retrieval Limb	55
3.5.2	Retrieval Vectors	59
3.5.2.1	Introduction	59
3.5.2.2	Mapping	59
3.5.2.3	Initialization and Update of Retrievals with Maps	60
3.5.2.4	Nonlinear Maps based on natural log	61
3.5.3	A Priori Constraints	61
3.5.4	Inverse Algorithm	62
3.5.4.1	The additive noise model and cost function	62
3.5.4.2	Initial Guess Refinement	63
3.5.4.3	Numerical Solution	63
3.5.4.4	Convergence Criterion	65
3.5.5	Pixel Categorization for Nadir	65
3.5.6	Pixel Categorization in the Limb	67
3.5.7	Retrieval Microwindow Selection	67
3.5.8	Error Analysis	68
<b>3.6</b>	<b>FINAL FULL SPECTRUM CALCULATION</b>	<b>69</b>
<b>3.7</b>	<b>DATA QUALITY &amp; RESIDUALS</b>	<b>69</b>
3.7.1	Level 1A	69
3.7.2	Level 1B	71
3.7.3	Level 2	71
3.7.4	Level 3	72
3.7.5	Archiving	72
<b>4</b>	<b>ALGORITHM VERIFICATION</b>	<b>73</b>
<b>4.1</b>	<b>END-TO-END CLOSURE EXPERIMENTS</b>	<b>73</b>
<b>4.2</b>	<b>VALIDATION</b>	<b>73</b>
<b>5</b>	<b>REFERENCES</b>	<b>75</b>

THIS PAGE INTENTIONALLY LEFT BLANK.

## I LIST OF ACRONYMS

ABSCO	Absorption coefficient
ADEOS	Advanced Earth Observing Satellite
AER	Atmospheric and Environmental Research Inc.
AERI	Atmospheric Emitted Radiation Interferometer
AES	Airborne Emission Spectrometer
AIRS	Atmospheric Infrared Sounder
ARM	Atmospheric Radiation Measurements
ASTER	Advanced Spaceborne Thermal Emission and Reflection Radiometer
ATBD	Algorithm Theoretical Basis Document
ATMOS	Atmospheric Trace Molecule Spectrometer
CAMEX	Convection and Moisture Experiment
CART	Cloud and Radiation Test (site)
CDC	Climate Diagnostics Center
CFC	chlorofluorocarbon
CHEM	Chemistry Mission (EOS third spacecraft)
CKD	Clough, Kneizys, and Davies
DAAC	Distributed Active Archive Center
DAO	Data Assimilation Office
DEM	Digital Elevation Model
ECMWF	European Center for Medium Range Weather Forecasting
ENVISAT	ESA Environmental Satellite
EOS	Earth Observing System
ETOPO5	Global digital elevation model on a 5-minute grid
FEV	fraction of explained variance
FFT	Fast Fourier Transform
FOV	field of view
GTOPO30	Global digital elevation model on a 30-arc second grid produced by the U. S. Geological Survey's EROS Data Center in Sioux Falls, South Dakota
HCFC	Hydrogenated Chlorofluorocarbon
HDF	Hierarchical Data Format
HFC	Hydrogenated Fluorocarbon
HIS	High resolution Interferometric Sounder
HITRAN	The molecular spectroscopic database
ILS	instrument line shape
IMG	Interferometric Monitor of Greenhouse Gases
ISAMS	Improved Stratospheric and Mesospheric Sounder
JPL	Jet Propulsion Laboratory
LaRC	Langley Research Center
LBLRTM	Line By Line Radiative Transfer Model
LIMS	Limb Infrared Monitor of the Stratosphere

## TES Level 2 Algorithm Theoretical Basis Document

---

LOS	line of sight
LRIR	Limb Radiance Inversion Radiometer
MIPAS	Michelson Interferometer for Passive Atmospheric Sounding
NASA	National Aeronautics and Space Administration
NAST-I	NPOESS Aircraft Sounder Testbed – Interferometer
NMC/NCEP	National Meteorological Center/National Center for Environmental Prediction
NOAA	National Oceanic and Atmospheric Administration
OD	optical depth
SCF	Science Computing Facility
TES	Tropospheric Emission Spectrometer
TOA	top of atmosphere
TOVS	TIROS N Operational Vertical Sounder
UARS	Upper Atmosphere Research Satellite
VMR	volume mixing ratio

## II TES NOTATION AND STANDARD UNITS

### General

Both symbols and units are given in the lists below. The first column is the unit to be used in code, and in files unless there is good reason to use other (well documented) units. If other units are used in files, the data should be converted to the recommended unit on input. SI under the heading *docs* means any conventional SI unit, with standard prefixes for powers of  $10^3$ . Where no unit is given, the quantity is dimensionless.

		<i>code &amp; files</i>	<i>docs</i>
<b><u>Thermodynamics &amp; mass distribution</u></b>			
$T$	(level) temperature	K	SI
$\bar{T}$	layer mean temperature	K	SI
$P$	pressure	Pa	SI, hPa
$\bar{P}$	layer mean pressure	Pa	SI, hPa
$P_m$	partial pressure of gas g	Pa	SI, hPa
$\zeta$	log pressure parameter		
$\rho$	(mass) density	kg m <sup>-3</sup>	SI
$H$	pressure scale height	m	SI
$g$	acceleration due to gravity	m s <sup>-2</sup>	SI
$M_m$	molar mass of gas g	kg mole <sup>-1</sup>	SI
$q_m$	volume mixing ratio of gas g	fractional	*ppxv
$\bar{q}_m$	volume mixing ratio layer mean	fractional	*ppxv
			*x is m, b, t, etc.

**Geometry**

$z$	height	m	SI
$r$	radius from a center	m	SI
$R_e$	Earth radius to geoid	m	SI
$R_c$	Earth radius of curvature at geoid	m	SI
$R_s$	Earth center to satellite	m	SI
$R_{cs}$	Radius of curvature to satellite	m	SI
$\psi$	Angle at center of curvature between path element and tangent point	rad	deg
$\psi_s$	Angular position of satellite	rad	deg
$\phi$	latitude	rad	deg
$\lambda$	longitude	rad	deg
$\theta$	zenith angle of a ray	rad	deg
$s$	distance along ray	m	SI

**Indexing**

$i$	frequency index
$j,k$	level index
$l$	layer index

Levels indices are numbered 0 to N, bottom to top.  
Corresponding layers are numbered from 1 to N

**Spectroscopy**

$S$	line intensity	$\text{cm}^{-1} \text{ molec}^{-1} \text{ cm}^2$	$\text{cm}^{-1} \text{ molec}^{-1} \text{ cm}^2$
$f(\nu)$	line shape	$1/\text{cm}^{-1}$	$1/\text{cm}^{-1}$
$\chi_\nu$	spontaneous emission line shape	$1/\text{cm}^{-1}$	$1/\text{cm}^{-1}$
$\phi_\nu$	absorption and stimulated emission line shape	$1/\text{cm}^{-1}$	$1/\text{cm}^{-1}$
$\rho_n$	number density	$\text{molec cm}^{-3}$	SI
$\tilde{C}_s, \tilde{C}_f$	self and foreign continuum functions	$\text{cm}^{-1} \text{ molec}^{-1} \text{ cm}^2 \text{ atm}^{-1}$	

[Warning: the units recommended here are not SI because the HITRAN data base is not in SI.  
Care must be taken when combining them with other quantities.]

**Radiative Transfer**

$\nu$	wavenumber	$\text{cm}^{-1}$	$\text{cm}^{-1}$
$n$	refractive index		
$L$	spectral radiance	$\text{W m}^{-2} \text{sr}^{-1}/\text{cm}^{-1}$	$*\text{W m}^{-2} \text{sr}^{-1}/\text{cm}^{-1}$
$L^\uparrow$	up radiance, etc	$\text{W m}^{-2} \text{sr}^{-1}/\text{cm}^{-1}$	$*\text{W m}^{-2} \text{sr}^{-1}/\text{cm}^{-1}$
$\mathcal{F}$	flux	$\text{W m}^{-2}/\text{cm}^{-1}$	$*\text{W m}^{-2}/\text{cm}^{-1}$
$B$	Planck function	$\text{W m}^{-2} \text{sr}^{-1}/\text{cm}^{-1}$	$*\text{W m}^{-2} \text{sr}^{-1}/\text{cm}^{-1}$
$J$	source function	$\text{W m}^{-2} \text{sr}^{-1}/\text{cm}^{-1}$	$*\text{W m}^{-2} \text{sr}^{-1}/\text{cm}^{-1}$
$\tau_l$	optical depth of layer $l$		
$\mathcal{T}_l$	transmittance of layer $l$		
$\tau_{ik}$	optical depth of path from level $i$ to level $k$		
$\mathcal{T}_{ik}$	transmittance of path from level $i$ to level $k$		
$u_l$	layer amount (number)	$\text{molec m}^{-2}$	SI
$u_{il}$	column amount (number)	$\text{molec m}^{-2}$	SI
$\kappa_g$	absorption coefficient of gas $g$	$\text{m}^2 \text{molec}^{-1}$	SI
$\varepsilon$	emissivity		
$\alpha$	albedo		
$\mathcal{R}_{\text{BRDF}}$	Bidirectional Reflectance Distribution Function		
$\Phi$	Instrument line shape	$1/\text{cm}^{-1}$	$1/\text{cm}^{-1}$
$\mathcal{R}_{\text{FOV}}$	Field of view function	$\text{rad}^{-1}$	$\text{deg}^{-1}$
$r_L, r_u$	ratios of NLTE to LTE state populations		
$g_L, g_u$	state degeneracies for upper and lower states		
$n_L, n_u$	occupation numbers for upper and lower states		
$\Delta$	LTE vibrational Boltzmann factor		
$C_\nu$	Non-LTE correction function		
$R_\nu$	Volumetric radiation function	$\text{W m}^{-2} \text{sr}^{-1}/\text{cm}^{-1}$	$*\text{W m}^{-2} \text{sr}^{-1}/\text{cm}^{-1}$
		* with SI-style prefix ( $\square$ , m, etc)	

**Retrieval**

Matrices are upper case bold. Column vectors are lower case bold. Superscript T (e.g.  $A^T$ ) indicates transpose

- $\mathbf{x}_f$**  full state vector
- $\mathbf{x}$**  retrieval vector
  - $\mathbf{x}$  for retrieved  $\mathbf{x}$
  - $\hat{\mathbf{x}}_a$  for a priori
  - $\mathbf{x}_0$  for first guess
  - $\mathbf{x}_i$  for  $i$ 'th iteration

<b>y</b>	measurement vector
<b>e</b>	measurement error
<b>b</b>	forward model parameters
<b>F</b>	generic forward model
<b>S</b>	covariance matrices. Subscript determines which. – $S_e$ for <b>e</b> – $S_a$ for <b>x-x<sub>a</sub></b> – <b>S</b> for <b>x-x</b>
<b>K</b>	Jacobian
<b>A</b>	averaging kernel
<b>G</b>	Kalman gain (contribution function)
<b>I<sub>n</sub></b>	unit matrix (order <i>n</i> optional)
<b>O<sub>n</sub></b>	zero matrix (order <i>n</i> optional)
$\sigma$	standard deviation
$z_r$	correlation length
<b>C</b>	cost function

**Physical constants**

$k_B$	Boltzmann constant
$c$	speed of light
$h$	Planck constant
$N$	Avagadro constant
$\sigma$	Stefan-Boltzmann constant
$c_1$	First radiation constant
$c_2$	Second radiation constant
$R$	Molar gas constant

THIS PAGE INTENTIONALLY LEFT BLANK.

### III LIST OF FIGURES

Figure 3-1: TES Level 2 Retrieval Flow	15
Figure 3-2: Illustration of the recursive radiative transfer calculations	23
Figure 3-3: Fit to sea water emissivity [Masuda <i>et al</i> , 1988] using a double dispersion curve (private communication, Clough, S.A., AER) shown with the tabulated emissivities that are interpolated for computing ocean surface radiances in the TES forward model.	29
Figure 3-4: Monochromatic solar spectrum over the spectral region relevant to TES (Kurucz, 1995).	33
Figure 3-5: Diagram for TES pointing geometry and FOV convolution in limb mode	37
Figure 3-6: Observed HIS spectrum and LBLRTM calculated results in equivalent brightness temperature for CAMEX case (a) and observed-calculated differences (b). The nadir measurement was taken from 20 km on the NASA ER2.	40
Figure 3-7: Supplier Dependencies	51
Figure 3-8: AFGL Mid Latitude Summer Profiles	57

### IV LIST OF TABLES

Table 2-1: TES Filter Bandpasses	3
Table 2-2: TES Global Survey Filters	4
Table 2-3: TES Standard Products	5
Table 2-4: TES Product Reporting Levels [= UARS Standard Levels]	7
Table 2-5: Format for Reporting TES Retrievals	8
Table 2-6: HITRAN Line List Species Used by TES	8
Table 2-7: HITRAN Cross-Section Species Used by TES	11
Table 2-8: Additional Cross-Section Species Needed by TES	12
Table 3-1: Operational spectral grid for TES filters	19
Table 3-2: Resolution and suggested forward model extension values.	34
Table 3-3: IR cross-section data prepared for TES	43
Table 3-4: Sample Retrieval Step Scenarios	54
Table 3-5: Retrieval results for temperature and tangent point for central ray of pixel 11 with TES FOV (tangent height = 11.5 km).	57
Table 3-6: Quantities related to the ray trace from the tangent point to the satellite as a function of tangent height. Refraction is included in the ray trace.	58

**Error! No table of figures entries found.**

THIS PAGE INTENTIONALLY LEFT BLANK

# 1 INTRODUCTION

## 1.1 PURPOSE

This Algorithm Theoretical Basis Document (ATBD) describes the algorithms used to retrieve all Tropospheric Emission Spectrometer (TES) Standard Data Products. These products are scheduled to be archived at the NASA Langley Research Center (LaRC) Distributed Active Archive Center (DAAC) <http://eosdis.larc.nasa.gov>. The standard products consist of vertical volume mixing ratio profiles of ozone, water vapor, carbon monoxide, methane, nitric oxide, nitrogen dioxide and nitric acid and their associated error estimates. Note that all products are retrieved near-simultaneously through a common process and are therefore discussed jointly rather than individually.

This document identifies the following: sources of input data that are required for the retrievals; provides the physical theory and mathematical background underlying the use of this information in the retrievals; describes practical considerations affecting algorithm development; and outlines a test and validation approach.

## 1.2 SCOPE

This document covers the algorithm theoretical basis for the parameters to be included in the TES Data Products at or near launch time. Only parameters that are to be routinely retrieved at the DAAC are discussed. On-going development and prototyping efforts may result in modifications to parts of certain algorithms. Only the algorithms that are implemented at the DAAC for routine processing of TES data will be preserved in the final release of this document. However, certain materials deemed too detailed for the main body of the document may be found in the Appendices, which are numerically keyed to their relevant sub-sections.

## 1.3 APPLICABLE DOCUMENTS

### 1.3.1 Controlling Documents

1) *Mission to Planet Earth Strategic Enterprise Plan 1998-2002*. NASA HQ MTPE, Oct 1998.  
<http://www.earth.nasa.gov/visions/stratplan/index.html>

2) *Execution Phase Project Plan for the Earth Observing System (EOS)*. GSFC 170-01-01, Rev. A, May 1995.

### 1.3.2 Project Reference Documents

*Tropospheric Emission Spectrometer: Scientific Objectives & Approach, Goals & Requirements*. JPL D-11294, Rev. 5.0, May 1996.

## 1.4 REVISION HISTORY

The original version (1.0) of this document was dated January 29, 1999.

## 2 BACKGROUND

### 2.1 EXPERIMENT OBJECTIVES

The Tropospheric Emission Spectrometer (TES), selected for flight on the EOS CHEM I mission, will provide the first global view of the chemical state of the troposphere (the lowest region of the atmosphere, extending from the surface to about 10-15 km altitude). The investigation will focus on mapping the global distribution of tropospheric ozone and on understanding the factors that control ozone concentrations.

Ozone is produced in the troposphere by photochemical oxidation of carbon monoxide (CO) and hydrocarbons in the presence of nitrogen oxides (NO<sub>x</sub>) and water vapor. These ozone precursors have both natural and anthropogenic sources. The chemistry of ozone is complex and tightly coupled to the atmospheric transport of both ozone and the precursors.

Tropospheric ozone has three major environmental impacts:

- 1) AS AN AIR POLLUTANT. Ozone in surface air is toxic to humans, animals and vegetation. It is the principal harmful component of smog.
- 2) AS A CLEANSING AGENT. Photolysis of ozone in the presence of water vapor is the primary source of the hydroxyl radical (OH), which is the main oxidant in the atmosphere. Reactions with OH in the lower and middle troposphere are the principal sink for a large number of environmentally-important species including air pollutants (carbon monoxide), greenhouse gases (methane), and gases depleting the stratospheric ozone layer (HCFC's, methyl halides).
- 3) AS A GREENHOUSE GAS. Ozone in the middle and upper troposphere is an efficient greenhouse gas. Perturbation of ozone in this region of the atmosphere results in heterogeneous radiative forcing with complicated implications for climate.

The troposphere contains only about 10% of the total ozone in the atmosphere -the bulk is in the stratosphere. The environmental implications of tropospheric ozone are very different from those of stratospheric ozone. The ozone layer in the stratosphere shields the Earth's surface from solar UV-B radiation, and thinning of this layer as a result of human activities is a matter of grave concern. Tropospheric ozone, by contrast, has increased as a consequence of human activity (primarily because of combustion processes). Whether this increase in tropospheric ozone is beneficial (cleansing agent) or harmful (air pollutant, greenhouse gas) depends to a large extent on its altitude. It is very important, therefore, to map the global 3-dimensional distribution of tropospheric ozone and its precursors in order to improve our understanding of the factors controlling ozone in different regions of the troposphere.

The specific Standard Products that TES will produce are global-scale vertical concentration profiles (0 - ~33 km) of ozone, water vapor, carbon monoxide, methane, nitric oxide, nitrogen dioxide and nitric acid (the latter 3 in the mid- and upper troposphere only). Essential by-products of the analysis are atmospheric temperature profiles and surface temperature and emissivity.

## 2.2 RELEVANCE TO EARTH SYSTEM SCIENCE

One of the primary EOS themes is ‘Atmospheric Ozone Research.’ TES directly addresses this theme.

## 2.3 INSTRUMENT CHARACTERISTICS

TES is an infrared, high resolution, Fourier Transform spectrometer covering the spectral range 650 - 3050  $\text{cm}^{-1}$  (3.3 - 15.4  $\mu\text{m}$ ) at a spectral resolution of 0.1  $\text{cm}^{-1}$  (nadir viewing) or 0.025  $\text{cm}^{-1}$  (limb viewing). The two observation modes are essential because many of the spectral features that TES observes are very weak (especially the nitrogen oxides) and limb-viewing markedly enhances their measurability (with the deficiency that cloud interference is much more likely than in nadir viewing, where TES has relatively good spatial resolution).

In order to improve signal-to-noise ratio and improve collection efficiency, TES is (as far as possible) radiatively cooled to  $\sim 180\text{K}$ , and it divides the spectral range into 4 sub-regions, each observed with a separate 1x16 array of detectors (identified as 1A, 1B, 2A, and 2B) actively cooled to 65K. The bandwidth is further restricted to  $\sim 250 \text{ cm}^{-1}$  by interchangeable filters. With these arrays, 16 altitudes in the troposphere and lower stratosphere are observed simultaneously with a height separation of 2.3 km or, alternatively, 16 contiguous areas (each 0.5 x 5 km) are observed on the ground. Table 2-1 shows the available filter ranges and their identifiers. A complete description of TES can be found as an appendix to the L1B ATBD [JPL D-16479, Oct.1 1999].

**Table 2-1: TES Filter Bandpasses**

Filter ID	Lower 50% Point, $\text{cm}^{-1}$	Upper 50% Point, $\text{cm}^{-1}$
1A1	1900	2250
1A2	2200	2450
1A3	2425	2650
1A4	2600	2850
1A5	2800	3050
1B1	820	1050
1B2	950	1150
2A1	1100	1325
2A2	1300	1550
2A3	1500	1750
2A4	1700	1950
2B1	650	900

Note: Any combination of 1Ax, 1By, 2Az and 2B1 is allowable (1 per detector array) with the proviso that, normally, only limited switching among 1Ax and 2Az filters can occur between successive scans. The actual arrangement of the filters in the filter wheels has been optimized for expected observation scenarios.

## TES Level 2 Algorithm Theoretical Basis Document

The filters actually employed for the Global Surveys are shown in Table 2-2. Sequences “A” and “B” alternate every 81.2 seconds for 58 orbits (4 days) for a total of 4234 sequences (= no. of profile sets). Note also that the pairs of nadir observations in each sequence are co-located.

**Table 2-2: TES Global Survey Filters**

Sequence	Scan No.	Type	Array 1A	Array 1B	Array 2A	Array 2B
A	1	Space	1A1	1B1	2A2	2B1
A	2	Black Body	1A1	1B1	2A2	2B1
A	3	Nadir	1A1	1B2	2A2	2B1
A	4	Nadir	1A1	1B2	2A2	2B1
A	5	Limb	1A1	1B1	2A2	2B1
A	6	Limb	1A1	1B2	2A4	2B1
A	7	Limb	1A1	1B2	2A4	2B1
B	1	Space	1A1	1B2	2A2	2B1
B	2	Black Body	1A1	1B2	2A4	2B1
B	3	Nadir	1A1	1B2	2A4	2B1
B	4	Nadir	1A1	1B2	2A2	2B1
B	5	Limb	1A1	1B1	2A2	2B1
B	6	Limb	1A1	1B2	2A4	2B1
B	7	Limb	1A1	1B2	2A4	2B1

In the limb mode, TES measures the infrared thermal emission from the atmosphere. In the nadir mode, the measurement is of the surface emission, downward directed atmospheric emission scattered from the surface, and further emission and absorption by the atmosphere. In a limited spectral range, under sunlit conditions, there may also be solar radiation scattered from the atmosphere and the surface.

TES obtains its data in 4 seconds (nadir) or 16 seconds (limb) plus calibrations in a sequence: 2 calibrations followed by 2 nadir observations followed by 3 limb observations. The entire cycle requires 81.2 seconds and is repeated continuously for four days out of eight, interspersed with major calibration-only sequences (essential for this type of instrument) and occasional targets-of-opportunity such as volcanic eruptions, biomass burning regions or regional ozone episodes for which TES has unique capabilities (but note that these are Special, not Standard, Products and are not further considered in this document).

It is a property of a Fourier Transform Spectrometer that it must be used in a so-called ‘staring’ mode (that is, the target location or altitude must be tracked). Accordingly, TES is equipped with a precision pointing system.

### 2.4 STANDARD PRODUCTS

TES Standard Products (and their data sources) are shown in Table 2-3.

Table 2-3: TES Standard Products

Product	Nadir	Limb
Atmospheric Temperature, T	√	√
Surface Temperature, T <sub>s</sub>	√	
Land Surface Emissivity	√	
Ozone (O <sub>3</sub> ) VMR	√	√
Water Vapor (H <sub>2</sub> O) VMR	√	√
Carbon Monoxide (CO) VMR	√	√
Methane (CH <sub>4</sub> ) VMR	√	√
Nitric Oxide (NO) VMR		√
Nitrogen Dioxide (NO <sub>2</sub> ) VMR		√
Nitric Acid (HNO <sub>3</sub> ) VMR		√

Standard Products will be reported at the pressure levels shown in Table 2-4 (note that the corresponding altitudes are approximate). Nadir and limb data are nearly co-located.

For each species, at each level, the reported parameters will be as shown in. The meaning of the last 5 columns is the following:

*Volume Mixing Ratio* (VMR,  $q$ ) is reported with respect to dry air to avoid the problem that the H<sub>2</sub>O VMR can be large enough to effect the overall result.

*Random Errors* are the square roots of the diagonal elements of the output error covariance matrix (i.e., the  $1\sigma$  values). The full matrix is also available.

*Systematic Errors* are estimated from reported errors in, for example, the HITRAN database.

*Fraction of Explained Variance* (FEV) is a measure of how much the measurements improve upon the *a priori* data (see 3.5.9 for a detailed explanation). If the FEV = 1 then all the information comes from the data. If the FEV = 0 then no information comes from the data.

*Correlation Length* ( $z_r$ ) is a measure of the dependence of adjacent (or nearby) retrieval levels (see 3.5.9). If  $z_r \ll$  the distance between adjacent levels then the values are independent. If  $z_r \geq$  the distance between adjacent levels then the values are not independent.

Each such file will be accompanied by a header containing information such as the time, date, latitude, longitude, and solar zenith angle at acquisition, plus a set of data quality indicators.

**Table 2-4: TES Product Reporting Levels [= UARS Standard Levels]**

<b>Index</b>	<b>Pressure hPa</b>	<b>US S.A. Altitude km</b>	<b>Delta Altitude km</b>
0	1000.0	0.100	
1	681.3	3.175	3.075
2	464.2	6.100	2.925
3	316.2	8.825	2.725
4	215.4	11.350	2.525
5	146.8	13.800	2.450
6	100.0	16.200	2.450
7	68.1	18.650	2.450
8	46.4	21.100	2.500
9	31.6	23.600	2.500
10	21.5	26.100	2.500
11	14.7	28.600	2.600
12	10.0	31.200	2.600
13	6.8	33.800	2.600
14	4.6	36.600	2.800

“Delta Altitude” at level  $i$  is the difference between Level  $i$  and Level  $i-1$

**Table 2-5: Format for Reporting TES Retrievals**

Species	Volume Mixing Ratio w.r.t Dry Air ( <i>q</i> )	Estimated Random Error ( $1\sigma$ )	Estimated Systematic Error	Fraction of Explained Variance (FEV)	Correlation Length <i>z<sub>r</sub></i> , km
---------	---	---	----------------------------------	---	--

## 2.5 SPECIES INCLUDED IN RETRIEVALS

In order to retrieve the Standard Products listed in Table 2-3, it is necessary to account for many more species in the process. These are often called “interferents” but, in fact, some will be retrieved as controls (e.g., N<sub>2</sub>O), some flagged for Special Processing (e.g., heavy hydrocarbons) and some fixed. For example, in order to retrieve HNO<sub>3</sub>, it is essential to include both CCl<sub>3</sub>F (CFC11) and CCl<sub>2</sub>F<sub>2</sub> (CFC12) whose bands overlap the nitric acid signature.

The primary source of spectral information is the HITRAN database [Rothman *et al.*, 1998]. Not all of the species in the list are pertinent to TES but those that are, are shown in Table 2-6 (line data) and (cross-section data). In addition, some modifications and additions to the list are discussed elsewhere in this document and it should be noted that certain isotopomers *must* be treated as separate molecules because their concentrations relative to the parent are known to be height-variable (HITRAN assumes a fixed ratio). Finally, Table 2-8 lists some species that are likely to be important to TES but for which little or no useful spectral data are available (i.e., they are candidates for laboratory study in the very near future).

**Table 2-6: HITRAN Line List Species Used by TES**

HITRAN [TES] Index No.	Molecule	Comments
1	H <sub>2</sub> O	HDO & H <sub>2</sub> <sup>17</sup> O Separated
[1a]	HDO	
[1b]	H <sub>2</sub> <sup>17</sup> O	
2	CO <sub>2</sub>	
3	O <sub>3</sub>	<sup>16</sup> O <sup>17</sup> O <sup>16</sup> O & <sup>17</sup> O <sup>16</sup> O <sup>16</sup> O Separated
[3a]	<sup>16</sup> O <sup>17</sup> O <sup>16</sup> O	

**TES Level 2 Algorithm Theoretical Basis Document**

---

<b>HITRAN [TES] Index No.</b>	<b>Molecule</b>	<b>Comments</b>
[3b]	$^{17}\text{O}^{16}\text{O}^{16}\text{O}$	
4	$\text{N}_2\text{O}$	
5	$\text{CO}$	
6	$\text{CH}_4$	$\text{CH}_3\text{D}$ Separated
[6a]	$\text{CH}_3\text{D}$	
7	$\text{O}_2$	
8	$\text{NO}$	
9	$\text{SO}_2$	
10	$\text{NO}_2$	
11	$\text{NH}_3$	
12	$\text{HNO}_3$	
13	$\text{OH}$	
14	(HF)	** Not Used **
15	$\text{HCl}$	
16 **	(HBr)	** Not Used **
17 **	(HI)	** Not Used **
18	$\text{ClO}$	
19	$\text{OCS}$	

**TES Level 2 Algorithm Theoretical Basis Document**

---

<b>HITRAN [TES] Index No.</b>	<b>Molecule</b>	<b>Comments</b>
20	HCOH	
21	HOCl	
22	N <sub>2</sub>	
23	HCN	
24	CH <sub>3</sub> Cl	
25	H <sub>2</sub> O <sub>2</sub>	
26	C <sub>2</sub> H <sub>2</sub>	
27	C <sub>2</sub> H <sub>6</sub>	
28 **	(PH <sub>3</sub> )	** Not Used **
29	COF <sub>2</sub>	
30	SF <sub>6</sub>	Also need X-sections
31	H <sub>2</sub> S	
32	HCOOH	
33 **	(HO <sub>2</sub> )	** Not Used **
34 **	(O)	** Not Used **
35	ClONO <sub>2</sub>	Also need X-sections
36 **	(NO <sup>+</sup> )	** Not Used **
37 **	(HOBr)	** Not Used **

**Table 2-7: HITRAN Cross-Section Species Used by TES**

Molecule	Common Name
CCl <sub>4</sub>	Carbon Tetrachloride
CCl <sub>3</sub> F	CFC-11
CCl <sub>2</sub> F <sub>2</sub>	CFC-12
CClF <sub>3</sub>	CFC-13
CF <sub>4</sub>	CFC-14
CHCl <sub>2</sub> F	HCFC-21
CHClF <sub>2</sub>	HCFC-22
C <sub>2</sub> Cl <sub>3</sub> F <sub>3</sub>	CFC-113
C <sub>2</sub> Cl <sub>2</sub> F <sub>4</sub>	CFC-114
C <sub>2</sub> ClF <sub>5</sub>	CFC-115
N <sub>2</sub> O <sub>5</sub>	Dinitrogen Pentoxide
HO <sub>2</sub> NO <sub>2</sub>	Peroxynitric Acid*
SF <sub>6</sub>	Sulfur Hexafluoride
ClONO <sub>2</sub>	Chlorine Nitrate

\* Seriously incomplete

**Table 2-8: Additional Cross-Section Species Needed by TES**

Molecule	Common Name
$C_6H_6$	Benzene
$C_2H_4$	Ethylene
$C_3H_8$	Propane
$CH_3C(O)CH_3$	Acetone
$CH_3OH$	Methyl Alcohol
$CH_3C(O)NO_2$	Peroxyacetyl Nitrate (PAN)
$HO_2NO_2$	Peroxynitric Acid*
$CH_3COOH$	Acetic Acid
$CH_3OOH$	Methyl Hydroperoxide

\* For bands not in HITRAN

## 3 ALGORITHM DESCRIPTION

### 3.1 ALGORITHM OVERVIEW

TES standard data processing falls naturally into 3 groups:

- 1) At Level 1A the raw data from the spacecraft are decommutated and the instrument outputs (called *interferograms*) reconstructed. File headers also contain important ancillary data such as time, date, spacecraft and target location, and instrument pointing. The target location is determined by a geolocation algorithm at Level 1A that uses the instrument pointing and spacecraft coordinates along with the Digital Elevation Model (DEM) and earth ellipsoid and geoid models.
- 2) At Level 1B, the interferograms are converted to spectra, radiometrically-calibrated and resampled onto a common frequency grid. Certain data quality flags are added to the header at this juncture and the results passed to Level 2 [JPL D-16479, 1999].
- 3) At Level 2, vertical concentration profiles of the selected species are extracted from the data through the process of *retrieval* that is the topic of this document.

Although this document is primarily concerned with standard products, we also expect to use the same algorithm for special products so we have retained generality in some sections to support these additional functions. This additional functionality will be maintained in the Reference Forward Model. We therefore describe the deliverable version as the Operational Forward Model.

Figure 3-1 shows an overall flow chart for the forward model and retrieval process.

In Global Survey mode, observations are made in sequences made up of calibration scans, two nadir observations and three limb observations. Observation sets may be binned together to be processed in batches containing all observations made each day at the same time after an equator crossing, i.e. at the same latitude. This would enable savings to be made in disk accesses for quantities that depend on latitude only. This includes climatological information used for the first guess and *a priori* information, which are likely to be zonally averaged.

Each observation set will be retrieved in several stages, with each stage using a selection of the results of a previous stage as *a priori*, or as a first guess, or as updated forward model parameters, as appropriate. For example, in both the nadir and the limb retrievals, temperature could be retrieved first, and the results used as forward model parameters for constituent retrievals. Although we will perform the retrievals using spectral ranges (referred to as ‘microwindows’) that are selected to minimize the errors from ‘interferent’ species on the retrieved parameters, we must still account for these interferences. Thus, the constituent retrievals will be carried out in an appropriate order so that an already retrieved quantity can be included as a forward model parameter (‘interferent’) for subsequent retrievals. Some quantities may be

retrieved jointly. In particular, the final profile for the temperature and water vapor fields will be obtained from a joint retrieval.

Each retrieval will use the same inverse algorithm comprising the following stages:

- (1) Full state vector construction for generating the forward model, including initial guess for retrieved parameters
- (2) *a priori* vector and covariance, or other constraint construction;
- (3) optimal estimate by numerically minimizing a cost function.
- (4) error estimate for retrieved parameters

The optimal estimate will be obtained by a nonlinear least squares process with constraints. It will minimize a cost function, which includes contributions from both the departure of the measured spectrum from the calculated spectrum and the departure of the retrieved state from constraints imposed through the *a priori* state. (The *a priori* is not in general the same as the first guess, which is a state selected as a starting point for a non-linear iteration). An appropriate subset of the measured spectrum will be used for each parameter retrieved. This may comprise a microwindow or a large segment of spectrum.

Finally, the complete spectrum will be calculated for quality control. At this point, the atmosphere will be determined as well as possible, but the individual retrievals will not have covered the complete spectrum, so there will be gaps in the surface emissivity (nadir case) or aerosol optical depth (limb case). This necessitates a final retrieval using the entire spectrum, with fixed atmospheric parameters. The results will be the desired spectra, along with spectra of the surface emissivity or aerosol optical depth as by-products.

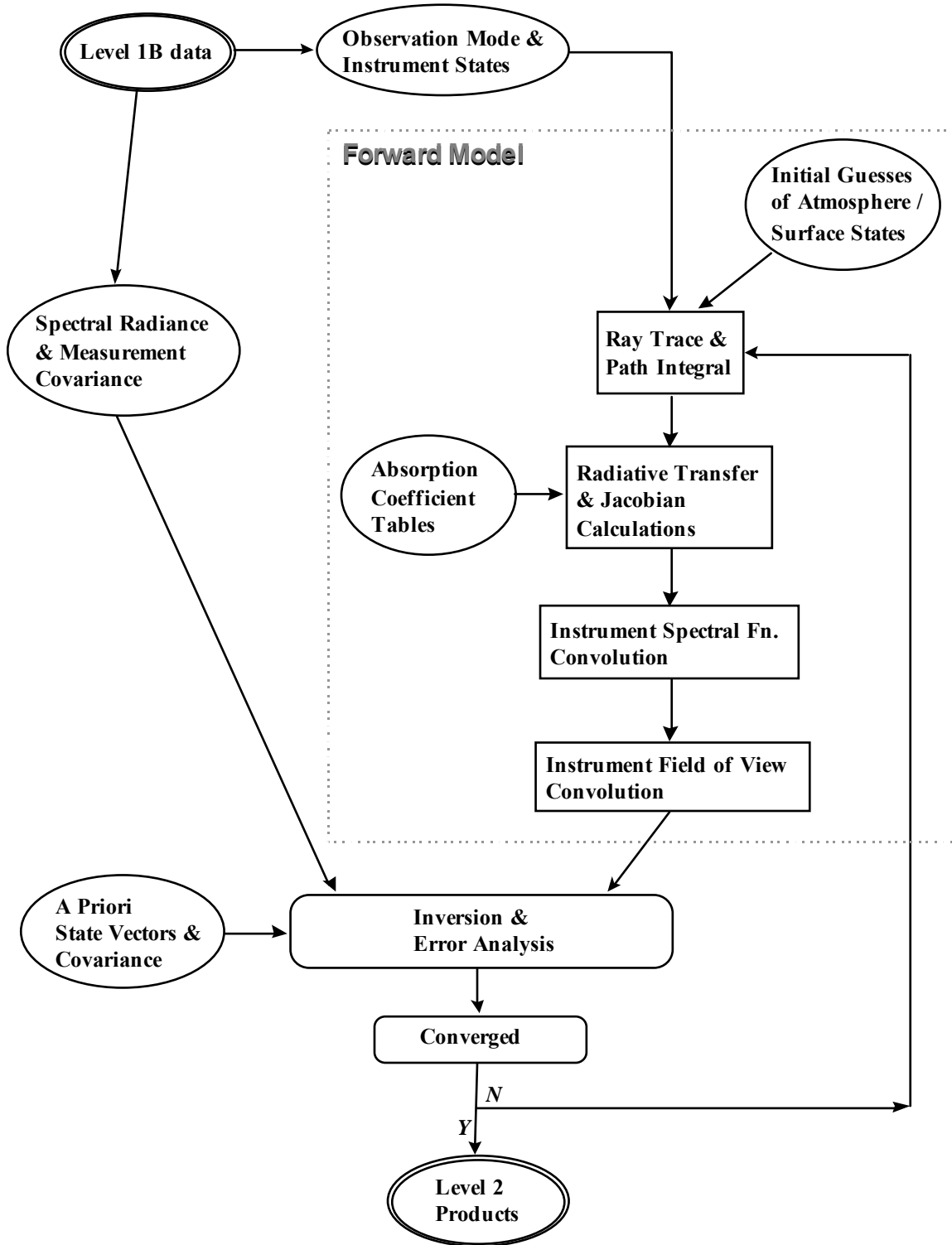
The optimal estimation process requires a numerical model to generate the spectrum expected for a particular atmospheric condition. Below, we describe the parameters necessary to carry out the calculation (3.2), the forward model (3.3), and the derivatives of the spectrum with respect to the desired parameters (3.4). The actual retrieval process is detailed in 3.5.

### **3.1.1 TES Retrieval Algorithm: Earth Limb and Nadir Operational Retrieval (ELANOR)**

Most of the algorithm elements discussed in this document have been coded and tested at the TES SCF in the TWPR (TES Working Prototype Retrieval Algorithm) and now ELANOR, which is the operational retrieval code designed based on TWPR. Prototyping efforts continue to test the speed and accuracy of ideas as they are put forward by the members of the Science Team. The retrieval algorithm is validated using simulated data as discussed in chapter 4.0, and whenever possible, using real data from AES (Airborne Emission Spectrometer), HIS (High Resolution Interferometer Sounder) and IMG (Interferometric Monitor of Greenhouse Gases). These instruments all have spectral resolution and coverage similar to TES, albeit nadir viewing only. When MIPAS (Michelson Interferometer for Passive Atmospheric Sounding) limb data become available, they will be used for the same purpose. It is our intention to continue improving ELANOR, with releases that meet pre-launch testing needs, at launch requirements and post-launch adjustments or added capabilities.

Figure 3-1: TES Level 2 Retrieval Flow

**TES LEVEL 2 RETRIEVAL FLOW**



## 3.2 STATE VECTORS

### 3.2.1 Terminology

A *state vector* specifies those aspects of the state of the atmosphere being measured, and of the instrument measuring it, which together determine the value of the resulting measurement. We will use the term *full state vector* to indicate the complete set of parameters required by the forward model (section 3.3) to simulate a measurement to the necessary accuracy, and the term *retrieval state vector* or simply *retrieval vector* to indicate the subset of the full state vector that is a target for retrieval. The remaining elements will either be predetermined (*forward model parameters*) or be determined by interpolation where the forward model requires a finer grid for numerical purposes.

### 3.2.2 Full State Vector Elements

The following elements comprise the full state vector for calculating nadir radiance:

- surface pressure
- temperature on a specified pressure grid
- constituent mixing ratios on a specified pressure grid
- aerosol extinction coefficients on specified pressure and wavenumber grids
- surface radiating temperature
- surface optical properties corresponding to each detector element on a specified wavenumber grid:
  - emissivity
  - albedo/reflectivity
  - bi-directional reflectivity distribution function
- nadir view angle
- nadir view location
- sun angle at the nadir location
- instrument line shape
- field of view function

The following elements comprise the full state vector for calculating limb radiance:

- temperature on a specified pressure grid
- constituent mixing ratios on a specified pressure grid
- aerosol extinction coefficients on specified pressure and wavenumber grids
- spacecraft position
- look angle of the boresight from the spacecraft
- sun angle at the tangent point location
- altitude of one pressure level
- instrument line shape
- field of view function

In this we assume that the atmosphere is hydrostatically balanced and radially symmetric. For the limb view, it may be necessary to include some representation of horizontal gradients of some of the elements.

There are several other quantities that should formally be part of the full state vector, but are best considered as constants, and treated separately by the forward model. These include

- Constituent absorption coefficients on a wavenumber, pressure and temperature grid.
- Digital elevation model
- Surface characterization map (Global land cover database)

### 3.2.3 Pressure Level Grids

The natural vertical grid for nadir forward model is based on pressure levels, as this is one in which the Jacobians have a particularly simple form. In order to combine results from the nadir and limb views, both must be on compatible grids, so this choice requires us to use a pressure grid for the limb view as well. We have chosen to use  $\log(P)$  as the basic vertical coordinate, and to make the grid spacing compatible with that established for UARS.

The full state vector will be defined on the *full grid*, which is a superset of the retrieval grid:

$$\log_{10}(P_i) = 5 - i/6m \quad (3.1)$$

where  $P_i$  is the pressure in pascals of level index  $i$  and the 'superset factor'  $m$  is an integer. The UARS grid corresponds to  $m=1$ , with a spacing of 6 levels per decade of pressure. The value of  $m$  will be determined by the accuracy requirements of the numerical method, and may vary with height.

The pressure grids for the retrieved state vectors will be subsets of those for the full state. The elements of the retrieval state vector that comprise profiles will be defined on a *retrieval grid*,

$$\log_{10}(P_i) = 5 - i/6n \quad (3.2)$$

The value of  $n$  will be a submultiple of  $m$ , chosen so that the full information content of the measurements can be represented. The range of levels used will vary with the quantity retrieved. The choice of the retrieval pressure levels for each TES product molecule and temperature are key investigation activities which involve the physical constraints used for profile retrieval and the trade-offs between the retrieval vertical resolution and the product accuracy.

Values of the profiled quantities between retrieval grid levels will be determined by the following interpolations:

- (1) Temperature is linearly interpolated in  $\log(P)$ .
- (2) Logarithms of constituent mixing ratios and aerosol extinction coefficients are interpolated and extrapolated linearly in  $\log(P)$ , and linearly extrapolated above the top level at the same gradient as in the top layer.

As an example, for the full state vector of the prototype forward we have constructed an 86-layer atmosphere model for simulations and for the absorption coefficient table pressure and temperature grids. This 86-layer atmosphere has 87 pressure levels between about 1211.53 hPa and 0.1 hPa. The pressure levels (in hPa) are defined up to 1 hPa as

$$P_k = 1000 \times 10^{-(k-2)/24} \quad k = 0 \dots 74; \quad (3.3)$$

and above 1 hPa as

$$P_k = 1000 \times 10^{-(k-38)/12} \quad k = 75 \dots 86; \quad (3.4)$$

In the troposphere, the layer thickness calculated using hydrostatic equation and for US standard atmosphere is about 0.83 km (surface) to 0.6 km (tropopause). Between 100 hPa and 1 hPa, the layer thickness is about 0.6-0.8 km; while above 1 mb, it is about 1.5 km.

### 3.2.4 Spectral Grids

The spectral grid for the monochromatic radiative transfer calculations over the spectral domain associated with a specific filter is determined by the mean Doppler width at the top of the atmosphere. Studies of the dependence of errors in radiative transfer on spectral sampling indicate that for pressure broadened lines, a sampling grid of four points per Lorentz halfwidth is required, [Clough and Kneizys, 1979]. Extension of this analysis to the Doppler and Voigt line shapes leads to essentially the same conclusion. The spectral sampling based on this criterion, in addition to being appropriate for the stratosphere, provides proper spectral sampling of the narrow water lines in the atmospheric window regions and of the line coupling effects of the carbon dioxide Q branches in the pressure broadening regime. Because the spectral grid is based on the Doppler width, the grid, though fixed for a given filter, is frequency dependent by filter (coarser at higher wavenumber values).

Based on studies of computational efficiency and accuracy, a decision has been made to utilize a fixed spectral grid over the domain of a given filter. Use of a fixed spectral grid also facilitates the computation of the forward model radiances and Jacobians by allowing the computation to be easily sub-divided into small spectral “chunks” that can fit in the memory of off-the-shelf computers. Two sets of absorption coefficient files have been computed, (1) a “fine” spectral grid that can sample lines at the top of the atmosphere in our 87-level forward model atmosphere at four points per half-width and (2) an operational grid that, for now, is at half the resolution of the fine grid. The operational grid absorption coefficient tables are computed by convolving a 3-point triangular filter with the fine-grid tables. We find that the radiances computed using this operational grid are accurate to within 0.001% as compared to the radiances computed using the fine spectral grid. Table 3-1 describes the operational spectral grid for each filter.

**Table 3-1: Operational spectral grid for TES filters**

Filter ID	Lower 50% Point, $\text{cm}^{-1}$	Upper 50% Point, $\text{cm}^{-1}$	Operational Spectral Grid ( $\text{cm}^{-1}$ )	Reference Grid ( $\text{cm}^{-1}$ )
1A1	1900	2250	0.0008	0.0004
1A2	2200	2450	0.0008	0.0004
1A3	2425	2650	0.0008	0.0004
1A4	2600	2850	0.0008	0.0004
1A5	2800	3050	0.0008	0.0004
1B1	820	1050	0.0004	0.0002
1B2	950	1150	0.0004	0.0002
2A1	1100	1325	0.0004	0.0002
2A2	1300	1550	0.0004	0.0002
2A3	1500	1750	0.0004	0.0002
2A4	1700	1950	0.0004	0.0002
2B1	650	900	0.0002	0.0001

State vector elements specified on other spectral grids are interpolated by a four-point Lagrangian to the operation spectral grid. Nominal values of other spectral grid spacings are:

- Heavy molecules (e.g., CFC's)  $0.0025 \text{ cm}^{-1}$
- $\text{H}_2\text{O}$ ,  $\text{N}_2$ , and  $\text{O}_2$  continua  $0.1 \text{ cm}^{-1}$
- Clouds and aerosols  $1 \text{ cm}^{-1}$
- Surface emissivity  $10 \text{ cm}^{-1}$
- Surface albedo/reflectivity  $10 \text{ cm}^{-1}$
- Surface bi-directional reflectivity distribution function  $10 \text{ cm}^{-1}$

### 3.3 FORWARD MODEL: ATMOSPHERE

#### 3.3.1 Radiative Transfer

The spectral radiance received by TES can be expressed by the radiative transfer equation. Under clear conditions, the radiance received in a downlooking mode includes four contributions: upwelling atmospheric emission, attenuated reflected downwelling atmospheric emission, attenuated surface emission and attenuated reflected solar radiation. In order to show the influence of the sensor on the signal, the radiance must be convolved with the absolute instrument line shape (ILS). For a single ray, we obtain Equation (3.5):

$$\begin{aligned}
 L(\Omega, \nu) = & \int_0^\infty \Phi(\nu, \nu') \left\{ \int_{z_0}^\infty B(\nu', T(z)) \frac{\partial T(\Omega, z, z_0, \nu')}{\partial z} dz \right. \\
 & \text{(Instrument)} \quad \text{(Upwelling atmospheric emission term)} \\
 & + \alpha(\nu') \cdot T(\Omega, z_0, \infty, \nu') \int_{2\pi} \mathcal{R}_{BRDF}(\Omega, -\Omega', \nu') \int_{\infty}^{z_0} B(\nu', T(z)) \frac{\partial T(-\Omega', z, z_0, \nu')}{\partial z} dz d\Omega' \\
 & \quad \text{(Downwelling, back - reflected, atmospheric emission term)} \\
 & + \varepsilon(\Omega, \nu') \cdot B(\nu', T_{surf}) \cdot T(\Omega, z_0, \infty, \nu') \\
 & \quad \text{(Surface emission term)} \\
 & \left. + \alpha(\nu') \cdot \mathcal{R}_{BRDF}(\Omega, -\Omega_0, \nu') \cdot E_s(\nu') \cdot \Omega_s \cdot T(-\Omega_0, \infty, z_0, \nu') \cdot T(\Omega, z_0, \infty, \nu') \right\} d\nu' \\
 & \quad \text{(Reflected sunlight term)}
 \end{aligned}$$

(3.5)

where

- $L(\Omega, \nu)$  = radiance at frequency  $\nu$  into upward, directed, solid angle  $\Omega$
- $\Phi(\nu, \nu')$  = ILS, i.e. spectral response at frequency  $\nu$  due to incident radiance at  $\nu'$
- $B(\nu, T)$  = Planck function for temperature  $T$  at frequency  $\nu$
- $T_{surf}$  = surface (skin) temperature
- $T(\Omega, z, z', \nu')$  = atmospheric transmittance at frequency  $\nu'$  in a direction  $\Omega$  between altitudes  $z$  and  $z'$
- $\alpha(\nu')$  = surface albedo at frequency  $\nu'$
- $\mathcal{R}_{BRDF}(\Omega, -\Omega', \nu')$  = surface biconical reflectance function for incident (downward) solid angle  $-\Omega'$  and emergent (upward) solid angle  $\Omega$
- $\varepsilon(\Omega, \nu')$  = surface emittance at frequency  $\nu'$  into solid angle  $\Omega$
- $E_s(\nu')$  = disk-average solar radiance at frequency  $\nu'$
- $\Omega_s$  = solar solid angle at Earth

The same equation holds for limb emission sounding if the last three (surface-related) terms are omitted. While the equation, therefore, seems much simpler, the geometry of the light path (especially in the lower atmosphere) becomes much more complicated because of significant refraction effects.

In the next section, a numerical radiative transfer model that was developed for TES will be described. This *forward model* uses atmospheric temperature and constituent profiles and the surface properties as inputs. The integrations in Equation 3.5 are carried out numerically by dividing the atmosphere into thin layers (by pressure). The layer effective quantities, such as the layer effective temperature and pressure and the layer molecular column amount, are calculated

in the ray tracing and path integrals step.

### 3.3.1.1 Ray Tracing and Path Integrals

The lines of sight through the atmosphere must be traced, allowing for the detailed geometry and possible refraction effects. Full details will be found in appendix 3.3.1.1. The basic principles are described here.

The non-sphericity of the Earth is accommodated by using a coordinate system with origin at the center of curvature, at a nominal tangent point, of a reference geoid. In the plane of the ray (refraction horizontally is ignored) the atmosphere is described in terms of functions of radius  $r$  and angle  $\psi$  of the line from the center to the ray element. Quantities in a radially symmetric atmosphere are assumed to be independent of  $\psi$ .

For integrating the hydrostatic equation, a full latitude/altitude model is used for the variation of the acceleration of gravity. The air density is calculated from an equation of state that includes the effect of water, and is not simplified to the perfect gas law. (Appendix 3.3.1.1.7)

For the quasi-nadir case, the ray tracing is evaluated from simple trigonometry, ignoring refraction. Integrals of absorber amounts and temperature are carried out analytically over full grid layers, assuming that  $\ln(q)$  and  $T$  are linear in  $\ln(P)$ . This is a change.

For the limb case, the approach used is based on that of Kneizys *et al.*(1983). The coordinate  $x = r \cos\theta$  is used along the ray to avoid the singularity at the tangent point. The zenith angle of the ray,  $\theta$ , is obtained from Snell's law for spherical symmetry,  $n(r)\sin\theta(r) = \text{constant}$ , and the distance element  $ds$  along the ray is related by  $dr = \sin\theta ds$ . This can be shown to give

$$ds = dx/[1+(r/n)(\partial n/\partial r)\sin^2\theta(r)] \quad (3.6)$$

which can be used to integrate path integrals with respect to  $x$ , an explicit function of  $r$ , rather than  $s$ . The integrals are evaluated by dividing each full grid layer into sub-layers in  $x$ , such that all quadrature intervals are smaller than a given length, and using a trapezium or higher order quadrature.

When the atmosphere is not radially symmetric, the above ray tracing technique does not apply because we can no longer assume that  $n(r)\sin\theta = \text{constant}$ . In this case we can use a more general approach and construct a set of three coupled ordinary differential equations in  $r(s)$ ,  $\theta(s)$  and  $\psi(s)$  to describe the ray trajectory. These are integrated forwards from an assumed tangent point to the satellite altitude. The horizontal location of the tangent point as expressed by  $\psi(0)$  is then iterated so that the ray reaches the location of the satellite. Path integrals are evaluated in the same way as for the radially symmetric case, but using the same quadrature points in  $s$  as are used by differential equation integration.

### 3.3.1.2 Ray Tracing (Surface Layer)

The pressure boundaries of the forward model atmospheric layer above the Earth's surface must be redefined for every TES observation. This layer will be thinner than or equal to the TES

standard forward model layers near the surface. The sea surface pressure will be obtained from fields obtained from available meteorological data (section 3.5.1.4.2). The earth surface pressure (the lower pressure boundary for the surface layer) will be calculated from the sea surface pressure using the hydrostatic equation at the TES identified elevation (section 3.3.2.3). The top pressure boundary for the surface layer will be a TES fixed pressure level.

### 3.3.1.3 Optical Depth

The optical depth (OD) along the line of sight for a given layer  $l$  is calculated as

$$\tau(\nu)_l = \sum_m u_{m,l} k_m(\bar{T}, \bar{P}, \nu) \quad (3.7)$$

where the sum is over species,  $u_{m,l}$  is the layer molecular amount for absorber  $m$ , and  $k_m(\bar{T}, \bar{P}, \nu)$  is the absorption coefficient for molecule  $m$ .  $u_{m,l}$ ,  $\bar{T}$ , and  $\bar{P}$  are calculated in the ray-trace and path integral step. Although we will still keep the option of using a line-by-line model to calculate absorption coefficients, for most molecules  $k_m(\bar{T}, \bar{P}, \nu)$  will be pre-calculated at fixed P/T grids and stored in files (ABSCO Tables). Section 3.3.7 describes the ABSCO Table generation and discusses the  $k_m(\bar{T}, \bar{P}, \nu)$  interpolations in temperature / pressure / H<sub>2</sub>O VMR. The frequency grid spacing of  $\tau(\nu)$  for the line species in the HITRAN list is defined in Table 3-1.

The cross-section, continuum, and cloud absorption coefficients (section 3.5 and 3.6) will be stored and calculated on a coarser frequency grid spacing (section 3.2.4). This is mostly determined by the representative spectral structures shown in some cross-section species, and this coarser frequency spacing is the TES tier 2 spacing.

The total layer optical depth is then calculated by the sum of the tier 1 OD and the interpolated tier 2 OD. The tier 2 to tier 1 interpolation is performed using a 4-point Lagrange interpolation scheme.

### 3.3.1.4 Atmospheric Radiance

The spectral radiance at the satellite is given in equation (3.5). By neglecting the reflected sunlight term the monochromatic radiance may be summarized as

$$L_{sat} = L_L^\uparrow + \varepsilon B(T_{sc}) \mathcal{T}_{0,L} + \alpha L_0^\downarrow \mathcal{T}_{0,L} \quad (3.8)$$

in which  $L_L^\uparrow$  is the upwelling radiance contribution of the atmosphere from the surface to the level at the top of the atmosphere (TOA),  $\mathcal{T}_{0,L}$  is the transmittance of the atmosphere and  $L_0^\downarrow$  is the downwelling radiance of the surface. For a specularly reflecting surface,  $L_0^\downarrow$  is calculated for the same zenith angle as  $L_L^\uparrow$  and  $\alpha$  is the appropriate bidirectional reflectance. For a Lambertian surface,  $L_0^\downarrow$  is calculated at the diffusivity angle, the downwelling radiation scattered by the surface is taken to be isotropic and  $\alpha$  is the albedo.

In the limb case, there is no surface term.  $L_{\uparrow L}$  is then the radiance contribution from the portion of the atmosphere from the tangent to the satellite and  $L_{\downarrow 0} \mathcal{T}_{0,L}$  would be the radiance contribution from the atmosphere from the far-side space to the tangent along the line of sight.

The upwelling term,  $L_{\uparrow L}$ , the downwelling radiance,  $L_{\downarrow 0}$ , and the total transmittance  $\mathcal{T}_{0,L}$  are calculated recursively in a layer loop. For example, in the case that the calculation starts from Earth's surface to satellite,  $L_{\uparrow L}$ ,  $L_{\downarrow 0}$ , and  $\mathcal{T}_{0,L}$  are initialized as 0.0, 0.0, and 1.0. At each layer step ( $l$ ), they are updated as (illustrated in Figure 3-2)

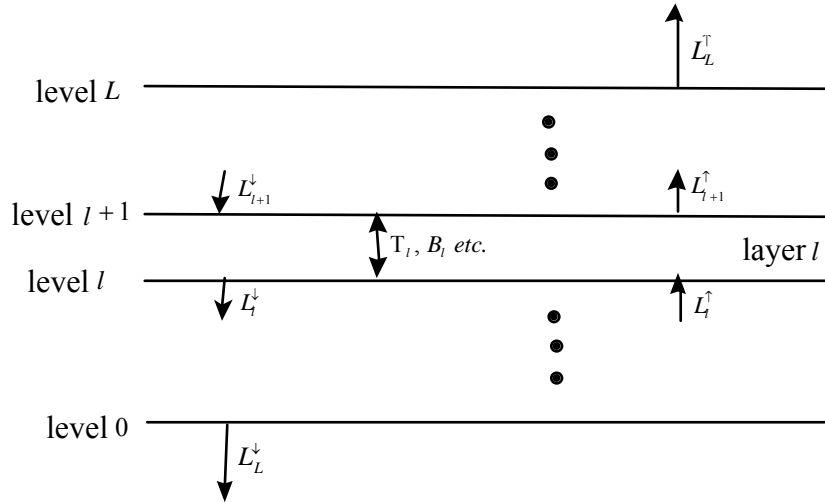
$$L_{\uparrow l+1} = L_{\uparrow l} \mathcal{T}_l + (1 - \mathcal{T}_l) B_{eff} \tag{3.9}$$

$$L_{\downarrow l+1} = L_{\downarrow l} + (1 - \mathcal{T}_l) B_l \mathcal{T}_{0,l} \tag{3.10}$$

$$\mathcal{T}_{0,l+1} = \mathcal{T}_{0,l} \mathcal{T}_l \tag{3.11}$$

where  $\mathcal{T}_l$  is the layer transmittance which is not necessarily the same for upwelling and downwelling cases ;  $B_l$  and  $B_{eff}$  are the Planck function at layer mean temperature  $T_l$  and the layer effective Planck function defined below.

**Figure 3-2: Illustration of the recursive radiative transfer calculations**



The layer transmittance  $\mathcal{T}_l$  is calculated as

$$\mathcal{T}_l = \exp(-\tau_l) \tag{3.12}$$

where  $\tau_l$  is the layer optical depth, as described in 3.3.1.3. Since the exponential calculation is relatively expensive, it is pre-computed and tabulated.

In order to simulate the contribution of the layer emission to the total radiance more accurately, we apply the “linear-in-tau” approximation [Clough et al., 1992]. The source term in equation 3.9 uses an effective Planck function defined as

$$B_{eff}(\bar{T}_l, T_{l+1}, \tau_l) = B(\bar{T}_l) + [B(T_{l+1}) - B(\bar{T}_l)] \left\{ 1 - 2 \left[ \frac{1}{\tau_l} - \frac{\mathcal{T}_l}{1 - \mathcal{T}_l} \right] \right\} \quad (3.13)$$

where  $B(T_{l+1})$  is the Planck function calculated using the layer upper level temperature,  $T_{l+1}$ . The function

$$F(\tau_l) = 1 - 2 \left[ \frac{1}{\tau_l} - \frac{\mathcal{T}_l}{1 - \mathcal{T}_l} \right] \quad (3.14)$$

and its derivative with respect to optical depth are pre-calculated and tabulated for computation efficiency. For small optical depth,  $F(\tau_l) \rightarrow \frac{\tau_l}{6}$  for  $\tau_l \rightarrow 0$ , which can be shown either graphically or by expanding  $F(\tau)$  to 2<sup>nd</sup> order terms. This effective Planck function has the desired behavior at the two extremes, e.g., optically thin layers,  $B_{eff} \approx B(\bar{T}_l)$  and optically thick layers,  $B_{eff} \approx B(T_{l+1})$ .

The calculation of Planck function as a function of frequency at the forward model frequency grids is very time consuming. We therefore implemented a piecewise continuous approximation in this calculation. The accurate Planck function is calculated at coarser frequency grids (section 3.2.4) and a linear interpolation is done for the grids in between.

### 3.3.1.5 Non-LTE

In certain circumstances it is necessary to make allowances for departures of the source function  $J$  from the Planck function. This will be most important for the case of nitric oxide, which has significant non-thermal emission from the thermosphere, particularly in the presence of solar activity. This emission can be a significant fraction of the total measured NO signal. To account for Non-LTE the forward model must be able to accept the populations of the individual vibrational levels affected relative to the Boltzmann population, which depends only on temperature. The algorithm to be implemented in the forward model for the calculation of NLTE radiances is provided in Appendix A3.3.1.5.

Two approaches are being explored to obtain NLTE state populations for the TES spectral measurements:

- (1) Estimate the populations of the excited states, using existing models and climatological temperature and solar irradiance values. This will provide a non-LTE climatology to be included as forward model parameters. For NO, retrieve only the mixing ratio in the troposphere and lower stratosphere.

- (2) Retrieve the populations of the affected vibrational levels at all relevant altitudes, as well as the mixing ratio distribution. This would proceed in the same way as retrieval of any other parameter, by including the relative populations in the state vector, and computing the Jacobians for them.

### 3.3.1.6 Radiative Transfer for the Solar Contribution

The contribution to the radiance at the satellite due to scattered solar radiation must be taken into account in the spectral region 2000-3050  $\text{cm}^{-1}$ . Experience with HIS spectra suggests that, under solar conditions, there is almost always some solar scattering due to atmospheric clouds and aerosols (see section 3.3.3) in addition to the scattering from the surface. Empirical techniques will be developed and utilized to address scattered solar effects in the affected microwindows in addition to the treatment of the scattered radiation from the surface. For the nadir case, the radiative transfer including the surface scattering is given as

$$L_{\text{sat}} = L_L^\uparrow + \varepsilon B(T_{\text{sfc}}) \mathcal{T}_{0,L} + \alpha L_0^\downarrow \mathcal{T}_{0,L} + \mathcal{R}_{\text{BRDF}}(90, \theta_{\text{sun}}) J_{\text{sun}} \mathcal{T}_{\text{sun}_{0,L}} \mathcal{T}_{0,L} \quad (3.15)$$

where  $J_{\text{sun}}$  is the solar source function at the top of the atmosphere,  $\mathcal{T}_{\text{sun}_{0,L}}$  is the transmittance of the atmosphere along the solar refracted path and  $\mathcal{R}_{\text{BRDF}}(90, \theta_{\text{sun}})$  is the surface bidirectional reflectance.

The solar contributions will be calculated at the monochromatic wavenumber grid. The appropriate Doppler shift due to Earth's rotation and orbit, and radiance adjustment due to the distance of the Earth to the sun will be taken into account. Treatment of these effects involves minimal computation time.

The method of calculation will be to use an effective secant for the solar path in each layer, thus making use of the optical depth calculation being done for the upwelling atmospheric radiation. The reference radiative transfer model will have the capability to treat solar scattering in the single scattering approximation at each layer given a profile of scatterers and their optical properties. The initial approach for the limb will be to remove spectra that are strongly contaminated by solar scattering in the 2000-3050  $\text{cm}^{-1}$  spectral domain, recognizing that if strong aerosol conditions exist, appropriate methods will be applied to extract as much information as possible for species optically active in this region [Rinsland *et al.*, 1994].

### 3.3.1.7 Surface Contribution

The radiance at the satellite including the effects of scattering and reflection at the surface may be written as,

$$L_{\text{sat}} = L_L^\uparrow + \varepsilon B(T_{\text{sfc}}) \mathcal{T}_{0,L} + \alpha L_0^\downarrow \mathcal{T}_{0,L} + \mathcal{R}_{\text{BRDF}}(90, \theta_{\text{sun}}) J_{\text{sun}} \mathcal{T}_{\text{sun}_{0,L}} \mathcal{T}_{0,L} \quad (3.16)$$

where  $J_{\text{sun}}$  is the solar source function at the top of the atmosphere,  $\mathcal{T}_{\text{sun}_{0,L}}$  is the transmittance of the atmosphere along the solar refracted path and  $\mathcal{R}_{\text{BRDF}}(90, \theta_{\text{sun}})$  is the surface bidirectional

reflectance. The terms associated with the upwelling radiance of the atmosphere, the surface emitted radiance and the surface reflected solar radiance can be treated rigorously assuming that the surface emittance is isotropic with emissivity  $\varepsilon$  and that  $\mathcal{R}_{\text{BRDF}}(90, \theta_{\text{sun}})$  properly describes the solar scattering by the surface. The radiance due to the surface scattering of the downwelling irradiance is a rather more complex problem. First, this term is assured not to be large: if the atmosphere is in the optically thin regime then the downwelling flux is small, and is further reduced by the surface albedo so that the radiance at the satellite is dominated by the surface emitted radiance attenuated by the satellite. In the optically thick regime, there is no contribution from other than upwelling radiance of the atmosphere. As a consequence of this perspective, the accuracy of the forward model radiance at the satellite is not highly dependent on the accuracy of the value for the albedo or on the accuracy of the calculation of the downwelling irradiance.

The scattering due to the surface is characterized as either Lambertian or specular. For the Lambertian case, the downwelling irradiance,  $L_{\downarrow}^{\circ}$  is required. This is obtained by performing the radiance calculation along the diffusivity ray (secant = 1.66) [Chandrasekhar, 1960, Goody and Yung, 1989]. The product of this radiance and the albedo provides an excellent approximation to the scattered upwelling isotropic radiance at the surface. The motivation for this approach is the low computational cost with acceptable accuracy. The layer optical depth for the diffusivity angle is obtained by multiplying the nadir layer optical depth by the secant angle. Although an additional exponential is required, this approach is faster than alternative methods. In general, the albedo will be taken as  $1-\varepsilon$  with  $\varepsilon$  a retrieved parameter but could also be retrieved directly.

In the case of specular reflection,  $\alpha$  assumes the role of a bidirectional reflectance, e.g.  $\mathcal{R}_{\text{BRDF}}(90, 90)$  for the nadir case. The downwelling radiance is calculated for the same secant as the upwelling (secant = 1 in the nadir case) and the same layer transmittances are used for both the upwelling and downwelling radiances. This calculation is fast and has full accuracy.

### 3.3.1.8 Simultaneous Multiple Rays

Two computationally expensive stages in the calculation of the radiance at the satellite for a given ray in the limb mode are the calculation of the spectral absorption coefficients and the calculation of the spectral radiative transfer. With the exception of the tangent layer the absorption coefficients required to calculate optical depths are the same in a given layer for all rays passing through that layer under the assumption that the layers are spherically symmetric. Consequently, given the optical depths for a given ray through a layer, the optical depths for all other rays through the layer may be obtained by multiplying this optical depth by the appropriate ratio of the integrated path amounts of dry air for the other rays. For the tangent layer (and perhaps the adjacent layer) the pressure and temperature are different from that of the pre-stored pressure grid and the absorption coefficients must be obtained specifically for the ray through tangent layer. Using an approach that retains the information required for the calculation of the required optical depths for all rays in this fashion, essentially eliminates the cost of multiple lookups of absorption coefficients and with the subsequent calculations of the optical depth. The additional quantities to be stored in the general case is small, namely the number of tangent rays. We refer to this approach for the limb as a simultaneous multiple ray approach, since the

information for all rays to the satellite is obtained with a single detailed calculation of optical depth in each layer plus one extra for each tangent layer.

Certain savings of this type can also be achieved in the radiative transfer, principally the calculation of the Planck functions. However, the computational cost of the Planck functions in our current implementation is sufficiently small that the gain in treating the multiple tangent rays simultaneously may not be warranted.

### 3.3.1.9 Horizontal Inhomogeneity

At the limb, the path length through the tangent layer can be many tens of kilometers. Consequently, the assumption that the atmosphere is homogeneous in composition and physical state may not be valid. It further follows that the ensuing discussion is tentative and subject to “lessons learned” once we are on orbit.

The approaches that we shall investigate (in order) are

- 1) Ignore Line-of-Sight (LOS) gradients in the forward model, retrieve a single profile from a single set of spectra, and include the effect in the error analysis (*i.e.* if a gradient exists, the residuals will increase).
- 2) Assume some known LOS gradients in the forward model. For temperature/pressure this can come from meteorological data. For constituents it can come from a first pass using method (1). This approach has been used by LRIR, LIMS, and ISAMS.
- 3) First perform a “nadir-type” retrieval (but with cold space rather than the Earth’s surface as background) *along the LOS*. The weighting and contribution functions will be strongly peaked in the tangent layer, but this is where inhomogeneity will have most of its impact. Use the results (one for each pixel) as a first guess for the standard limb retrieval.
- 4) Retrieve the 2-D distribution (or at least a mean profile and a profile of the LOS gradient) from a single set of spectra. If horizontal inhomogeneity has a measurable effect on the radiances, then there is, in principle, information about it from which it might be retrieved. However this information might also alias into something else. Only numerical experiments can tell the difference.
- 5) Simplified tomography by sequential estimation. For example, consider successive profiles at the locations corresponding to three successive measurements. Call them A, B, and C in time order. Set up an *a priori* (see later). Use the B spectra to retrieve all three profiles jointly. The result gives the final retrieval for the A profile. The retrievals so far for B and C become *a priori* for the next cycle, and *a priori* for D, the next location, are obtained by a combination of, for example, climatology and extrapolation. Now use the C spectra to retrieve B, C, and D jointly. This gives the final retrieval for B and the C and D *a priori* for the next cycle. Repeat.

### 3.3.2 Surface Model

#### 3.3.2.1 Surface Radiative Properties

TES nadir data will have many spectral regions that contain information about the surface radiative properties, (“window” regions). As discussed in 3.3.1, unless we have additional information about the bi-directional reflectance, the surface model must choose either a Lambertian or specular reflectance approximation for the forward model calculation. For either case, we will assume that the albedo is  $1-\varepsilon$ , where  $\varepsilon$  is the emissivity. For any forward model frequency,  $\nu$ , the emissivity is calculated from a linear interpolation. We can then model the surface contribution with a single “skin” temperature and the emissivity spectrum, which gives us the flexibility to adjust the emissivity structure for specific target types.

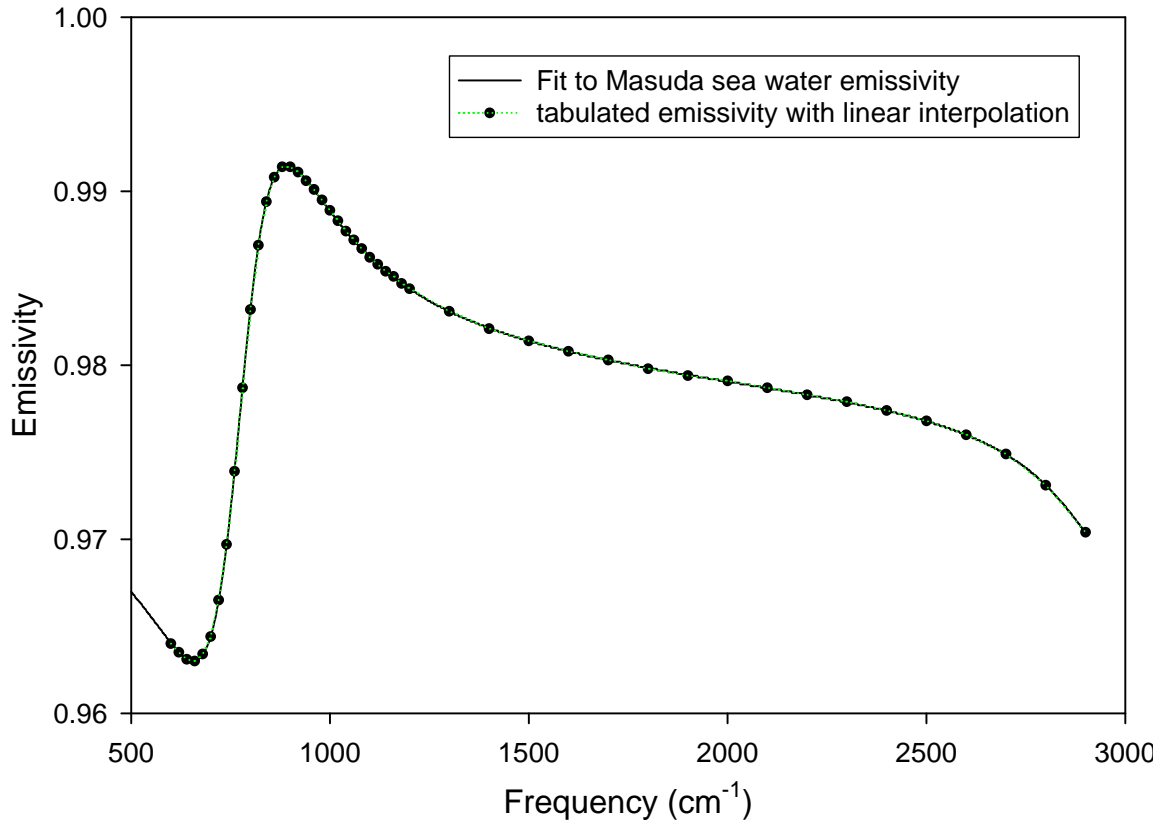
The *a priori* emissivity values will be obtained from a database structured by month and lat/lon coordinates. To populate the database, we may use a combination of ASTER emissivity products, where available, and emissivities derived from knowledge of the seasonal land cover characteristics. Although ASTER will have a very coarse spectral resolution, (5 channels between 8 and 12  $\mu\text{m}$ ), it measures the reflective properties of actual nadir targets from space. For land nadir target scenes where we do not have measured emissivities, we will generate the emissivity first guess using the seasonal land characteristics for the target spot and weighted emissivity spectra for the specific materials (e.g., deciduous trees or dry grass) that are likely to be present. Note that the preponderance of our nadir targets are either water or ice, which have reasonably well known emissivities [Smith *et al.*, 1996 and Masuda *et al.*, 1988] (See Figure 3-3).

#### 3.3.2.2 Map of Earth Surface Composition

In order to arrive at a reasonable first guess of emissivity, or where appropriate, the bi-directional reflectance for a target surface scene, we will need an up-to-date estimate of the seasonal land cover for the latitude and longitude of each pixel in a given nadir view. Since the footprint of an individual pixel is approximately 0.5 by 5 km, a database with spatial resolution of order 1 km (or 32 arc-seconds) should suffice. An existing database of land cover characteristics with 1 km resolution is described in Appendix 3.3.2.3. This database can be used for our initial algorithm development and testing, however, it is also important to note that improved databases, tailored more to the needs of infrared spectral remote sensing, should be available by TES launch.

For the TES Level 2 algorithm to access this type of data efficiently, the global maps will likely need to be reformatted from separate seasonal images to a look-up table of land cover type vs. season or month, latitude and longitude. The land cover type from the table would then specify the emissivity function to be used in the first guess of the surface model parameters. If a particular land cover type required further differentiation, such as snow/ice or dry/wet grasslands, additional information, if available, could be employed. If no additional information were available, default values for the emissivity of the ambiguous land cover type would be used.

**Figure 3-3: Fit to sea water emissivity [Masuda *et al*, 1988] using a double dispersion curve (private communication, Clough, S.A., AER) shown with the tabulated emissivities that are interpolated for computing ocean surface radiances in the TES forward model.**



### 3.3.2.3 Digital Elevation Model

The digital elevation map (DEM), together with NCEP sea level pressures and the hydrostatic equation, are used to estimate the surface pressure at the location of an observation for nadir retrievals. The DEM simply provides the difference in altitude between the location of an observation and sea-level pressure reference geoid. Integration of the hydrostatic equation, using this elevation difference and the *a priori* temperature profile, gives an estimate of the surface pressure.

There are a number of global DEMs available. The only issue is horizontal resolution and vertical accuracy. The highest spatial resolution DEMs with global coverage are limited to latitude-longitude bins of 5 arc-minutes. At the equator this corresponds to an area of 9.28 x 9.28 km<sup>2</sup>, somewhat larger than the 8.5 km along track by 5.5 km cross-track nadir footprint of (i.e. the coverage of a 16-pixel TES detector array). The altitude at the pixel is estimated from a 2 dimensional linear fit and interpolation of the DEM elevations along the spacecraft track.

The requirements for DEM altitude accuracy is driven by the requirement that errors in total column density be less than 0.5%. This translates into a maximum allowable elevation error of about 42 m near sea level.

The principle candidate data set is the GTOPO30:

<http://www.ngdc.noaa.gov/seg/globsys/globe.html>

under development at NOAA's National Geophysical Data Center. It improves upon the ETOPO5 map with increased horizontal resolution (30-arc-second or 1 km grid). Currently, this map covers about 60% of the Earth's land surface. It is anticipated that this data set will cover the Earth's complete land surface before launch of the CHEM platform.

The EOS Product Generation Software Tool-Kit provides routines to extract the elevation data from both of this DEM.

### 3.3.3 Radiative Transfer for Clouds and Aerosols

The capability to treat cloud aerosol radiative effects is an important aspect of the radiative transfer to be included in the forward model. Clouds and aerosols differ from gases not only because their light extinction behavior varies slowly with frequency, but also because they are scattering and absorbing, not simply absorbing like gases. The principal contributions to the radiative transfer associated with aerosols are somewhat different for the nadir and limb viewing modes. The general radiative transfer equation including scattering and ignoring solar radiation terms and downwelling reflected atmospheric emission is as follows.

$$\begin{aligned}
 L(\Omega, \nu) = & \int_0^\infty \Phi(\nu, \nu') \left\{ (1-\omega_\nu) \int_{z_0}^\infty B(\nu', T(z)) \frac{\partial T(\Omega, z, z_0, \nu')}{\partial z} dz \right. \\
 & \left. + \varepsilon(\Omega, \nu') \cdot B(\nu', T_{surf}) \cdot T(\Omega, z_0, \infty, \nu') \right\} d\nu' \\
 & + \frac{\omega_\nu}{2} \int_{z_0}^\infty \int_{-1}^1 P(\mu, \mu') L(\Omega, \nu, z) \frac{\partial T(\Omega, z, z_0, \nu')}{\partial z} d\mu dz
 \end{aligned} \tag{3.17}$$

This equation differs from equation (3.5) in the following ways:

- The transmittance now includes transmittance due to aerosols and clouds.
- The atmospheric emission term is now multiplied by  $(1-\omega_\nu)$ , where  $\omega$  is the single scattering albedo, defined as  $\omega_\nu = \sigma(\nu) / (\sigma(\nu) + \kappa_\nu)$  where  $\sigma(\nu)$  is the scattering cross section and  $\kappa_\nu$  is the absorption cross section. It should be noted that the single scattering albedo will be a function of frequency, as it is a measure of the scattering coefficient compared to the total extinction. When the gas optical depth is large, the single scattering albedo will be small.
- There is an additional term (the third term) that is the source function for scattering – this represents radiation that is scattered into the line of sight. Under single scattering conditions (small single scatter albedo), this term is insignificant.

The importance of this term will also be dependent on the viewing geometry due to the angular dependence of the phase function.

### 3.3.3.1 Radiative Transfer for Aerosol in Nadir View

The general radiative transfer equation presented above will not be solved generally for operational analysis. Instead, a subset of tractable cases will be considered.

If no clouds or aerosols are present, the single scattering albedo is zero, and this equation becomes (3.5), the radiative transfer equation presented in section 3.3.1.

When the optical thickness of the cloud or aerosols is small, the single scattering albedo is small and single scattering dominates. The scattering source function can be ignored and the extinction effects of the cloud can be approximated by absorption. This is accomplished by assuming that the single scattering albedo is zero and using ‘pseudo extinction coefficients’ – absorption coefficients for the cloud or aerosol that result in the same radiative transfer effects as scattering and absorption. For an example of this approach, see Echle *et al.* (1998)

When microwindows are used for the radiative transfer, an assumption of linearity can be made for the cloud or aerosol pseudo-extinction spectra dependence. To implement such a strategy, two cross section species will be created, one with a positive slope, the other with a negative slope. Profile of these two species will be retrieved. The ratio of the two species can vary and allow for any slope. The overall magnitude of the two retrieved profiles is an indication of the overall optical depth of the cloud or aerosol layer. There is a risk that the sensitivity of these cross section species to the cloud height is not large, and the cloud retrieval will interfere with the retrieval of other species that have linear spectral dependence across microwindows, such as the water vapor continuum. This will be investigated.

There may be cases where the optical thickness of the cloud is quite large. In this extreme,  $T$  of the cloud is so small (the optical depth is so large) that the surface term and the atmospheric emission terms below the cloud layer do not contribute to the TOA radiance. Given the fact that clouds have a fairly well defined upper surface, it is natural to redefine the surface as the upper boundary of the cloud. In cases where the cloud optical depth is large (greater than 7, or 8) the transmittance through the cloud is quite small ( $9 \times 10^{-4}$  or  $3 \times 10^{-4}$ ) and rather uniform across the spectra. With the surface redefined as the cloud top height, the first and second terms of the above RT equation remain, and it becomes the original RT equation discussed in section 3.3.1.

Intermediate cases where the scatter source function term is important will not be considered in routine processing.

### 3.3.3.2 Radiative Transfer with Scatterers in the Limb

In the case of limb viewing geometry, the surface emission term is not present.

In the case of optically thick aerosols and clouds, where backside radiation is removed with more than 99.99% efficiency, one may consider the cloud or aerosol as the surface. Unfortunately, there is great uncertainty as to the actual location of the cloud – with the placement along the

line of sight poorly known, it would be quite difficult to define the radiative transfer problem in a tractable way. Therefore, in the case of optically thick aerosols or clouds, the surface will be redefined to the lowest pixel not effected by the aerosol or cloud ( see 3.5.5 pixel categorization section for more details).

In some cases, it may be possible to include a parameterized form of the term for the scattered source. This will be discussed in more detail in ATBD v1.3.

For limb measurements, it will be important to account for the effects of stratospheric sulfuric acid aerosols. Under background conditions (sufficient long time after a volcanic eruption), this will be a low optical depth layer at altitudes roughly from 17 to 24 km. No surface term is needed and the scattering source term can be ignored. As was done in the nadir, ‘pseudo extinction’ coefficients can be used to treat the aerosol effects as absorption with linear dependence across the microwindows. (Echle *et al.* (1998)). This will be achieved with the two linear cross section species described in section 3.3.3.1.

### **3.3.4 Solar Source Function**

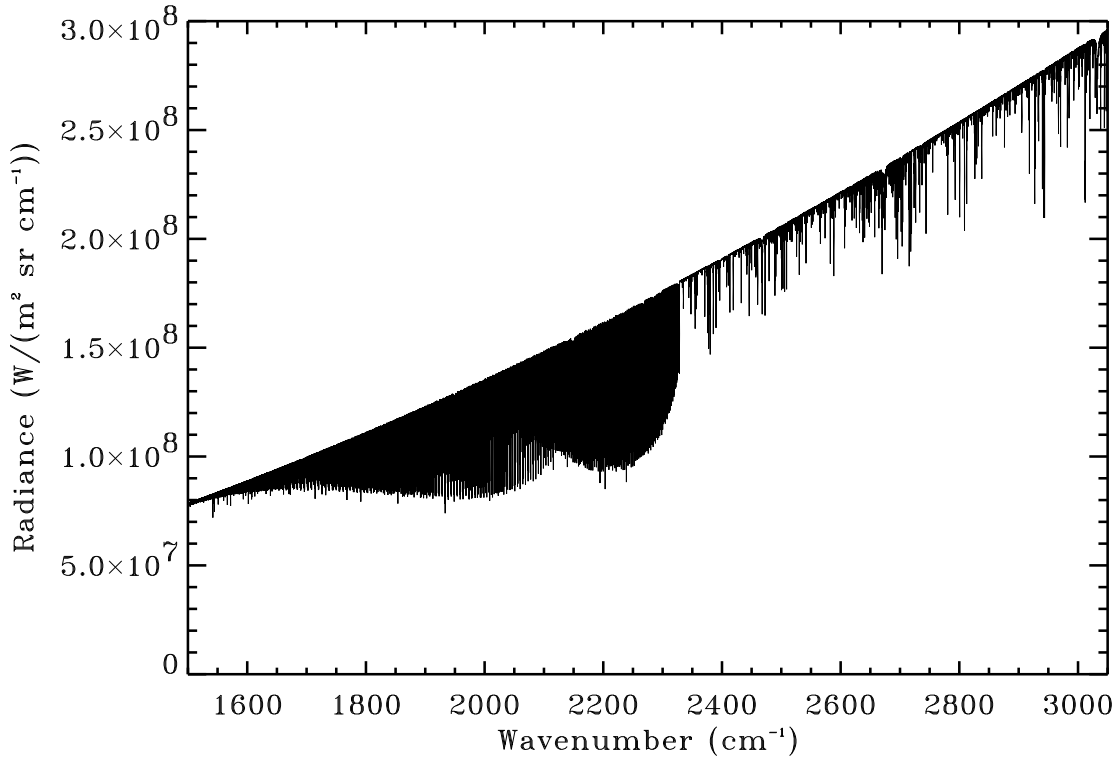
Extraterrestrial solar radiance will contribute to the TES observed radiance in the 2000-3050  $\text{cm}^{-1}$  spectral regime. In order to accurately model the impact of the solar source radiance in the spectrum, the solar source function of Kurucz [1995, 1992, 1984], shown in Figure 3-4, is used in the forward model. It is the result of a radiative transfer calculation based upon solar measurements, including those of ATMOS [Gunson *et al.*, 1996], with a resolution of 0.0040  $\text{cm}^{-1}$  at 2000  $\text{cm}^{-1}$  and 0.0061 at 3050  $\text{cm}^{-1}$ . The spectra are interpolated and stored on the operational monochromatic frequency grid.

Given the solar function  $J_{\text{SUN}}$ , total transmittance through the atmospheric path  $\mathcal{T}_{0,L}$ , and surface albedo  $\alpha$ , the solar contribution to the radiance observed at the satellite  $L_{\text{SUN}}$  is given as

$$L_{\text{sun}} = J_{\text{sun}} \mathcal{T}_{0,L} \alpha \quad (3.18)$$

where  $\alpha=1$  in limb viewing mode. This source function results from a spatial integration over the solar disk and is provided at monochromatic resolution. For radiative transfer calculations using the solar source function, the proper Doppler shifts between the scattering medium (nadir view) and the sun must be applied to the spectrum. Initially we would assume a static solar source function, but we may need to investigate the effects of the solar cycle.

Figure 3-4: Monochromatic solar spectrum over the spectral region relevant to TES (Kurucz, 1995).



### 3.3.5 Instrumental Line Shape Spectral Convolution and Apodization

In order to compare with the measured spectra, the calculated monochromatic spectra at very fine spectral grids described in previous sections need to be convolved, or smoothed, with the instrument line shape (ILS) function. This convolution is described as

$$L_C(\nu) = \int_{-\infty}^{\infty} L_M(\nu') \Phi(\nu - \nu') d\nu', \quad (3.19)$$

where  $L_M$  and  $L_C$  are the monochromatic and convolved spectral radiances respectively, and  $\Phi$  is the ILS function which ideally is a *sinc* function.

An efficient way of performing the above convolution is to multiply the Fourier transforms of the  $L_M$  and  $\Phi$  and then transform the result back to the frequency domain. This method directly simulates the operation of a FTS. The monochromatic radiance is transformed into an interferogram, then it is apodized, and transformed back to obtain the convolved spectra.

The spectral range for  $L_M$  (the integration boundaries in equation (3.19)) calculated in the forward model needs to be extended beyond the range of  $L_C$  in use. Study shows that this

extension should be over 160 *sinc* halfwidths so that the error in  $L_C$  due to this truncation becomes insignificant (Gallery and Clough, 1992). In cases where microwindows are used for retrievals, this extension of the monochromatic spectra could make the forward model calculations more computationally expensive. For example, a  $\pm 6 \text{ cm}^{-1}$  extension is needed for TES nadir simulations. Norton-Beer apodization would reduce this frequency extension. For the general case, 160 halfwidths corresponds to a *sinc* function amplitude decrease of 0.0035. Therefore, we have estimated the extension needed for the Norton-Beer apodization functions based on the fractional amount in frequency space where these decrease to 0.0035 of their maximum values compared to the *sinc* function defined on the same frequency index scale. Table 3-2 lists the spectral resolutions and the minimum extensions for  $L_M$  to derive  $L_C$  based on four different apodizations.

**Table 3-2:** Resolution and suggested forward model extension values.

Apodization Case	Resolution Factor	Nadir Resolution ( $\text{cm}^{-1}$ )	Nadir Extension ( $\text{cm}^{-1}$ )	Limb Resolution ( $\text{cm}^{-1}$ )	Limb Extension ( $\text{cm}^{-1}$ )
None (box function)	1.0	0.07143	6.0	0.01786	1.5
Norton-Beer Weak	1.2	0.08571	3.36	0.02143	0.84
Norton-Beer Medium	1.4	0.10000	1.44	0.02500	0.36
Norton-Beer Strong	1.6	0.11429	0.48	0.02857	0.12

The measurement of radiance by off-axis detectors introduces self-apodization, frequency scaling, line broadening, and asymmetry to the ILS (Bowman *et al.*, 2000). The Level 1B process will correct most of the off-axis effects, but does not remove the residual asymmetry in the ILS (see TES Level 1B ATBD). As a result, this asymmetry must be modeled in Level 2. Derived from the instrument calibration, a residual ILS correction function in the interferogram domain will be provided for a given filter and pixel, in nadir and limb mode respectively.

If no other type of apodization is applied, the residual ILS correction function together with the maximum optical path difference (max OPD) for nadir and limb mode respectively are used for apodizing the “interferogram” of the monochromatic radiance. This correction of the residual ILS function can be ignored however, if Norton-Beer apodizations on both measured and modeled spectra are applied.

### 3.3.6 Field-of-View Spatial Integration

The TES forward model derives the effective radiative response of a pixel at the satellite by performing a trapezoidal integration of the Field Of View (FOV) function with the representation of the radiance field provided by multiple rays originating at specified tangent points. The set of refracted path radiances,  $L(\theta_k)$ , is obtained by running the forward model over TES prescribed tangent pressure levels,  $k=0, \dots, N_{ray}$ , with corresponding zenith angles at the TES boresight,  $\theta_k$ . (See Figure 3-5). The TES instrument spatial FOV function for detector

d,  $R_{FOV,d}$  is stored on an angular grid  $\theta_j, j = 0, \dots, N_{FOV}$  appropriate for the trapezoidal integration. The forward model radiances,  $L(\theta_k)$ , are interpolated to match the  $R_{FOV,d}$  grid using a four point Lagrange method for unequally spaced points with continuous first derivatives and are then integrated with  $R_{FOV,d}$  to obtain the effective radiance at the detector. (For the top and bottom rays, three point Lagrange interpolation is used.) The calculated radiance for detector d at the satellite  $L_{sat}$  is given as

$$L_{sat}(\theta_d) = \sum_{j=0}^{N_{FOV}} L(\theta_j) R_{FOV,d}(\theta_j - \theta_d) \Delta\theta_j \quad (3.20)$$

where  $\theta_d = \theta_p + \Delta\theta_d$ ;  $\theta_p$  is the instrument pointing angle, which corresponds to the TES boresight, (defined as the 2B detector array center point),  $\Delta\theta_d$  is the fixed angular difference between this point and the center of detector d, and  $\Delta\theta_j = \frac{1}{2}(\theta_{j+1} - \theta_{j-1})$ . The interpolated radiances corresponding to the angular grid of the FOV function are

$$L(\theta_j) = a_{j,-1} L(\theta_{k-1}) + a_{j,0} L(\theta_k) + a_{j,1} L(\theta_{k+1}) + a_{j,2} L(\theta_{k+2}) \quad (3.21)$$

with Lagrange coefficients  $a_{j,-1}$ ,  $a_{j,0}$ ,  $a_{j,1}$ , and  $a_{j,2}$  defined as follows:

$$a_{j,-1} = p(-1+2p-p^2)/(1+c_1) \quad (3.22)$$

$$a_{j,0} = 1 + p^2[2p-3+(1-p)/(1+c_2)]$$

$$a_{j,1} = p^2(3-2p) + p(1-2p+p^2)/(1+c_1)$$

$$a_{j,2} = p^2(p-1)/(1+c_2)$$

with

$$p = (\theta_j - \theta_k) / (\theta_{k+1} - \theta_k)$$

$$c_1 = (\theta_k - \theta_{k-1}) / (\theta_{k+1} - \theta_k)$$

$$c_2 = (\theta_{k+2} - \theta_{k+1}) / (\theta_{k+1} - \theta_k)$$

To implement this integration efficiently, we switch the order of interpolation and summation over FOV angles to obtain frequency-independent coefficients that are then applied to the ray radiances. Since each  $L(\theta_j)$  interpolation uses 4 rays, we can form the following coefficients:

$$a_{d,k,m} = \sum_j a_{j,m}(\theta_j) R_{FOV,d}(\theta_j - \theta_d) \Delta\theta_j \quad (3.23)$$

where  $k \rightarrow k+1$  when  $\theta_j > \theta_{k+1}$ , *i.e.*, each  $a_{d,k,m}$  is the sum over the FOV angles that use the same group of 4 rays. We then reduce this set of coefficients to ray coefficients by combining terms common to each ray, *e.g.*:

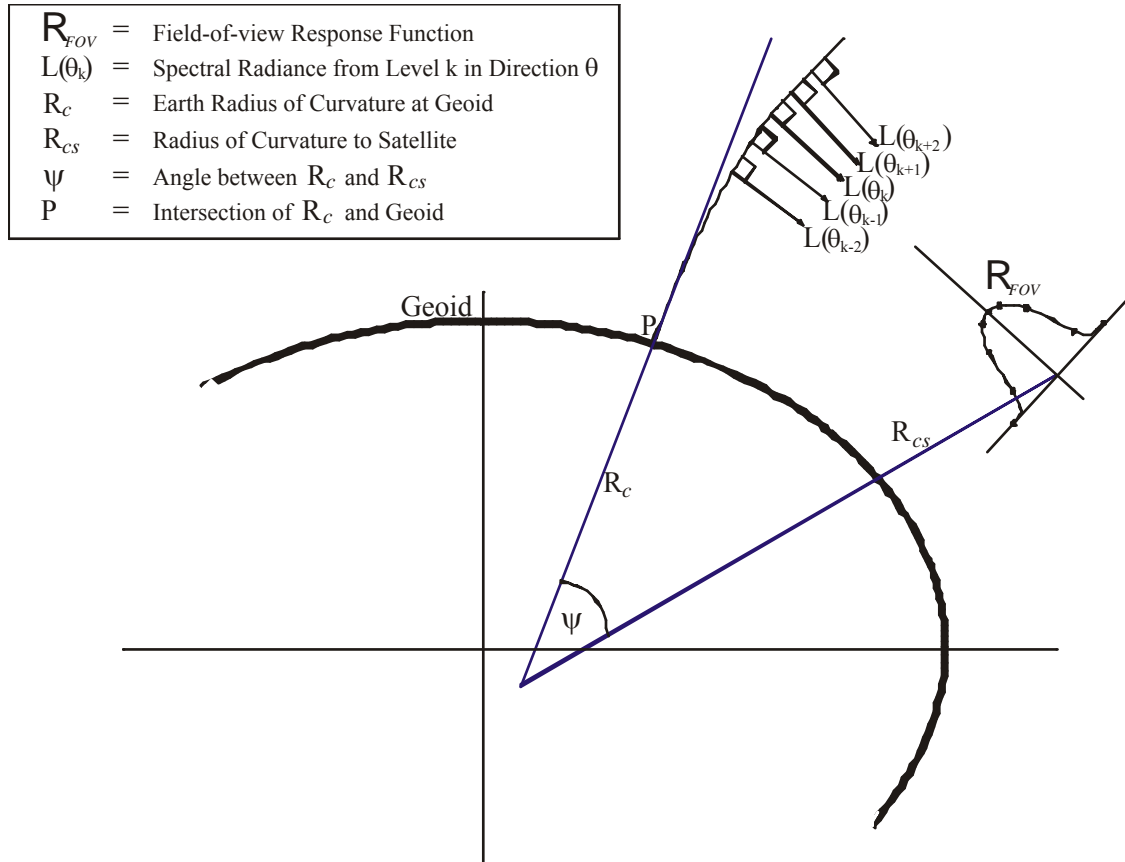
$$\text{for } k \geq 3, \quad b_{d,k} = \sum_{m=1}^2 a_{d,k+m-1,m} \quad (3.24)$$

This allows a significant portion of the FOV calculation to be performed after ray-tracing, when the ray angles are available, but before the radiative transfer, *i.e.*, without frequency dependence. The radiance at each detector is then given by the sum over rays:

$$L_{sat}(\theta_d) = \sum_k^{N_{ray}} b_{d,k} L(\theta_k) \quad (3.25)$$

The analytic partial derivatives of  $L_{sat}$  with respect to  $\theta_p$  for each detector can be calculated at little computational cost from the above expressions. These jacobians are used for the retrieval of the pointing angle.

Figure 3-5: Diagram for TES pointing geometry and FOV convolution in limb mode



### 3.3.7 Absorption Coefficient (ABSCO) Tables

#### 3.3.7.1 ABSCO Table Generation (Using LBLRTM)

The absorption coefficients for a given molecular species as functions of pressure, temperature, and frequency will be pre-calculated and stored using TES LBL (a line-by-line code described in next section) without any line rejection approximation. The corresponding pressures will be the TES forward model layer effective pressures pre-calculated using US standard global average temperature profile. At each pressure, about ten temperatures are calculated at every 10 K. A  $\pm 60$  K temperature band centered at the US standard atmospheric temperature profile [1976 US Standard] is used to limit the temperature grids at a given layer.

Temperature interpolation for total layer optical depth, which is the sum of the layer optical depths for all the molecules considered, will be performed to interpolate OD at pre-defined temperature grids to the TES retrieved atmospheric layer effective temperature. The interpolation scheme will be a three-point Lagrangian method. The pressure interpolation for the layer optical depth will not be required except for the surface layer in the nadir case and for the tangent layer in the limb case. Detailed discussions and validations of this pressure interpolation issue are in section 3.3.7.4.

In the case of tropospheric water vapor, the self-broadening effect cannot be neglected. The H<sub>2</sub>O volume mixing ratio ( $q$ ) is therefore another variable in the ABSCO tables for tropospheric H<sub>2</sub>O. Since the dependence of the H<sub>2</sub>O absorption coefficient on its  $q$  is nearly linear for a given temperature and pressure, we use linear interpolation/extrapolation in  $q$  to calculate the H<sub>2</sub>O absorption coefficient for the associated three temperature values. The temperature interpolation is performed as described above. The two tabulated  $q$  grids are for extremely dry air,  $q_{\text{dry}} = 10^{-8}$ , and for 90% of the saturation  $q$  at the given temperature and pressure grid,  $q_{\text{wet}} = 0.9 * q_{\text{sat}}$ .

In general, by comparison to real time line-by-line calculations of ABSCO, the advantage of table lookup is to greatly speed up the calculation of the required spectral optical depths. However, there are spectral regions in which lines are sparse for a given molecular species. In these cases, the computational cost of the line-by-line calculation may be comparable or faster. TES team has started to study the data storage issue. In the light of using spectral microwindows for TES retrievals and the advancing of the computing technology, the required storage for TES ABSCO table files should be met without much difficulty.

The effect of interpolations (temperature, pressure, and tropospheric  $q$ ) on TES retrievals is being examined thoroughly. Preliminary studies for a nadir case show that comparing to the spectral radiance calculated by line-by-line code, the radiance differences are less than 0.5%. A significant advantage of the ABSCO approach is that the accuracy of the absorption coefficient calculation is not limited in any way by computational cost considerations. In addition, the spectral absorption coefficients are readily amenable to empirical adjustment as atmospheric measurements may suggest for improved retrievals.

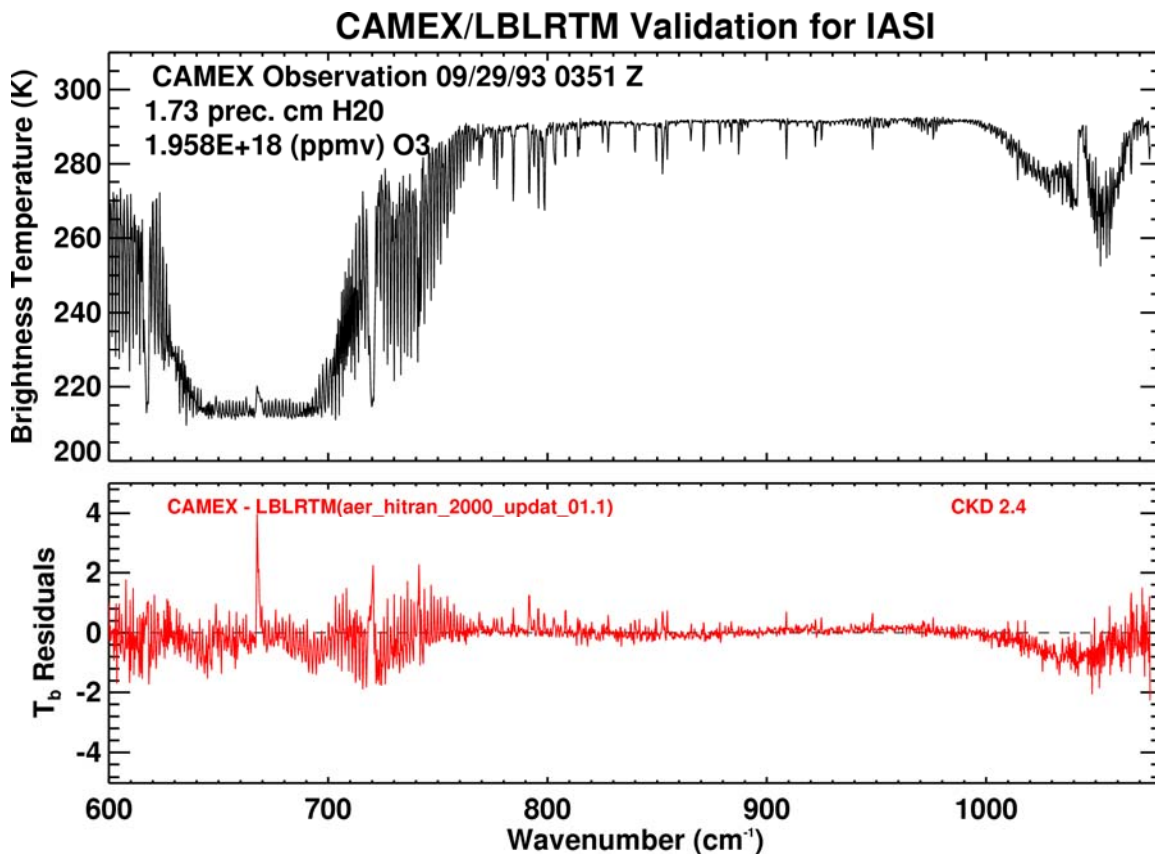
### 3.3.7.2 TES Line-by-Line Optical Depth Code

The line-by-line model to be used to calculate spectral absorption coefficients is TES (TES\_LBL), an advanced version of the module performing the comparable operation in LBLRTM (e.g. Clough *et al.*, 1995) which itself is based on the FASCODE line by line model [Clough *et al.*, 1981]. These models have a long history of validation in the spectral radiative transfer community. TES\_LBL will be used to calculate the spectral absorption coefficients with high algorithmic accuracy. The model is reasonably efficient and is written such that the connection between the physics and the coding is apparent. TES\_LBL will be (1) run off line for the generation of absorption coefficients for a lookup table to be used subsequently in the radiative transfer calculation; or (2) incorporated directly into the forward model to be used as part of the online radiative transfer calculation. In the latter case options may be invoked to accelerate the calculation with some negligible, acceptable loss of accuracy, e.g. line rejection.

TES\_LBL includes the following important attributes: (1) the Voigt line shape is used at all atmospheric levels with an algorithm based on a linear interpolation between precalculated Armstrong [Armstrong, 1967] Voigt functions; (2) all relevant parameters from line databases including HITRAN are utilized including the pressure shift coefficient, the halfwidth temperature dependence and the coefficient for the self-broadening of water vapor; (3) an improved version of the TIPS (Total Internal Partition Sum) program is used for the temperature dependence of the line intensities [Gamache *et al.*, 1990]; (4) the effects of line coupling are treated to second order with the coefficients for carbon dioxide in the 600 - 800  $\text{cm}^{-1}$  region included explicitly [Hoke *et al.*, 1988]; (5) the effects of line coupling are treated to first order with coefficients for  $\text{CO}_2$  following from Strow *et al.*, 1994 for the Q-branch regions of 1932, 2076, 2093 and 2193  $\text{cm}^{-1}$ ; (6) capability to compute quantities for atmospheric layers that are not in local thermodynamic equilibrium (LTE); (7) an explicit formulation is included to address the non-Lorentzian behavior of the wings of carbon dioxide lines. For molecules having an associated continuum, the spectral absorption coefficient calculation utilizes a line shape such that the result of combining the line and continuum contributions provides the correct result.

There have been extensive validations of the LBLRTM model against both upward and downward radiance observations taken by a number of different instruments for a range of atmospheric conditions [Tjemkes *et al.*, 2002, Tobin *et al.*, 1999; Mlawer *et al.*, 1997; Clough and Iacono, 1995; Clough *et al.*, 1992]. The assessment of this model has principally been accomplished under the DoE ARM program. In general, the spectral residuals from these validations have been acceptably low for the purposes of TES. There are spectral regimes where continuing evaluation and improvement is required, including the 650-800  $\text{cm}^{-1}$  carbon dioxide region, the methane region at 1300  $\text{cm}^{-1}$ , and the carbon dioxide bandhead at 2385  $\text{cm}^{-1}$ . The magnitude of the residuals is such that errors including the specification of atmospheric state, line parameters and instrument function are of similar order as those of the model errors presenting a significant challenge to model improvement.

Figure 3-6: Observed HIS spectrum and LBLRTM calculated results in equivalent brightness temperature for CAMEX case (a) and observed-calculated differences (b). The nadir measurement was taken from 20 km on the NASA ER2.



As an indication of the current level of model performance for a portion of the longwave spectral region, we provide in Figure 3 - 5a a radiance spectrum in equivalent brightness temperature obtained with the U. of Wisconsin High-resolution Interferometer Sounder (HIS). The data were taken from the NASA ER2 aircraft during the 1993 Convection and Moisture Experiment (CAMEX) aircraft at an altitude of 20 km in a nadir view over the ocean. The resolution of the unapodized spectrum is  $0.22 \text{ cm}^{-1}$  (hwhm). The absolute radiometric calibration is better than 1K with the relative calibration better than 0.5K. In Figure 3 - 5b we indicate the difference between the brightness temperature spectrum of Figure 3 - 5a and a calculated spectrum utilizing LBLRTM with a version of HITRAN2000 line parameter database with updates (aer\_hitran\_2000\_updat\_01.1), [for HITRAN96 refer to Rothman *et al.*, 1998]. Despite the limitation that the atmosphere utilized for the validation was obtained from radiosonde data that was neither co-spatial nor co-temporal, the comparison is extremely good. The surface temperature and emissivity have been adjusted to minimize the brightness temperature differences in the atmospheric window region. The ozone residuals in the  $1000\text{-}1100 \text{ cm}^{-1}$  region have been improved by utilizing a retrieved ozone profile obtained from the spectral data. The effects of heavy molecules including  $\text{CCl}_4$ , CFC11 and CFC12 have been into account. Carbon dioxide line coupling effects in this region have been accounted for using the temperature dependent first and second order coupling coefficients of Hoke *et al.* [1988]. The

sharp spectral residual at  $668\text{ cm}^{-1}$  is actually due to warmer carbon dioxide in the instrument area rather than to line coupling effects. The regularly spaced spectral residuals in the  $600\text{--}650\text{ cm}^{-1}$  and  $700\text{--}760\text{ cm}^{-1}$  regions are an active area of research as this is the region used for temperature retrieval by TES. The residuals are associated with carbon dioxide and are either due to remaining issues with carbon dioxide line parameters or with problems with the characterization of the instrument function. Since this residual signature is also seen in validations with other sensors (i.e. Scanning-HIS AFWEX spectra) it is currently thought that there are remaining issues more with the carbon dioxide spectroscopy. A contribution to the spectral residuals undoubtedly results from errors in the atmospheric temperature and humidity profiles. Of particular note is the high quality of the spectral radiance data in terms of the photometric calibration, the noise and the spectral calibration.

### 3.3.7.3 Cross-Section Code

Similar to the table look up / temperature interpolation strategy used for the absorption coefficients of line molecules, the cross-section data table for heavy molecules will also be pre-generated at pre-defined pressure and temperature grids. These layer pressure and temperature grids will be the same as the grids used for the line species (section 3.3.7.1). The 3-point Lagrangian interpolation scheme will also be used for temperature interpolation. Section 3.3.8.2 and the associated appendix discussed the method used for temperature/pressure interpolations from the laboratory measurement grids to the TES table  $T/P$  grids.

### 3.3.7.4 Pressure Interpolation

An advantage of using fixed pressure levels bounding the TES forward model atmospheric layers is the ability to ignore the interpolation of species absorption coefficients in pressure at all layers except two: the layer nearest the Earth's surface in the nadir case, and the tangent layer in the limb case. We have conducted a study to examine the changes in layer effective pressures for all the possible layer atmospheric temperature gradients and the effect of pressure interpolation on the simulated spectral radiance.

With a fixed layer boundary pressure, the change in the layer effective pressure ( $\bar{P}$ ) depends mainly on the changes of the boundary temperatures and on the instrument viewing direction. Fifteen averaged temperature profiles of 1997 are calculated using data obtained from the NOAA CDC site (<http://www.cdc.noaa.gov/cdc/reanalysis>): global averaged, global maximum, global minimum, four seasons for tropics, four seasons for mid-latitude, and four seasons for the polar region. We also constructed an extreme temperature profile:  $\pm 20\text{ K}$  on odd and even levels of the global averaged temperature points, respectively. These temperature profiles are used to calculate the layer effective pressures for 24 atmospheric layers between 1000 and 10 hPa for three TES viewing modes: nadir angle = 0, nadir angle =  $45^\circ$ , and a limb viewing case. A standard  $\bar{P}$  profile is calculated using the global average temperature profile and for the nadir angle = 0 case. This standard layer effective pressure profile is the pressure profile used to generate the species absorption coefficient tables.

In the two nadir cases, the layer  $\bar{P}$  for the considered temperature profiles are seen to be extremely close to the standard  $\bar{P}$  profile. The unrealistic temperature profile results in less than

0.3% differences in  $\bar{P}$ , and all the other realistic temperature profiles result even small differences in  $\bar{P}$  (less than 0.11%).

In the limb case, the largest disagreement in  $\bar{P}$  occurs at the tangent layer (~3.2%) for all the temperature profiles, comparing to the nadir standard  $\bar{P}$ . The differences in the layer next to the tangent layer are reduced to about 0.5%. We also found that the effect of different temperature profiles on the limb tangent layer  $\bar{P}$  is very small, which means that we may need a standard limb tangent layer  $\bar{P}$  profile for the limb case if the ~3.2% difference is a problem in the level 2 process.

In conclusion, the standard  $\bar{P}$  profile calculated using global averaged temperature profile for TES nadir ( $\theta = 0^\circ$ ) mode can be used as the pressure grids for the absorption coefficient tables, and the interpolation in pressure is not needed for most cases. The two exceptions are the limb tangent layer and the surface layer. In the case of the limb tangent layer, the absorption coefficient table at the standard limb tangent layer  $\bar{P}$  profile calculated using global averaged temperature profile for TES limb mode may be needed. In the case of the surface layer, which will be thinner than our fixed layers near the surface, the option would be to perform pressure interpolation if it is necessary. The preliminary comparisons of spectral radiances using the standard  $\bar{P}$  profile and the “real”  $\bar{P}$  profiles strongly support this conclusion (the radiance differences for the nadir case are less than 0.05% and for the limb case are less than 0.1%).

### 3.3.8 ABSCO Databases

#### 3.3.8.1 Line Parameters

The line-by-line portion of the TES spectroscopic database contains transitions for individual infrared active molecular species and their isotopomers within the spectral range defined by the TES nadir and limb observations. The numbering of the species, the format and definition of the parameters, and the contents of the TES spectral parameters database are currently identical to those in the 1996 HITRAN compilation [Rothman *et al.*, 1998]. The status and quality of the HITRAN parameters have been reviewed by Rothman *et al.* [1998]. Here we highlight the known, key limitations of the 1996 HITRAN parameters for the molecules and spectral regions of importance to TES, laboratory work in progress, and published results not incorporated in HITRAN. As was done for the ATMOS project [Brown *et al.*, 1996], the TES spectroscopic database will be updated to satisfy the specific needs of the TES project. The discussion, shown in Appendix 3.3.8.1, proceeds on a molecule-by-molecule basis, with the anticipated changes described for each molecule in ascending wavenumber order.

#### 3.3.8.2 Cross-Sections

For heavy molecular species such as chlorofluorocarbons (CFC's), hydrochlorofluorocarbons (HCFCs), SF<sub>6</sub>, N<sub>2</sub>O<sub>5</sub>, and, in part, ClONO<sub>2</sub>, spectral absorption cross-sections measured at atmospheric conditions are required [Massie *et al.*, 1985; Camy-Peyret *et al.*, 1987 and Massie and Goldman, 1992]. This is essential, since the small rotational constants, low vibrations and strong hot bands of such molecules preclude complete modeling of the individual line transitions. The 1986 and 1992 editions of the HITRAN compilation introduced temperature-

dependent cross-sections but neglected the effect of pressure broadening [Ballard *et al.*, 1988, McDaniel *et al.*, 1991; Massie *et al.*, 1991; Cantrell *et al.*, 1988]. More recently, pressure-temperature cross-sections sets have become available [Varanasi *et al.*, 1992a; Varanasi, 1992b; Varanasi, 1992c].

The absorption cross-section,  $\kappa_\nu$ , is defined as

$$\kappa_\nu = (-\ln \mathcal{T}_\nu) / nL \quad (3.26)$$

in terms of the spectral transmittance  $\mathcal{T}$  at wavenumber  $\nu$ , temperature  $T$  and pressure  $P$ , of column density  $n$  along an optical path of length  $L$  (cm). It is presented at several  $(T,P)$  combinations representing atmospheric layers given in commonly tabulated atmospheric models as well as conditions encountered in the polar regions.

Table 3-3 shows the datasets that have been adapted for TES, from an updated set of measurements provided by Varanasi [private communication, 1997]. These form an extension of the cross-sections of CFC-11, CFC12, HCFC-22, and SF<sub>6</sub> provided by Varanasi for 1996 HITRAN [Varanasi and Nemtchinov, 1994; Li and Varanasi, 1994; Varanasi *et al.*, 1994; Rothman *et al.*, 1998], and also include CF<sub>4</sub>. The cross-sections of CCl<sub>4</sub> listed in 1996 HITRAN, which originate from the work of Orlando *et al.* [1992] have been replaced by those of Varanasi, for TES. These cross-sections were measured using a high-resolution Fourier-transform spectrometer. For these species, a spectral resolution of 0.03 cm<sup>-1</sup> was used for most of the broadening pressures used in the experiments, while at 40 torr and lower 0.01 cm<sup>-1</sup> was used. The data were obtained at temperatures between 180 and 296 K and are free from instrumental distortion, since the spectra were recorded at a spectral resolution that was sufficiently high at each broadening pressure used.

**Table 3-3: IR cross-section data prepared for TES**

<i>Molecule</i>	<i>Wavenumber Range (1/cm)</i>	<i>Temperature Range (K)</i>	<i>Pressure Range (torr)</i>	<i>Number of P,T sets</i>
CCl <sub>4</sub>	770-812	208-297	8-760	32
CFC-11	810-880	190-296	8-760	55
(CCl <sub>3</sub> F)	1050-1120	190-296	8-760	55
CFC-12	810-965	190-296	8-760	51
(CCl <sub>2</sub> F <sub>2</sub> )	1040-1200	190-296	8-760	51
HCFC-22 (CHClF <sub>2</sub> )	760-860	216-294	40-760	7
SF <sub>6</sub>	925-955	216-295	25-760	7
CF <sub>4</sub>	1250-1290	180-296	8-760	54
HFC134a (CFH <sub>2</sub> CF <sub>3</sub> )	1000-1350	253-287	0	3

For the purpose of TES codes, the cross-sections, which are originally given at different spacings (chosen according to resolution and pressure) were interpolated to a constant step of 0.0025 cm<sup>-1</sup>.

A special P-T interpolation was devised for conditions different from the laboratory data. Table 3-3 shows the data sets prepared on the TES system and Appendix 3.3.8.2 describes the P-T interpolation program XSFINT.

The data are stored in HITRAN format, i.e. as separate files for each individual molecule. Each portion of the file corresponding to a particular temperature-pressure pair begins with a header that contains information on the wavenumber ( $\text{cm}^{-1}$ ) range, number of cross-section data in this set, temperature (K), and pressure (torr). The maximum value of the absorption cross-section ( $\text{cm}^2/\text{molecule}$ ) and additional information containing the reference to that observation are also presented in each header. The wavenumber spacing of the cross-section listings is uniform for each of the pressure-temperature sets, and is determined by taking the difference between the maximum and minimum wavenumber and dividing by the number of points (cross-section data in this set).

The rest of the molecular cross-sections sets are taken from the 1996 HITRAN database, which, compared to 1992 HITRAN, provides an update for  $\text{ClONO}_2$ . In addition to the  $\text{ClONO}_2$   $v_4$  line parameters, new cross-sections for the  $\text{ClONO}_2$  in the  $1265\text{-}1325\text{ cm}^{-1}$  region at 201, 211, and 222 K are available from 1996 HITRAN, as provided by Orphal *et al.* [1994].

The increased use of hydrofluorocarbons (HFCs), which are expected to replace CFCs and HCFCs in many applications in order to reduce the deleterious effects of released chlorine on the atmospheric ozone layer, will add another absorber in the IR 'window' region, 8-12  $\mu\text{m}$ . Cross-sections data for a number of HCFCs have become available [Clerbaux *et al.*, 1993; Smith *et al.*, 1996]. More recently, Smith *et al.* [1998] determined the cross-sections of HFC-134 ( $\text{CHF}_2\text{CHF}_2$ ) and HFC-143a ( $\text{CF}_3\text{CH}_3$ ). All of these data are already available on the GEISA database [Jacquinet-Husson *et al.*, 1998] and will also be available on a future edition of HITRAN. At this time we prepared in TES format the cross-sections of HFC-134a (from Clerbaux *et al.*, 1993) which is considered as one of the most popular HCFC's.

### 3.3.8.3 Aerosols

The HITRAN 1996 compilation [Rothman *et al.*, 1998] contains auxiliary tables in ASCII for various atmospheric particles. The index of refraction tables include water and ice (the composition of cloud particles), aqueous sulfuric acid (the composition of volcanic aerosols), and nitrate acid trihydrate and aqueous  $\text{HNO}_3/\text{H}_2\text{O}$  (possible compositions of polar stratospheric clouds). The tables have individual wavenumber ranges, increments, and data formats. A description of the individual files is reported in Table 10 of Rothman *et al.* [1998]. Massie [1994] reviewed the indices of refraction which form the basis of the files on HITRAN 1996 [Rothman *et al.*, 1998]. Note that most of the available measurements were obtained only at room temperature.

The emission measurements obtained by TES will display enhanced radiances due to the scattering and absorption by aerosol particles. As is well known, sulfate aerosol injection into the stratosphere after a major volcanic eruption will greatly increase radiance levels. At such times, strong aerosol bands appear throughout infrared limb spectra [Rinsland *et al.*, 1994].

### 3.3.8.4 CKD 3.0 Continuum

A new continuum model is being developed for TES. This model includes continua due to water vapor, carbon dioxide, oxygen and nitrogen. The water vapor continuum [Clough *et al.*, 1980 and Clough *et al.*, 1989] and carbon dioxide continua are developed and utilized such that when the continuum contribution is added to the line by line component, agreement with observation is achieved. These continua have slow spectral dependence and known thermodynamic scaling. The continua for oxygen [Thibault *et al.*, 1996] and nitrogen [Lafferty *et al.*, 1996] are due to collision induced effects resulting from collisions with the respective molecule and the molecules comprising the air.

The water vapor continuum plays an important role in atmospheric radiative transfer providing increased opacity between spectral lines over the full spectral region from the microwave to the visible. The continuum is important to the physical solution of the inverse problem, the remote sensing of atmospheric state to retrieve temperature, water vapor, and trace species profiles as well as surface properties. There are two components to the continuum: the self-broadened continuum ( $C_s$ ), dependent on the square of the partial pressure of water vapor, and the foreign-broadened continuum ( $C_f$ ), dependent on the product of the water vapor partial pressure and the dry air pressure. As a consequence the self-broadened continuum tends to be more important in the lower atmosphere while the foreign-broadened continuum tends to be more important in the middle to upper troposphere. A comprehensive continuum model based on a single line shape for all transitions from the microwave to the visible has provided generally acceptable results [Clough *et al.*, 1989; hereafter CKD]. The general formulation for the absorption coefficient associated with the continuum is given by

$$\kappa_c = \nu \tanh(hc\nu / 2k_B T) \left[ (\rho_{H_2O} / \rho_0) \tilde{C}_s(T) + (\rho_{air} / \rho_0) \tilde{C}_f(T) \right] \quad (3.27)$$

with the usual definitions.

The CKD model has evolved with empirical adjustments over time to provide improved agreement with measurements (e.g. Clough, 1995). The current version of the model, CKD\_2.2, has been modified on the basis of two recent observations: (1) the measurement of the downwelling radiance at Kavieng, New Guinea by Han *et al.* [1997] which indicated that the self-broadened continuum gave rise to an 8K error in brightness temperature at 950 cm<sup>-1</sup> for an atmosphere with ~6 precipitable cm of water vapor; and (2) a clear indication that the foreign continuum was in error in the wings of the 1600 cm<sup>-1</sup> water vapor band as observed by Revercomb and colleagues at the U. of Wisconsin. These modifications are significant in the context of remote sensing from space. Of interest is the fact that the spectral character of the continuum in the 950 cm<sup>-1</sup> window has the effect of decoupling the atmospheric radiance of the moist atmosphere in the boundary layer from the surface emission, thereby significantly improving the accuracy with which boundary layer water vapor and surface brightness temperature can be retrieved (given the spectral emissivity of the surface). Examples of the role of the continuum for atmospheric observations may be found in Clough *et al.* [1992] and Mlawer *et al.* [1997].

As a result of more stringent accuracy requirements for remote sensing applications and with the availability of improved laboratory measurements and atmospheric observations, an entirely new water vapor continuum formulation is being developed [Mlawer *et al.*, 1999]. The basis for the new formulation is an important new set of laboratory measurements by Tobin *et al.*, 1996. The laboratory measurements are for 296K. The foreign continuum coefficient is taken as temperature independent consistent with the CKD model. The temperature dependence of the CKD model has been adopted for the self continuum. The new formulation involves not only line wing effects but also two types of collision-induced effects, one with high spectral content and the other with very slow spectral characteristics. The principal consequences for remote sensing are with respect to the foreign continuum, important in the upper troposphere for the retrieval of water vapor and for the background spectral radiance for retrieval of trace species including NO. An interim version of the new continuum is currently available and has been applied to atmospheric observations in the arctic by Tobin *et al.* [1999] with encouraging results. The agreement between observation and LBLRTM calculation with the new continuum in the 400-500  $\text{cm}^{-1}$  region in an extremely cold environment provides confidence that the model will perform well in the middle –upper troposphere in the 1200-2000  $\text{cm}^{-1}$  region of importance for TES retrievals. The new formulation has significantly higher spectral content than the CKD continuum model. It is anticipated that the self continuum coefficients will be stored on a 0.5  $\text{cm}^{-1}$  grid and the foreign continuum on a 0.1  $\text{cm}^{-1}$  grid.

### 3.4 JACOBIANS

The sensitivity of spectral radiance at the satellite to the perturbations of retrieved parameters included in the retrieval vector is the Jacobian matrix,  $\mathbf{K}$ . In general,  $\mathbf{K} = \partial\mathbf{F}/\partial\mathbf{x}$ , where  $\mathbf{F}$  is the forward model radiance and  $\mathbf{x}$  represents a retrieved parameter, such as temperature at level  $l$ . In our retrievals, we cannot assume we are close to a linear solution. Therefore, Jacobians are recalculated for each iteration of a retrieval, using updated parameters.

#### 3.4.1 Finite Difference

Evaluating Jacobians using a finite difference method is straightforward. For example,  $\mathbf{K}$  can be calculated as  $[\mathbf{F}(\mathbf{x}+\Delta\mathbf{x}) - \mathbf{F}(\mathbf{x})]/\Delta\mathbf{x}$ , where  $\Delta\mathbf{x}$  is a small perturbation of parameter  $\mathbf{x}$ . If terms  $\mathbf{F}(\mathbf{x}+\Delta\mathbf{x})$  are calculated for all retrieved parameters by carrying out forward model many times, the algorithm is not very efficient considering that many layer quantities (see 3.3.1.3 and 3.3.1.4) will be unnecessarily calculated over and over again. The computation, if not optimized, can be expensive and the accuracy of the derivatives is more prone to numerical error and nonlinear contributions. For these reasons, we compute analytic Jacobians for operational retrievals and retain the finite difference method for validating analytic Jacobians. Although accelerated methods for computing finite difference are possible, they have very low development priority since they would not be used operationally. For validating analytic Jacobians, symmetric finite differences will be used, where the finite difference is computed with both positive and negative perturbations to the retrieval parameter.

#### 3.4.2 Analytical

In evaluating analytic expressions for the terms in the Jacobian matrix, there are some cases where approximations represent a significant computational savings with only marginal impact

on accuracy. We have never placed a requirement on the accuracy of analytic jacobians. From experience, accuracy around 5% is sufficient for retrieval convergence to a solution within estimated error, in most cases. However, jacobians are also used to compute retrieval errors, as well as in assimilation (L4) algorithms. Data assimilation would probably place the most stringent requirements on jacobian accuracy, but algorithms have not yet been developed for the assimilation of TES data. A jacobian accuracy requirement is therefore TBD. For this version of the L2 ATBD, we will set a goal of 1% accuracy (at the maximum absolute value in a frequency range) for analytic jacobians as compared to finite difference.

### 3.4.2.1 Temperature and Gas Concentrations

Due to the form of the radiative transfer equation (equation 3.8), the analytic derivative of the radiance at the satellite with a change in parameter  $x_l$  at level  $l$ , is most expeditiously obtained in terms of associated layer quantities, so that we have

$$\frac{\partial L_{sat}}{\partial x_l} = \sum_j \frac{\partial L_{sat}}{\partial \bar{x}_j} \frac{\partial \bar{x}_j}{\partial x_l} \quad (3.28)$$

in which  $x_l$  is an element of the retrieval vector associated with level  $l$  and  $\bar{x}_j$  is the associated layer quantity for layer  $j$ . Note that in general,  $x$  may be mixing ratio (log mixing ratio) or temperature in this context.

In this section we focus on the computation of  $\frac{\partial L_{sat}}{\partial \bar{x}_j}$ , noting that  $\frac{\partial \bar{x}_j}{\partial x_l}$  is independent of wavenumber. (These layer-to-level partial derivatives are discussed in Appendix A3.4.) For the layer quantities, it is useful to separate the jacobian calculation into partial derivatives with respect to layer total optical depth ( $\tau_l$ ) and Planck function ( $B_l$ ) via the chain rule. Differentiating Eq. 3.8, we obtain

$$\frac{\partial L_{sat}}{\partial x_l} = \frac{\partial L_{sat}}{\partial \tau_l} \frac{\partial \tau_l}{\partial x_l} \quad (3.29)$$

for gas species, and

$$\frac{\partial L_{sat}}{\partial T_l} = \frac{\partial L_{sat}}{\partial \tau_l} \frac{\partial \tau_l}{\partial T_l} + \frac{\partial L_{sat}}{\partial B_l} \frac{\partial B_l}{\partial T_l} \quad (3.30)$$

for layer temperature  $\bar{T}_l$ . This approach has the advantage of relatively simple expressions for the derivatives of  $\tau_l$  with respect to log mixing ratio and temperature. It is also compatible with the modularity designed into our code where quantities associated with optical depth are computed first to determine whether they can be reused from one ray calculation to the next, while quantities associated with layer to layer radiative transfer are used locally in different function. Appendix A3.4 describes the above terms in detail. In summary, the partials for all gas species but H<sub>2</sub>O have very simple jacobians, while H<sub>2</sub>O has additional terms for line self-

broadening, continuum and integrated path amount dependence. Temperature jacobians include terms for gas species line absorption, continuum absorption, dependence of the integrated path amount and Planck (or effective Planck) function dependence. For absorption coefficient tables, the temperature jacobians for species line absorption are a straightforward differentiation of the temperature interpolation coefficients.

### 3.4.2.2 Surface and Opaque Cloud Boundary Properties

For lower boundaries that are either the earth's surface or opaque clouds, we will retrieve a single "surface" temperature,  $T_{sfc}$ , and coarse frequency resolution functions for emissivity,  $\varepsilon(\nu)$ , and possibly albedo,  $\alpha(\nu)$ . The Jacobians for these parameters are calculated analytically. Derivations are straightforward given that the surface contribution to the total radiance is a separate term in the radiative transfer equation 3.8. Emissivity and albedo functions will be expressed as tabulated quantities on a coarse spectral grid ( $10 \text{ cm}^{-1}$  spacing). Assuming piecewise linear interpolation, for tabulated  $\varepsilon(\nu)$  on a frequency grid with any two adjacent table points at  $\nu_a$  and  $\nu_b$ , the emissivity at  $\nu$ , where  $\nu_a \leq \nu \leq \nu_b$ , is given by

$$\varepsilon(\nu) = \left[ \frac{\nu_b - \nu}{\nu_b - \nu_a} \right] \varepsilon_a + \left[ \frac{\nu - \nu_a}{\nu_b - \nu_a} \right] \varepsilon_b \quad (3.31)$$

Assuming the albedo is defined on the same frequency grid, we have the following surface Jacobians:

$$\frac{\partial L_{sat}}{\partial T_{sfc}} = \varepsilon(\nu) \frac{\partial B}{\partial T_{sfc}} \mathcal{T}_{0,L} \quad (3.32)$$

$$\frac{\partial L_{sat}}{\partial \varepsilon_a} = \left[ \frac{\nu_b - \nu}{\nu_b - \nu_a} \right] B(\nu, T_{sfc}) \mathcal{T}_{0,L} \quad (3.33)$$

$$\frac{\partial L_{sat}}{\partial \varepsilon_b} = \left[ \frac{\nu - \nu_a}{\nu_b - \nu_a} \right] B(\nu, T_{sfc}) \mathcal{T}_{0,L} \quad (3.34)$$

$$\frac{\partial L_{sat}}{\partial \alpha_a} = \left[ \frac{\nu_b - \nu}{\nu_b - \nu_a} \right] L_0^\downarrow \mathcal{T}_{0,L} \quad (3.35)$$

$$\frac{\partial L_{sat}}{\partial \alpha_b} = \left[ \frac{\nu - \nu_a}{\nu_b - \nu_a} \right] L_0^\downarrow \mathcal{T}_{0,L} \quad (3.36)$$

### 3.4.2.3 Pointing

In the limb case, retrieving instrument pointing angle needs to be carried out as part of the profile retrievals. Recall that the TES forward model radiances for the rays along the field of view directions starting from pre-defined tangent pressure levels are interpolated in zenith angle and convolved with the instrument field of view function (section 3.3.6). Only one angle,  $\theta_p$ , the instrument pointing angle (e. g. the zenith angle for the optical axis) determines the relative "alignment" between the pixel dependent FOV functions and the ray radiances. Since each detector has  $\theta_d = \theta_p + \Delta\theta_d$ , the derivatives of detector radiance with respect to  $\theta_p$  are

$$\frac{\partial L_{sat}}{\partial \theta_p} = \frac{\partial L_{sat}}{\partial \theta_d} \quad (3.37)$$

Formulas for this analytic jacobian are given in Appendix A3.4.7. These derivatives with respect to pointing angle have been validated using finite difference jacobians where the finite difference is computed by perturbing the pointing angle, which adjusts the FOV functions relative to the forward model rays, then performing the FOV convolution again. The finite difference jacobian is the change in radiance from the perturbed and reference case divided by the delta angle.

## **3.5 RETRIEVAL**

### **3.5.1 General Strategy**

Our goal is to have a single, flexible, efficient retrieval code that can be used in a variety of ways under control of a strategy table. The approach is to use non-linear least squares spectral fitting of retrieval parameters, based on the so-called optimal estimation technique [Rodgers, 1970]. The retrieval parameters will be retrieved in a series of steps, with retrieved quantities from one step usually feeding the next as fixed inputs. In some cases, parameters will be retrieved in multiple steps, such as in initial guess refinement (see section 3.5.4.2).

Each limb or nadir target scene will be treated independently. This is the simplest approach, and allows partial results from incomplete observation sets. Computational gains from parallelization can be achieved by processing multiple target scenes at the same time.

#### **3.5.1.1 Strategy Table Selection**

The particular strategy table that it will be used to retrieve a target scene will be selected based on the following parameters:

- view mode (nadir or limb)
- initial guess override (to specify an initial guess from a previous retrieval result)
- surface type (land, ocean, or cloud)

In the future, other table selection parameters may be identified. At present, the basic difference between strategy tables is the retrieval order and species retrieved. However, different strategy tables may also specify different constraint types, initial guess sources, or retrieval control parameters. The flexibility of the strategy tables may be used in production, but will also be used for testing and comparing new retrieval strategies.

#### **3.5.1.2 Target-level Suppliers**

The task of assembling data to run retrieval steps is divided up into a conceptual division of suppliers. Each supplier is designed to operate with a degree of independence to accomplish a specific task. The target level suppliers assemble the data needed before the first retrieval step begins, and create data which be used throughout all the retrieval steps. The step level suppliers assemble the data needed for each retrieval step, and which may vary from step to step. Some suppliers that are conceptually step-level are moved to the target level because their data is

needed before the first retrieval step, for example microwindows. Microwindows for all steps are determined at the target level so that all FM species list can be determined and so that the FM radiance can be generated for simulation mode.

A figure showing the suppliers and supplier dependencies is shown in Figure 3-7.

The target level suppliers are (see appendix for descriptions):

- Strategy Table
- Surface pressure
- Forward model pressure
- Target level full state vector (initial guess)
- True full state vector
- Target level emissivity
- Target level map
- Simulated spectrum
- Measured spectrum
- Target level microwindows definitions
- Target level error covariance

### 3.5.1.3 Step-level Suppliers

The step level suppliers assemble the data needed for one retrieval step. A step will be defined by the following parameters:

- quantities to be placed in the retrieval vector
- first guess for each of these quantities
- *a priori* for each of these quantities
- quantities to be used as forward model parameters
- forward model parameters
- numerical method to be used to minimize the cost function
- subset of the measured spectrum to be used (may be detector-dependent)
- other items TBD.

These pieces of information will be collected by step level suppliers, or are specified as step control parameters in the strategy table. The step level suppliers are (see appendix for descriptions):

- Step level map
- Step level microwindows definitions
- A priori  $x_a$ .
- A priori constraint
- Microwindows radiances
- Emissivity a priori
- Step level full state vector
- Retrieval levels

The suppliers must collect data in a particular order, because many depend on data from other suppliers. The ordering and dependencies are shown in Figure 3.7.

**Figure 3-7: Supplier Dependencies**

<u>Order</u>	<u>Supplier (Sub supplier)</u> → means an either/or case for supplier choice	<u>Dependency</u>
1	Target Scene Attributes	
2	Strategy Table	Target Scene Attributes
3	Target Level Microwindows Definitions	Target Scene Attributes Strategy Table
4	Target Level FMPressures (includes Target Level Surface Pressure)	Strategy Table
5	Target Level Map (includes Target Level Retrieval Levels)	Target Level FMPressures Strategy Table
6	Target Level FSV (includes Target Level Emissivity)	Strategy Table Target Level Microwindows Definitions Target Level FMPressures Target Level Map
7	Target Level TFSV (includes Target Level Emissivity)	Strategy Table Target Level Microwindows Definitions Target Level FMPressures Target Level Map
8	Target Level Error Covariance (includes Emissivity A Priori Climatological Covariance)	Strategy Table Target Level FMPressures
9	→Target Level Full Apodized Measured Spectrum (FAMS) →Target Level Full Apodized Measured Spectrum [ <i>Simulation mode</i> ]	Strategy Table Target Level TFSV Target Level FMPressures Target Level Microwindows Definitions
10	Target Level Cloud <sup>1</sup>	Strategy Table Target Level FSV Target Level Microwindows Definitions

-----below is repeated for every step-----

11	Step Level Map	Strategy Table Target Level Map
12	Step Level FSV	Target Level FSV
13	Step Level A Priori Constraint Vector (includes Emissivity A Priori Constraint Vector)	Strategy Table Target Level FMPressures Step Level Map Step Level FSV
14	Step Level A Priori Constraint Matrix (includes Emissivity A Priori Constraint Matrix)	Strategy Table Target Level FMPressures Step Level Map Step Level FSV

<sup>1</sup> If a cloud is detected, update surface pressure based on met-data and observed data, then return to # 2, to get a different Strategy Table, then update and/or redo the other supplier data.

		Step Level A Priori Constraint Vector
15	Microwindows Radiances	Target Level Microwindows Definitions Target Level FAMS

### 3.5.1.4 Operational Support Products

Operational Support Products (OSP's) are defined as any files or databases that are needed to perform L2 processing. There are two types of OSP's. Internal OSP's are generated by the science team for use by the different suppliers. External OSP's will be used directly by the suppliers. The remainder of this section is a list and brief description of the more important OSP's.

#### 3.5.1.4.1 Initial Guess

The main sources for the initial guess are the *a priori*, and the results from a nearby retrieval. The nearest previous retrievals include the previous one along the orbit (about 530 km), one at the same latitude on an adjacent orbit (orbital spacing is about 24°), or one at the same latitude on the previous day. It is of course possible that any of these was not retrieved due to cloudy pixels. The available information may be combined by weighting each according to its estimated precision. The initial guess based on one or more of these pieces of information will then be refined using a simpler, faster and less accurate retrieval than the full resolution non-linear iteration.

#### 3.5.1.4.2 Climatology

The development of climatologies for all retrieved and forward model species is still in progress. The climatologies for the different chemical species are needed to provide

- An initial guess for the retrieval of a given species as mentioned previously.
- “True State” profiles for a given species if there is a need to do a simulated retrieval
- Formulation of *a priori* covariance matrices.

Development of a climatology for any given species will involve combining tropospheric and stratospheric data sets. As many current and future atmospheric data sets that might be relevant for a given species will be considered in developing a climatology. However for certain atmospheric species it may be necessary to use 3D model fields as a climatology. Information on how the climatologies are assembled and the spatial/temporal gridding of the data will be made available once they are better defined.

#### 3.5.1.4.3 Meteorological Data

The meteorological data used as inputs for the retrieval will be an external OSP. The most likely source of the data will be the GSFC Data Assimilation Office (DAO). The accuracy of the meteorological data, particularly mean sea level pressure, will affect the accuracy of the retrieval products. Because of the importance of the meteorological data, we are continuing to evaluate sample products from DAO, European Center for Medium-Range Weather Forecasts (ECMWF)

and National Center for Environmental Prediction (NCEP). The meteorological data needs to provide the retrieval strategy suppliers with the following parameters

- Reference Pressure: The mean sea level pressure from the meteorological data, will be used along with the digital elevation model (section 3.3.2.3) to provide the reference surface pressure for a given target location.
- Temperature profiles (including at the surface) to use as an initial guess for a temperature retrieval.
- Tropopause height, which can either be provided or calculated from the temperature profile. This will be used in developing initial guesses for atmospheric species with little tropospheric variation (e.g., methane).
- Water profiles, that will be combined with a stratospheric (and possibly upper tropospheric) water climatology to provide *a priori* information.

In order to provide a best initial guess for temperature and water, we are hoping to obtain meteorological data on a  $0.5^\circ \times 0.5^\circ$  spatial grid. Many other meteorological data fields will be used for data analysis purposes.

#### 3.5.1.4.4 *A priori Climatology Covariance Matrices*

These will be calculated as the climatologies are developed and will be used in error analysis and possibly in determining *a priori* constraints. The covariances will be calculated using the full TES pressure level grid, resulting in  $87 \times 87$  matrices.

#### 3.5.1.4.5 *Microwindows*

Microwindows and corresponding spectral masks will be developed for all retrieval species and made available to the suppliers (see section 3.5.7).

#### 3.5.1.4.6 *Land Characteristics and Surface Emissivity Properties Databases*

These databases must be provided to calculate an *a priori* surface emissivity for retrievals over land (see section 3.3.2.1).

#### 3.5.1.4.7 *Other OSP's*

More quantities that will need to be specified (calculated) and then provided to the suppliers include the maps and inverse maps (section 3.5.2), *a priori* constraints (section 3.5.3), forward model pressure levels (section 3.2.3) and retrieval levels (species and latitude dependent).

### 3.5.1.5 Retrieval Step Scenarios

The following table shows some retrieval step scenarios. These steps are specified in the strategy table and their content is flexible, both with regards to what is retrieved and to the parameters controlling the retrieval. These strategies will be modified in the light of experience with real data.

Table 3-4: Sample Retrieval Step Scenarios

Viewing_Mode	NADIR	NADIR	LIMB
Surface	LAND/CLOUD	OCEAN	-
Selected table →	<b>Table 1</b>	<b>Table 2</b>	<b>Table 3</b>
Retrieval steps	1 <b>TSUR &amp; EMIS</b>	<b>TSUR</b>	<b>pointing</b>
	2 <b>TATM</b>	<b>TATM</b>	<b>TATM</b>
	3 <b>H2O</b>	<b>H2O</b>	<b>H2O</b>
	4 <b>TATM &amp; H2O</b>	<b>TATM &amp; H2O</b>	O3
	5 O3	O3	CH4
	6 CH4	CH4	CO
	7 CO	CO	HNO3
	8		NO

Note: **BOLD** indicates retrieval order is important.

Retrieval tables 1 and 2 show the difference in strategy between a land and an ocean target scenes retrieval. The difference is whether emissivity (EMIS) is retrieved. For TES nadir data taken over water, we would fix the emissivity parameters to the known water emissivity spectrum and retrieve only the “skin” temperature (TSUR). This may also be possible for some well-characterized scenes over ice. For land targets, the emissivity spectrum will be retrieved using reasonable first guess emissivity values (described in section 3.3.2.1). We have successfully performed land emissivity retrievals with silicate features using AES data and we found that emissivity parameters need additional constraints so that they are limited to physical values (*i.e.*, they must be less than 1). These constraints can be specified in the strategy table. The above Strategy Tables are examples which show the flexibility of the Tables to specify any combination of retrieval species in any order.

All the sample tables in Table 2-1Table 3-4 show each species retrieved once. However, O<sub>3</sub> (or any other species) may be retrieved in more than one step. Below shows nadir retrieval step scenario using initial guess refinement for O<sub>3</sub>. O<sub>3</sub>-IG-refine is an initial guess refinement step (see section 3.5.4.2). This step will have a different map and possibly different microwindows than the second O<sub>3</sub> step, all of which can be specified in the strategy tables. These details are not shown here but are easily specified in the strategy tables.

Retrieval steps
<b>EMIS &amp; TSUR</b>
<b>TATM</b>
<b>H2O</b>
<b>TATM &amp; H2O</b>
<b>O3-IG-refine</b>
<b>O3</b>
CH4
CO

Additionally, some final steps may be done following the above retrieval steps:

- retrieval of all species simultaneously for more improvement or error analysis
- full filters radiance calculations for quality control

In the limb case, the filters radiance calculation will be done for each pixel. In the nadir case, this will actually be a retrieval of surface emissivity using the already determined atmospheric state.

### 3.5.1.6 Strategy for Limb Pointing Retrieval Limb

The central problem to be addressed from the spacecraft is the pointing direction of the 2B1 reference focal plane. Once this is known, then the pointing of all pixel elements is established given predetermined focal plane properties. The general strategy will be to utilize the radiance spectrum associated with a pixel having a projection in the upper troposphere to minimize the effects of clouds and to perform a simultaneous retrieval of pointing angle and temperature.

The procedure for establishing the radiance field at the satellite and the relevant Jacobians with respect to pointing angle and to temperature is described elsewhere. The initial guess for the pointing angle will be obtained from the encoder associated with the platform spacecraft attitude system. For this stage of the pointing angle retrieval, there will be three elements for the retrieval state vector: (1) the pointing angle, (2) a shift in level temperature for all tangent rays included in the FOV, and (3) a shift in temperature lapse rate for all tangent rays included in the FOV. It will probably be necessary to retrieve temperature profiles somewhat above the tangent layers, but this can be handled in a fashion analogous to the line of sight retrievals appropriate to the nadir case. The spectral region will be that associated with carbon dioxide for which the mixing ratio is assumed known, Figure 3-8, and one in which water vapor plays a minimal role.

The radiance at the satellite is calculated for each tangent ray required for the FOV convolution. The tangent levels associated with all tangent rays are those of the forward model pressure grid. The zenith angle of

$$n R \sin(\theta) = \text{Constant} \quad (3.38)$$

$$n_t(R_c + z_t) = R_{cs} \sin(\theta_s) \quad (3.39)$$

$$\theta_s = \text{asin} \{ n_t(R_c + z_t) / R_{cs} \} \quad (3.40)$$

The dependence of the radiance field on the zenith angle at the satellite,  $\theta_s$ , is nonlinear and is retrieved as an element of the retrieval vector in the nonlinear retrieval procedure. The Jacobian required is obtained analytically in the course of the FOV convolution. Results from a simultaneous pointing angle / temperature retrieval are provided in Table 3-5. The method, as evaluated through simulations, has been established to be robust and provides excellent accuracy.

Relevant geometrical quantities and horizontal offsets in the direction of the satellite are provided in Table 3-6 as a function of tangent height. These offset values enable the evaluation

of the effects of using a single column for the hydrostatic equation. It may be noted that the FOV is 25 km wide in the horizontal direction perpendicular to the chief ray. The effect on the pointing / temperature retrieval due to an error in the tangent altitude obtained from the hydrostatic equation is small.

This simultaneous retrieval approach should be more critically evaluated with respect to measurement errors greater than those given by the source radiance and with respect to the expected sources of systematic error. The use of pixels in other atmospheric regimes such as the lower stratosphere needs to be explored since there would presumably be less cloud. Also to be explored is the inclusion of the pointing angle in the retrieval state vector for the global fit associated with the retrieval of the temperature field. The relative registration of the four focal plane arrays is determined by the on-board spatial calibration. It may also be tested in space by viewing sharp radiative discontinuities in the scene with both nadir and limb views. These discontinuities can be associated with discontinuities in cloud fields for both the limb and nadir mode and in surface properties (land/ocean) for the nadir view. The relative registration of the pixels is independent of the viewing mode so that there should be consistency between pixel registrations obtained from the two modes. Also to be explored is the retrieval of pointing angle using other spectral regions associated with the other focal planes to further evaluate the consistency of pointing angle among the focal plane arrays.

Figure 3-8: AFGL Mid Latitude Summer Profiles

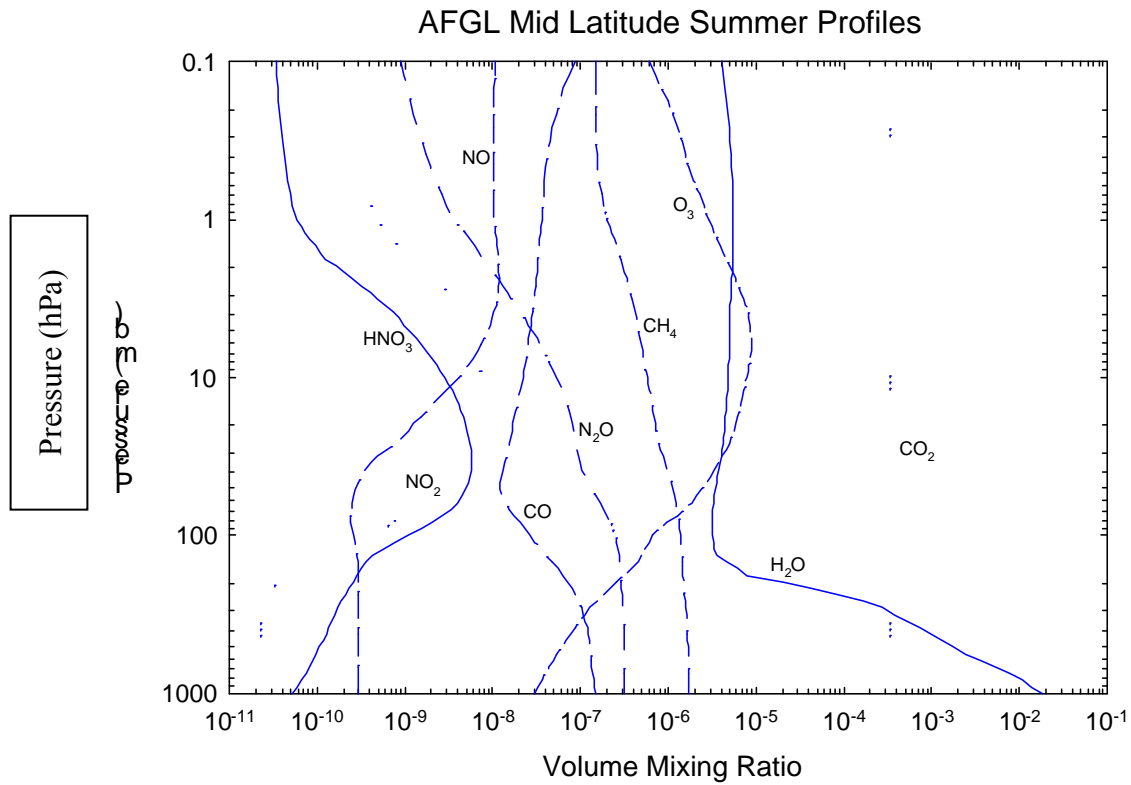


Table 3-5: Retrieval results for temperature and tangent point for central ray of pixel 11 with TES FOV (tangent height = 11.5 km).

Case	Parameter		Perturbation	Retrieved	Difference	Error (1 $\sigma$ )	
1c	Temperature	(K)	1.0	1.00	0.00	0.02	
	(700-800 cm <sup>-1</sup> )	Tangent Point	(m)	500.0	501.00	1.00	1.96
1d	(NESR*10)	Temperature	(K)	1.0	0.97	0.03	0.20
	(700-800 cm <sup>-1</sup> )	Tangent Point	(m)	500.0	506.40	6.40	19.60

**Table 3-6: Quantities related to the ray trace from the tangent point to the satellite as a function of tangent height. Refraction is included in the ray trace.**

Tangent Height		$\theta_s$	$\sin(\theta_s)$	$\Psi$	bending	Horizontal Offset	
(km)		(deg)		(deg)	(deg)	(km)	
37.95		115.078	0.90574	17.137	0.003	-163.9	
36.80		115.099	0.90557	17.086	0.003	-150.3	
35.65		115.121	0.90541	17.035	0.004	-142.3	
34.50		115.143	0.90525	16.985	0.005	-134.3	
33.35		115.165	0.90509	16.936	0.006	-126.4	
32.20		115.187	0.90492	16.887	0.007	-118.6	
31.05		115.209	0.90476	16.839	0.008	-110.8	
29.90		115.231	0.90460	16.791	0.010	-103.0	
28.75		115.252	0.90444	16.744	0.012	-95.3	
27.60		115.274	0.90428	16.698	0.014	-87.5	
26.45		115.296	0.90412	16.652	0.017	-79.9	
25.30		115.317	0.90395	16.606	0.021	-72.2	
24.15		115.339	0.90379	16.562	0.025	-64.5	
23.00		115.360	0.90363	16.518	0.030	-56.8	
21.85		115.382	0.90347	16.474	0.036	-49.0	
20.70		115.403	0.90331	16.431	0.043	-41.2	
19.55		115.424	0.90315	16.388	0.052	-33.2	
18.40		115.445	0.90300	16.347	0.063	-25.2	
17.25		115.466	0.90284	16.305	0.077	-17.0	
16.10		115.487	0.90268	16.265	0.091	-8.7	
14.95		115.508	0.90253	16.225	0.110	0.0	
13.80		115.528	0.90237	16.186	0.133	9.0	
12.65		115.549	0.90222	16.147	0.150	17.3	
11.50		115.569	0.90207	16.109	0.167	25.3	
10.35		115.589	0.90191	16.071	0.187	33.8	
9.20		115.609	0.90176	16.034	0.211	42.7	
8.05		115.629	0.90161	15.998	0.237	51.6	
6.90		115.649	0.90146	15.962	0.266	60.8	
5.75		115.668	0.90132	15.927	0.299	70.3	
4.60		115.687	0.90117	15.893	0.334	80.0	
3.45		115.707	0.90103	15.859	0.372	89.9	
2.30		115.725	0.90089	15.826	0.416	100.4	
1.15		115.744	0.90075	15.793	0.470	111.8	
0.09		115.760	0.90062	15.764	0.523	122.6	

### 3.5.2 Retrieval Vectors

#### 3.5.2.1 Introduction

In TWPR, an atmospheric profile of a chemical species or temperature is defined on the forward model (FM) grid as a function of log pressure. This grid is chosen so that each layer within the grid is homogeneous with respect to temperature, humidity and the trace gases. The retrieval of these profiles, however, is generally not calculated directly on the FM grid. Rather, the profile is represented by some basis in order to constrain the estimated profile. A priori information can be used to further constrain the shape to be physically reasonable. The coefficients of the profile in this basis are retrieved and then “mapped” to the forward model grid. The linear algebraic ordering of these coefficients is called the retrieval vector.

The retrieval vector may be selected from the following, although not all combinations will be valid.

- surface emitting temperature, for each detector
- surface spectral emissivity for a specified spectral range, for each detector
- atmospheric temperature
- constituent mixing ratio ( $q$ )
- constituent  $\ln(q)$
- aerosol extinction coefficient (or its  $\ln$ ) on a contiguous range of levels of the retrieval grid and for a specified spectral range
- the angle of the boresight of the spectrometer

The quantities not being retrieved at each stage will be treated as forward model parameters.

The choice of basis depends on the specific trace gas. For an initial guess refinement stage of the retrieval the basis is chosen to capture patterns of the profile that are more easily detected, e.g., the shape retrieval [Clough et al 2002, Bowman et al 2002]. Retrievals of trace gases subsequent to an initial guess refinement retrieval may use a piece-wise linear basis in mixing ratio or the logarithm of mixing ratio. In either case, the basis must also be applied to the Jacobians as well. The mathematical machinery necessary to relate the retrieval vector and its Jacobian to the full state vector and its Jacobian are described in the following section.

#### 3.5.2.2 Mapping

The atmospheric profile is described by the atmospheric full state vector  $\mathbf{x} \in \mathbb{R}^M$ , the FM radiances by  $\mathbf{L} \in \mathbb{R}^N$ , and the Jacobian by  $\mathbf{K}_x \in \mathbb{R}^{N \times M}$ . The retrieval vector,  $\mathbf{z} \in \mathbb{R}^{M'}$ , is related to the full state vector by a mapping  $\mathbf{M} : \mathbb{R}^{M'} \rightarrow \mathbb{R}^M$  so that  $\mathbf{x} = \mathbf{M}(\mathbf{z})$ . In general,  $M' < M$ . For simplicity, we shall restrict our attention initially to linear maps so that

$$\mathbf{x} = \mathbf{M}\mathbf{z}. \tag{3.41}$$

Equation (3.41) may also be written as

$$\mathbf{x} = \sum_{i=1}^{M'} z_i \mathbf{m}_i \quad (3.42)$$

where  $z_i = [\mathbf{z}]_i$  is the  $i^{\text{th}}$  element of the retrieval vector and  $\mathbf{m}_i$  is the  $i^{\text{th}}$  column vector of  $\mathbf{M}$ . The atmospheric state vector is expressed as a linear combination of basis vectors  $\mathbf{m}_i$  weighted by retrieval parameters  $z_i$ .

We also need an inverse mapping from a full state vector to a retrieval vector, which is described by

$$\mathbf{z}_0 = \mathbf{M}^* \mathbf{x}. \quad (3.43)$$

Under certain conditions the inverse mapping is a pseudo-inverse of the map. These conditions will be described in more detail later.

The Jacobian of the retrieval parameters with respect to the radiances is expressed as

$$\mathbf{K}_z = \frac{\partial \mathbf{L}(\mathbf{M}\mathbf{z})}{\partial \mathbf{z}} \quad (3.44)$$

The chain rule can be applied to Equation (3.44) to give

$$\frac{\partial \mathbf{L}}{\partial \mathbf{z}} = \frac{\partial \mathbf{L}}{\partial \mathbf{x}} \frac{\partial \mathbf{x}}{\partial \mathbf{z}} \quad (3.45)$$

or

$$\mathbf{K}_z = \mathbf{K}_x \mathbf{M}. \quad (3.46)$$

### 3.5.2.3 Initialization and Update of Retrievals with Maps

The retrieval algorithm estimates the retrieval parameters that best minimize the ML or MAP cost function. The Forward Model, however, works exclusively on the FM pressure grid and can only be evaluated on the atmospheric state vector,  $\mathbf{x}$ . Therefore a map projects the estimated retrieval parameters to atmospheric state values. This can be done either by projecting the natural log of the atmospheric state values or the values themselves. Typically natural logs are used, although for shape retrievals and atmospheric temperature profiles the values themselves are used. So, for the typical case, an additional exponentiation will be necessary.

To start the retrieval, the initial values of the retrieval parameters must be calculated from the initial atmospheric state vector. The initial retrieval vector is related to the atmospheric state vector through the inverse mapping as described in Equation (3.43), thus

$$\ln(\mathbf{z}_0) = \mathbf{M}^* \ln(\mathbf{x}_{in}). \quad (3.47)$$

The forward model and Jacobian must be calculated on the atmospheric full state vector. Thus the initial guess retrieval vector must be mapped back to an initial guess atmospheric full state vector resulting in

$$\mathbf{x}_0 = \mathbf{M}\mathbf{z}_0 = \mathbf{M}\mathbf{M}^* \mathbf{x}_{in}, \quad (3.48)$$

where  $\mathbf{x}_{in}$  is the input atmospheric full state vector. In general, the initial guess atmospheric full state vector is *not* equal to the input atmospheric full state vector, i.e.  $\mathbf{M}\mathbf{M}^* \neq \mathbf{I}$ .

The update to the retrieval parameters is calculated by solving Equations (3.48). The new atmospheric state vector is then

$$\ln(\mathbf{x}_{i+1}) = \mathbf{M} \ln(\mathbf{z}(1 + \delta\mathbf{z})). \quad (3.49)$$

The forward model may now be recalculated at the new atmospheric state vector,  $\mathbf{L}(\mathbf{x}_{i+1})$ .

#### 3.5.2.4 Nonlinear Maps based on natural log

For several atmospheric species, e.g. ozone, H<sub>2</sub>O, the retrieval of the natural log of the volume mixing ratio (VMR) is preferable. In this case,

$$\ln \mathbf{x} = \mathbf{M}\mathbf{z}, \quad (3.50)$$

which results in the following nonlinear maps:

$$\mathbf{M}(\mathbf{g}) = \exp(\mathbf{M}\mathbf{g}) \quad (3.51)$$

and

$$\mathbf{M}^*(\mathbf{g}) = \mathbf{M}^* \ln(\mathbf{g}). \quad (3.52)$$

The initial guess retrieval vector and the a priori retrieval vector are now calculated as

$$\mathbf{z}_0 = \mathbf{M}^* \ln(\mathbf{x}_{in}) \quad (3.53)$$

### 3.5.3 A Priori Constraints

*A priori* is a description of what is known or believed about the state before the measurement is considered. Typically it may comprise a climatological estimate of the state plus some measure of its uncertainty, most conveniently expressed as a covariance matrix. Other possible sources include independent measurements by other observing systems, such as the NCEP analyses or forecasts.

Other constraints that may be used include positivity, and linear inequality and *ad hoc* smoothness constraints. Positivity for constituents may be imposed by using log(mixing ratio)

rather than mixing ratio in the state vector. Linear inequality constraints allow physical bounds to be imposed on the range of the state vector elements, such as emissivity [Gill, Murray, and Wright, 1981]. Smoothness can be imposed by adding a quadratic form to the cost function that penalizes the first or second difference of the profile [Twomey 1963, Steck 2002] or by defining correlations between elements of the profile that decay exponentially as a function of distance [Steck, 2001].

The combination of constraints to be used will be determined by the driver table (see 3.5.1).

### 3.5.4 Inverse Algorithm

#### 3.5.4.1 The additive noise model and cost function

Measured radiances in TES can be related to a forward model through the following additive noise model:

$$\mathbf{y} = \mathbf{F}(\mathbf{x}) + \mathbf{n} \quad (3.54)$$

where  $\mathbf{y} \in \mathbb{R}^N$  which is a real vector of length  $N$ , is the calibrated, measured spectrum;  $\mathbf{x} \in \mathbb{R}^M$  is the “full” state vector and  $\mathbf{n}$  is a vector containing all the other trace gases, atmospheric temperature profile, geometry of the spacecraft, etc. necessary to define the radiative transfer from the atmosphere to the space craft. The forward model parameter vector  $\mathbf{b}$  will be dropped in the subsequent derivations because these parameters are fixed for the purpose of the retrievals. However, the effects of errors in the forward model parameter vector will be discussed in Section 3.5.8. The forward model operator  $\mathbf{F} : \mathbb{R}^M \rightarrow \mathbb{R}^N$  is a discretized version of Equation (3.5) that simulates a spectrum produced from the propagation of radiation through the atmosphere from the Earth to the spacecraft. The noise term  $\mathbf{n} \in \mathbb{R}^N$  is assumed to be zero-mean, Gaussian white noise so that the error covariance,  $\mathbf{S}_n = E[\mathbf{nn}^T]$ , is  $\mathbf{S}_n = \sigma^2 \mathbf{I}$  where  $E[\cdot]$  is the expectation operator [Papoulis:prvsp-84] and  $\sigma$  is the standard deviation of the noise.

Given the additive noise model of the measured radiances, the estimate of the full state vector,  $\mathbf{x}$ , is

$$\hat{\mathbf{x}} = \mathbf{M} \cdot \min_{\mathbf{z}} (C(\mathbf{z})), \quad (3.55)$$

where the cost function is

$$C(\mathbf{z}) = \|\mathbf{y} - \mathbf{F}(\mathbf{Mz})\|_{\mathbf{S}_n^{-1}}^2 + \|\mathbf{z} - \mathbf{z}_c\|_{\mathbf{\Lambda}}^2. \quad (3.56)$$

The mapping matrix,  $\mathbf{M}$ , is defined in Equation (3.41),  $\mathbf{z}_c$  is the constraint vector and  $\mathbf{\Lambda}$  is the constraint matrix. The constraint vector and matrix may be based on climatology or smoothness as discussed in Section 3.5.3.

Minimization proceeds iteratively from an initial guess by means of an appropriate numerical method, until convergence is obtained as discussed in Section 3.5.4.3.

### 3.5.4.2 Initial Guess Refinement

The purpose of initial guess refinement is to start the relatively expensive optimal estimator close to the final solution, so that as few iterations as possible are required. Thus a computationally inexpensive *ad hoc* non-optimal retrieval method is used to find the region of the solution. \

In the nadir case, a preliminary retrieval step could be to treat the troposphere and stratosphere as two columns. This step is to fit the measurement spectrum to solve for the two scale factors that would shift the initial guess constituent profile, and this refined profile would then be the initial guess profile used for the full optimal retrieval at more levels [S. Clough *et al*, 1995].

Alternatively, the so-called shape retrieval could be applied to either limb or nadir retrievals. This mapping is constructed to retrieve the broad features of the ozone profile such as the mean and gradient of ozone in the troposphere as well as the peak and width of the stratospheric ozone shape [Clough *et al*, 2002; Bowman *et al*, 2002]. The results of the shape retrieval are then used as the initial guess for a subsequent retrieval based on a finer discretization of the profile.

### 3.5.4.3 Numerical Solution

There is a wide range of numerical methods available in the literature designed for minimizing non-linear least-squares functions such as the cost function in Equation (3.55). The basic methods considered here are the Gauss-Newton method and the Levenberg-Marquardt method. Both methods implement Equation (3.54) by iteratively linearizing the cost function in Equation (3.55) with respect to the retrieval vector. We define a step in the retrieval vector as

$$\delta \mathbf{z} = \mathbf{z}_{i+1} - \mathbf{z}_i. \quad (3.57)$$

The Gauss-Newton method consists of iteratively minimizing the cost function linearized about  $\mathbf{z}_i$ , which can be written as

$$\mathbf{K}' \delta \mathbf{z} = \delta \mathbf{y}' \quad (3.58)$$

where

$$\mathbf{K}' = \begin{bmatrix} \mathbf{S}_n^{-1/2} \mathbf{K}_z(\mathbf{z}_i) \\ \mathbf{\Lambda}^{1/2} \end{bmatrix} \quad (3.59)$$

and

$$\delta \mathbf{y}' = \begin{bmatrix} \mathbf{S}_n^{-1/2} (\mathbf{y} - \mathbf{F}(\mathbf{Mz}_i)) \\ \mathbf{\Lambda}^{1/2} (\mathbf{z} - \mathbf{z}_c) \end{bmatrix}. \quad (3.60)$$

The Jacobian,  $\mathbf{K}_z$ , in Equation (3.59) is defined in Equation (3.44) and related to the full state vector  $\mathbf{x}$  in Equation (3.46). A numerically robust method for calculating a Gauss-Newton

iteration to Equation (3.58) is by factoring the augmented Jacobian  $\mathbf{K}'$  into the QR decomposition

$$\mathbf{QR}\delta\mathbf{z} = \delta\mathbf{y}', \quad (3.61)$$

where  $\mathbf{Q} \in \mathbb{R}^{N \times N}$  is an orthogonal matrix and  $\mathbf{R} \in \mathbb{R}^{N \times M}$  is an upper triangular matrix. The orthogonal matrix can be inverted implicitly and the retrieval vector can be calculated by back-solving from  $\mathbf{R}$  [Bjorck,1996]. The forward model is evaluated by the updated full state vector  $\mathbf{x}_{i+1} = \mathbf{M}\mathbf{z}_{i+1}$  and Equation (3.58) is solved again until convergence, which is the subject of Section 3.5.4.4.

Alternatively, the least squares solution to Equation (3.58) may also be written as

$$\delta\mathbf{z} = (\mathbf{K}'^T \mathbf{K}')^{-1} \mathbf{K}'^T \delta\mathbf{y}' \quad (3.62)$$

or

$$\mathbf{z}_{i+1} = \mathbf{z}_i + (\mathbf{\Lambda} + \mathbf{K}_i^T \mathbf{S}_n^{-1} \mathbf{K}_i)^{-1} (\mathbf{K}_i^T \mathbf{S}_n^{-1} [\mathbf{y} - \mathbf{F}(\mathbf{M}\mathbf{z}_i)] - \mathbf{\Lambda}[\mathbf{z}_i - \mathbf{z}_c]) \quad (3.63)$$

Note that the efficiency of the iteration is enhanced if  $\mathbf{S}_n$  is diagonal, particularly for cases where the measurement vector is large, as in the case of TES. However, the apodization of microwindows will introduce off-diagonal elements in  $\mathbf{S}_n$  and other sources such as calibration may also cause correlations in the measurement errors. The off-diagonal elements due to apodization are easily calculated and if any other correlations are stable with time, we could perform an inversion of the error correlation matrix on an infrequent basis. This stored matrix could then be scaled using the diagonal measurement errors to provide  $\mathbf{S}_n^{-1}$  for each retrieval. The retrieval sensitivity to the accuracy of the off-diagonal elements in  $\mathbf{S}_n$  needs to be studied in order to decide when off-diagonal elements can be neglected and how often the inverted correlation matrix would need to be updated to account for any time variations.

The Gauss-Newton method is satisfactory for *small residual problems* [Fletcher, 1993]. For these problems, the initial guess is in a region sufficiently close to the solution such that nonlinearities in the cost function are small, as we hope to have with the initial guess refinement. If the initial guess refinement is not successful, then the Levenberg-Marquardt (LM) method will be used. This algorithm is implemented as a *trust-region* method [More', 1977]. In this method, the cost function in (3.30) is minimized subject to a constraint on the maximum step size,  $\|\mathbf{z}_{i+1} - \mathbf{z}_i\| < \delta$ . The *trust region radius*  $\delta$  defines a sphere over which the cost function is considered linear. An LM step is calculated by solving

$$\begin{bmatrix} \mathbf{K}' \\ \gamma_i^{1/2} \mathbf{W} \end{bmatrix} \delta\mathbf{z} = \begin{pmatrix} \delta\mathbf{y}' \\ \mathbf{0} \end{pmatrix} \quad (3.64)$$

with the QR decomposition or alternatively as

$$\mathbf{z}_{i+1} = \mathbf{z}_i + (\gamma_i \mathbf{W}^T \mathbf{W} + \mathbf{\Lambda} + \mathbf{K}_i^T \mathbf{S}_n^{-1} \mathbf{K}_i)^{-1} (\mathbf{K}_i^T \mathbf{S}_n^{-1} [\mathbf{y} - \mathbf{F}(\mathbf{Mz}_i)] - \mathbf{\Lambda}[\mathbf{z}_i - \mathbf{z}_c]) \quad (3.65)$$

where the parameter  $\gamma_i$  is called the LM parameter and  $\mathbf{W}$  is a non-zero scaling matrix that permits the minimization over an ellipse rather than a sphere. The LM parameter is varied from step to step according to the strategy described by More':

1. Find  $\gamma_i$  such that the step size is within the trust region radius.
2. Check that  $C(\mathbf{z}_{i+1}) < C(\mathbf{z}_i)$ . If the update cost function has increased, then reduce the trust region radius and return to step 1.
3. Compare  $C(\mathbf{z}_{i+1})$  with its linear approximation,  $C_1(\mathbf{z}_{i+1})$ .
4. Increase the trust region radius if  $C(\mathbf{z}_{i+1}) \sim C_1(\mathbf{z}_{i+1})$  and decrease if  $C(\mathbf{z}_{i+1}) \gg C_1(\mathbf{z}_{i+1})$ .
5. Return to step 1 for next iteration.

#### 3.5.4.4 Convergence Criterion

The convergence criterion depends on the numerical method being used. If it is a second-order method such as Levenberg-Marquardt then once the  $\gamma$  parameter has become small, i.e., when the Levenberg-Marquardt step reduces to a Gauss-Newton step, a change  $C(\mathbf{z}_i) - C(\mathbf{z}_{i+1})$  that is positive and much less than unity is appropriate [Press *et al.*, 1989]. When convergence appears to have taken place according to this criterion the absolute value of  $C(\mathbf{z})$  will be examined to determine whether the iteration has converged to a valid solution. This is determined using a  $\chi^2$  test:

$$\chi^2 = \|\mathbf{y} - \mathbf{F}(\mathbf{Mz})\|_{\mathbf{S}_n^{-1}}^2 \quad (3.66)$$

This test determines whether the solution agrees with the measurements to the required accuracy. We may also test whether the solution agrees with the *a priori* using

$$\chi^2 = \|\mathbf{z} - \mathbf{z}_c\|_{\mathbf{\Lambda}}^2 \quad (3.67)$$

where the constraint vector and matrix are assumed to be the climatological mean and covariance, respectively. The statistics of the *a priori*, however, are likely to be less well known than those of the measurement error, so this may tell us more about the quality of the *a priori* rather than that of the retrieval.

### 3.5.5 Pixel Categorization for Nadir

Clouds and aerosols may impact TES measurements, and as discussed in section 3.3.3, there are a variety of radiative transfer approaches/approximations that may be used, depending on the presence and characteristics of the clouds or aerosols. Therefore, it is imperative that there be techniques for categorizing the target scenes so that appropriate radiative transfer solution strategies can be applied.

We will use the framework of sorting the data into cases of no clouds, broken or highly inhomogeneous clouds, optically thick clouds, and optically thin clouds. The basic strategy is to examine the brightness temperatures in the atmospheric window regions and use the values and variability of the values to classify the observations. These are methods similar to those proposed for MODIS [Ackerman, *et al.*, 1998]).

The brightness temperature in the 11 micron window will be the primary quantity examined for pixel categorization. This quantity (BT11) is an brightness temperature average over the 867-900  $\text{cm}^{-1}$  region with water lines removed. Data from this spectral region will be available in all of the observation strategies and it is comparable to long term nadir satellite measurements from instruments such as AVHRR and MODIS.

Additional L1B parameters that may be calculated are  $\text{CO}_2$  line depths. We are studying the possibility of calculating a parameter that can be a quick indication of the reduction in the column  $\text{CO}_2$  and therefore an indication that the measurement is not seeing to the surface.

Clear cases will be identified by instances where the BT11 value is within a threshold of the surface temperature and does not have high variability between pixels. Preliminary analysis shows that when absorption effects of the water continuum are taken into effect, a temperature threshold of about 0.5K can be used for high clouds. This threshold will result in a set of clear cases that includes all cases with 'high cloud' optical depths of less than 0.02. Analysis is underway to assess the impact of the definition of 'clear' on retrievals.

Cases of broken or highly inhomogeneous clouds will be identified by high variability in BT11 between pixels. The first approximation of this threshold will be made by examination of global datasets from MODIS. The 1km by 1km 11 micron radiances from MODIS will be converted to brightness temperature, and variability over 5km by 8km areas will be calculated. This variability data will be compared to MODIS cloud mask data over the same footprints to determine the variability threshold. This threshold will be updated after TES data is collected.

Cases of optically thick clouds will be identified by BT11 values that are significantly lower than surface temperatures and do not have high variability. Additional work is underway to develop techniques for differentiating between optically thick low clouds and moderate optical thickness high clouds that would result in the same BT11 temperatures.

Cases of optically thin clouds will be identified by BT11 values slightly lower than surface temperatures. Again, methods of implementing an adaptation of  $\text{CO}_2$  slicing to determine cloud height are under investigation.

Another possibility, to be considered for special processing, is to perform the retrieval in the presence of clouds using the philosophy of the  $\text{CO}_2$  slicing technique, in conjunction with the NWP temperature field, to determine the effective cloud amount and the cloud-top pressure. The cloud could then be included in the forward model with retrievable optical parameters. The basic  $\text{CO}_2$  slicing method is described in many papers (see the description and references in Wylie, *et al.*, 1994) and involves the assumption of a single cloud layer. The cloud-top pressure is determined using the measured radiance and the estimated clear sky radiance for (at least 2)

channels with CO<sub>2</sub> lines where the weighting functions peak at different altitudes. This type of algorithm can be tested with many existing data sets such as AES, IRIS-D, IMG and NAST-I. For TES data, in many cases, we should be able to compare the estimated cloud top pressures with CHEM OMI data products.

### 3.5.6 Pixel Categorization in the Limb

Clear pixel detection in the limb view is much more straightforward than in the nadir because the background is cold space rather than a warm surface. It can be accomplished simply by setting a radiance threshold in a window region such as 12  $\mu\text{m}$ . Calculations made for ISAMS [Lambert *et al.*, 1996] show limb radiance at 12  $\mu\text{m}$  in the region of 10-20 km as around 0.5  $\text{mW}/\text{m}^2/\text{sr}/\text{cm}^{-1}$  in the absence of aerosol, compared with the Planck function at 200K of around 20  $\text{mW}/\text{m}^2/\text{sr}/\text{cm}^{-1}$ . Mt. Pinatubo volcanic aerosol was shown to be optically thick in this region, so that we would expect cirrus cloud also to be optically thick.

A more sophisticated cloud detector would be the joint retrieval of temperature and aerosol extinction profiles using an onion peeling process. The lower limit of the limb retrieval would then be set as the lowest altitude where the aerosol extinction is less than some threshold.

### 3.5.7 Retrieval Microwindow Selection

There are several reasons for using small regions of the spectrum (microwindows) for retrievals, including:

- Reduction in computation, because the forward model only has to generate a small interval.
- Reduction in computation due to fewer fitted parameters
- Reduction of the effect of interfering gases

The spectral size of the microwindows will range from a few wavenumbers to one hundred or more wavenumbers, depending upon the species to be retrieved. In order to achieve the maximum reduction in computing time, both the calculated and observed spectrum need to be apodized. This reduces the ringing of lines, and thus the width of the spectrum required.

Usually, different microwindows will be needed for different altitude regions, and for the nadir and limb. Generally, strong lines will be used for high altitudes, while weak lines will give more information at low altitudes.

There are at least two objective methods for microwindow selection [Rodgers 1996, von Clarmann 1999]. Candidate regions are selected for a species based on known absorption and interferences. The information content for particular points in the interval are evaluated, and selections made to maximize the information. Initial microwindows will be selected using simulated spectra, with expected instrument noise. The microwindows will be revised early in the mission based on real instrument performance.

### 3.5.8 Error Analysis

The retrieved state  $\mathbf{x}_r$  can be related to the true state  $\mathbf{x}$  by

$$\mathbf{x}_r = \mathbf{x}_a + \mathbf{A}(\mathbf{x} - \mathbf{x}_a) + \mathbf{e}_x \quad (3.68)$$

where  $\mathbf{A} = \partial \mathbf{x}_r / \partial \mathbf{x}$  is the averaging kernel, and  $\mathbf{e}_x$  is the contribution to the total error from random and systematic errors in the measurement and the forward model.

The error term  $\mathbf{e}_x$  can be described by a covariance matrix  $\mathbf{S}_e$ , which can be expressed as the sum of random and systematic components:

$$\mathbf{S}_e = \mathbf{S}_r + \mathbf{S}_s \quad (3.69)$$

The averaging kernel matrix and the error covariances may be calculated at little cost during the retrieval process. However they are of size  $n^2$ , when  $\mathbf{x}$  is of size  $n$ , and every retrieval has its own unique averaging kernel and error covariance. There may be problems of (a) storage and (b) user appreciation.

The following parameters will be computed for error characterization:

- (1) the error variance of each retrieved quantity, separated into random and systematic components.
- (2) for profile quantities, the ‘correlation distance’, or vertical range outside which the absolute value of correlation coefficient is less than some TBD quantity (nominally 0.5)
- (3) the correlation matrix for the retrieval vector
- (4) the fraction of explained variance

The averaging kernel matrix should be made available in some form, but it is TBD whether we present (1) the full matrix for every retrieval or (2) a few sample matrices

The fraction of explained variance can be described as

$$f_i = 1 - [\mathbf{K}^T \mathbf{S}_e^{-1} \mathbf{K} + \mathbf{S}_a^{-1}]_{ii}^{-1} \mathbf{S}_{a,ii} \quad (3.70)$$

which has the property that  $f_i$  takes the value 1 when all of the information comes from the data and none from the *a priori* and 0 when no information comes from the data.

Finally, the user should know the range of grid levels over which the retrieval comes primarily from the data, rather from the *a priori*. This is most properly expressed in terms of the area of the averaging kernel, a vector of length  $n$ . It can be simplified to two numbers - the upper and lower levels of the range within which the *a priori* contribution is less than some given fraction.

### 3.6 FINAL FULL SPECTRUM CALCULATION

In order to search for unmodeled species in our data, we will examine the difference between the complete forward model generated from our retrieved atmospheric state and the full TES measured spectrum. The final forward model is calculated using the full state vector constructed from the microwindow retrievals. Unmodeled species will appear as deviations in the residual that are above the noise level and have characteristic spectral features that can be analyzed using techniques such as Fourier analysis, wavelet transforms or spectral matched filtering.

For land nadir views, in order to calculate a residual spectrum, we will also need to retrieve surface spectral emissivity parameters since these cannot be completely provided from the microwindow retrievals. This requires saving the transmission and downwelling radiance from the atmospheric radiative transfer calculation but the Jacobians of the atmospheric parameters would not need to be calculated or stored.

For limb views this full spectrum calculation could become prohibitive if performed for each target. We may therefore only perform it as needed for diagnostics (e.g., TBD per Global Survey). For detection of unmodeled species, the residual calculation could be performed more often but on reduced spectral ranges that are larger than microwindows but smaller than the full filter frequency ranges.

### 3.7 DATA QUALITY & RESIDUALS

Data quality is assessed at every level of processing (1A, 1B, 2, 3 ....) and the assessments passed forward to all subsequent steps (unless the error halts the Product Generation Executive [PGE]). For completeness, therefore, this section contains all error conditions from all levels, stated in the form of requirements. A full discussion can be found in JPL D-20322: *Science & Operational Algorithm Quality Assessment and Diagnostic Requirements*, V1.2, June 29, 2001.

Note, however, that this section covers only the science requirements. “Software Mechanics” (e.g., exception handling) are treated elsewhere.

#### 3.7.1 Level 1A

- 1: Data streams with missing packets shall be placed in a holding area and, if the missing packets do not appear within TBD (24) hours, the associated interferograms shall be rejected.
- 2: Interferograms whose total length is less than expected by TBD (1%) shall be rejected..
- 3: All interferograms containing absolute DN values in excess of TBD (30,000) shall be flagged as having “possible A-D overflow”.
- 4: All interferograms containing date or time errors shall be flagged as having “possible date/time error”.
- 5: The Run Counter is a unique identifier (beginning at 1) for major data blocks such as a 16-orbit Global Survey. It is continuously incremented for the lifetime of the mission.

All interferograms with an erroneous Run Count shall be flagged as having a “run count error” and the PGE halted.

6: The Sequence Counter identifies data granules such as an 81.2 second Global Survey sequence. It is reset at the beginning of each Run.

All interferograms with an erroneous Sequence Count shall be flagged as having a “sequence count error” and the PGE halted.

7: The Scan Counter identifies the individual scans within a sequence (#7 for a Global Survey sequence) and is reset at the start of each Sequence.

All interferograms with an erroneous Scan Count shall be flagged as having a “scan count error” and processing halted.

8: All interferograms with erroneous filter wheel settings shall be rejected.

9: All interferograms, except for “cold space” calibrations, with maximum absolute DN values less than 16,000 shall be flagged as having “A-D underflow”.

10: All interferograms for which persistent indications of either attitude or attitude rate errors are found shall be rejected.

11: All interferograms for which the PCS pitch & roll angles exceed acceptable bounds shall be rejected.

12: All interferograms for which the mean scan speed is outside  $1.0559 \pm 0.317$  cm/sec shall be flagged as having an “incorrect scan speed”.

13: All interferograms for which the scan direction is not that expected shall be flagged as having an “incorrect scan direction”.

14: All interferograms for which the scan speed variations exceed TBD (3%) shall be flagged as having an “excess scan speed variation”.

15: All interferograms for which the scan speed variations exceed TBD (4%) shall be rejected.

16: All blackbody calibration interferograms for which the indicated blackbody temperatures are not as expected shall be rejected.

17: All interferograms for which the cold reference plate temperature differs from TBD (180K) by more than TBD (2K) shall be rejected.

18: All interferograms acquired while any instrument temperature has an incorrect or unexpected value but within the “yellow” range shall be flagged as having a “possible instrument

temperature out of range”.

19: All interferograms acquired while any instrument temperature has an incorrect or unexpected value outside the “yellow” range shall be rejected.

### **3.7.2 Level 1B**

1: All interferograms containing amplitudes more than TBD (10) times greater than neighboring values (except near Zero Path Difference) shall be flagged as having “possible spikes in interferogram”.

2: Spectra having offsets in excess of TBD ( $1\Phi$ ) shall be flagged as having “significant baseline offset in spectrum”.

3: If the area under the spectrum does not meet expectations within TBD (5%) then the spectrum shall be flagged as having an “incorrect gain or instrument is contaminated”.

4: If the peak brightness temperature does not meet expectations the spectrum shall be flagged as “probable cloud or aerosol in the field of view”.

5: If the nadir pixel-to-pixel brightness temperature variations exceed TBD (1K) then the PGE shall be halted and the data flagged as having “excess inter-pixel variability”.

6: If correlation tests on the imaginary part of the spectrum following phase correction show unexplained peaks in excess of TBD ( $5\Phi$ ) the spectrum shall be rejected.

7: Spectra having NESRs more than TBD (5%) above expectations shall be flagged as having “excess noise or reduced signal”.

### **3.7.3 Level 2**

1: Retrievals that do not converge in TBD (3) iterations shall be stopped and rejected.

2: If the final retrieval step size is greater than TBD (0.1%) of the parameter value the retrieval shall be flagged as having “probable convergence failure” and the parameter name logged.

3: Retrievals that converge with a significance level greater than TBD (99%) shall be flagged as having a “significant disagreement with the measurement”, and the parameter name logged.

4: If a full climatology is available for a particular species then retrievals with a significance level greater than TBD (99%), shall be flagged as having a “significant disagreement with the climatology”.

5: Retrievals that go negative or show unsatisfactory smoothness (“jack-knifing”) in which consecutive values in a profile oscillate about a mean by more than TBD ( $3\Phi$ ) shall be flagged as having “negative or jack-knifed profile”.

6: Retrievals wherein the trace of the Averaging Kernel matrix is less than TBD (1) shall be flagged as having “little information content”.

7: Retrievals exhibiting peak residuals (spectrum - final forward model) greater than TBD ( $5\Phi$ ) above the RMS noise level shall be flagged as having “excess error propagation or unmodeled species”.

8: Residuals having a mean offset greater than TBD ( $1\Phi$ ) shall be flagged as having “significant offset in the mean residual”.

### **3.7.4 Level 3**

9: Associated limb and nadir retrievals that differ by more than TBD (2x the sum of the error bars) shall be flagged as having “inconsistent limb & nadir profiles” and the parameter name logged.

### **3.7.5 Archiving**

Observations that complete all stages with acceptable flags will be released to the archive. The data will be accompanied by the diagnostics described in Section 2.4

## 4 ALGORITHM VERIFICATION

### 4.1 END-TO-END CLOSURE EXPERIMENTS

The purpose of the end-to-end closure experiments using the TES reference and operational software is to test the robustness of TES level 2 retrieval algorithms and the operational software and to identify any problems either in the algorithm or in coding. This procedure will also be helpful for algorithm validations. A single step end-to-end simulation would be to add noise to the model radiance and then to execute a step retrieval defined in the TES retrieval strategies. A full end-to-end closure experiment would be to generate a full four-day global survey set of radiances with added noise and clouds and then to carry out the four-day retrieval processing.

Establishing a profile/parameter database which consists collections of measured atmospheric temperature and constituent profiles and surface parameter data by all means of observations, sonde, balloon, aircraft, satellite, etc. is one of the key activities for the pre-launch closure experiments. These profiles/parameters along with model simulated profiles allow us to compile the baseline initial guesses and the *a priori* (see sections 3.5.3 and 3.5.4), to simulate the observed spectral radiance, and to evaluate the retrieval results for all the possible atmospheric conditions including extreme cases. Global cloud coverage data will also be obtained so that the simulated TES global pixel measurements will be more realistic.

The end-to-end closure experiments will follow three procedures: (1) simulate the TES observations using collected measurement profiles/surface parameters/cloud coverage as the true atmospheric full state with added noise, (2) generate TES retrieval products using a defined initial guess, and (3) examine and evaluate the retrieval results and error analysis by comparing with the “smoothed true profiles” and their statistical variance. Since the level 2 software will be developed in steps from a single profile retrieval to automated four-day data retrieval, the end-to-end experiment can be performed at each step.

### 4.2 VALIDATION

Validation, in the sense used here, differs from validation of the TES measurements in that we will use pre-existing data that have already been analyzed by others. The objective is to ensure that the TES algorithm either produces identical results or there are plausible reasons why it does not. Measurement validation will employ near-concurrent and co-located measurements and is not further discussed in this document (although, of course, it is a crucial part of the overall TES experiment).

Data sources currently identified that are (or will be) appropriate for this purpose are

- 1) Airborne Emission Spectrometer (AES). AES operates in both a downlooking mode from a variety of aircraft and uplooking from the surface. It was specifically designed to cover the same spectral region at the same resolution as TES and is therefore a prime data source for validation exercises. Downlooking data are very similar to the TES nadir mode and uplooking data are a useful surrogate for TES limb data.

2) AERI (Atmospheric Emitted Radiation Interferometer). AERI is a well calibrated,  $1 \text{ cm}^{-1}$  spectral resolution, uplooking, Michelson interferometer covering the range 550 to 1700 and 2000 to  $2500 \text{ cm}^{-1}$ . Several copies of the instrument are operational – the one of primary interest for TES validation is located at the Central facility of the ARM Cloud And Radiation Test (CART) site in northern Oklahoma. The AERI-X (eXtended resolution AERI) is also located at the central facility. It has  $0.1 \text{ cm}^{-1}$  spectral resolution, but only covers 550 to  $1600 \text{ cm}^{-1}$ . The ARM program provides good temperature and water vapor information about the atmosphere overhead. Information about ozone and other stratospheric gases, as well as aerosol optical depth, is available from solar absorption instruments at the site.

3) HIS (High resolution Interferometric Sounder). HIS is an autonomous FTS that flies on the ER2 in a variety of campaigns with the goal of temperature and water vapor sounding. Some of the more recent campaigns have been in support of tropospheric chemistry missions, where independent measurements may also be available. Although the spectral resolution is lower, the data are from an altitude that is more “space-like” than the AES data.

4) IMG (Interferometric Monitor of Greenhouse Gases). IMG, a nadir sounder developed by the Japanese, flew on the ADEOS mission (which failed in June 1997). Nevertheless, it represents the only available source of real space-based data with spectral coverage and resolution very close to that of TES. Some tests using IMG data are already ongoing and more are planned.

5) MIPAS (Michelson Interferometer for Passive Atmospheric Sounding). MIPAS will fly on the ENVISAT mission at least one year before TES. It is a limb sounder with slightly poorer spectral resolution than TES but will nevertheless be the only available source of space-based limb emission data prior to TES, so it will be a very valuable validation tool.

6) NAST-I (NPOESS Aircraft Sounder Testbed – Interferometer). NAST-I is a nadir-viewing instrument that has flown on several ER2 missions, including CAMEX-3, with correlative radiosonde measurements. It has a spectral resolution of  $0.25 \text{ cm}^{-1}$  covering the spectral regime  $590\text{-}2810 \text{ cm}^{-1}$ . As a testbed to the NPOESS candidate instruments, it has been used to simulate “space-like” ground coverage views for the validation of key meteorological species.

## 5 REFERENCES

### 1 INTRODUCTION

*Execution Phase Project Plan for the Earth Observing System (EOS)*. GSFC 170-01-01, Rev. A, May 1995.

*Mission to Planet Earth Strategic Enterprise Plan 1996-2002*. NASA HQ MTPE, May 1996.

*Tropospheric Emission Spectrometer: Scientific Objectives & Approach, Goals & Requirements*. JPL D-11294, Rev. 5.0, May 1996.

### 2 BACKGROUND

Rothman, L.S., C.P. Rinsland, A. Goldman, S.T. Massie, D.P. Edwards, J.-M. Flaud, A. Perrin, C. Camy-Peyret, V. Dana, J.-Y. Mandin, J. Schroeder, A. McCann, R.R. Gamache, R.B. Wattson, K. Yoshino, K.V. Chance, K.W. Jucks, L.R. Brown, V. Nemtchinov, and P. Varanasi, The HITRAN Molecular Spectroscopic Database and HAWKS (HITRAN Atmospheric Workstation): 1996 Edition, *J. Quant. Spectrosc. Radiat. Transfer*, 60, 665-710, 1998.

TES Level 1B ATBD, JPL D-16479, October 1, 1999.

### 3 ALGORITHM DESCRIPTION

#### 3.1 ALGORITHM OVERVIEW

*TES Level 1B Algorithm Theoretical Basis Document*, JPL D-16479, 1999.

##### 3.2.4.1 Spectral grid for radiative transfer

Clough, S.A. and F.X. Kneizys, Convolution algorithm for the lorentz function. *Applied Optics*, 18, 2329, 1979.

##### 3.3.1.4 Atmospheric Radiance

Clough, S.A., M.J. Iacono, and J.-L. Moncet, Line-by-line calculation of atmospheric fluxes and cooling rates: Application to water vapor. *J. Geophys. Res.*, 97, 15761-15785, 1992.

##### 3.3.1.6 Solar Radiance

Rinsland, C.P., G.K. Yie, M.R. Gunson, R. Zander, and M.C. Abrams, Mid-infrared extinction by sulfate aerosols from the Mt. Pinatubo eruption, *J. Quant. Spectrosc. Radiat. Transfer*, 52, 241-252, 1994.

##### 3.3.1.7 Surface Contribution

Chandrasekhar, S., *Radiative Transfer*, Dover Publications, 1960.

Goody, R.M and Y.L. Yung, *Atmospheric Radiation, Theoretical Basis*, Second Edition, Oxford University Press, 1989.

### 3.3.2.1 Surface Radiative Properties

Smith, W. L., R. O. Knuteson, H. E. Revercomb, W. Feltz, H.B. Howell, W.P. Menzel, N. Nalli, O. Brown, J. Brown, P. Minnett, and W. McKeown, Observations of the Infrared Radiative Properties of the Ocean - Implications for the Measurement of Sea Surface Temperature via Satellite Remote Sensing, *Bull. Amer. Meteor. Soc.*, January 1996.

Masuda, K.T., Takashima and Y. Takayama: Emissivity of pure and sea waters for the model sea surface in the infrared window regions, *Remote Sens. Environ.*, 24, 313-329, 1988.

### 3.3.3 Radiative Transfer for Aerosols

G. Echle, T. von Clarmann, H. Oelhaf, 1998, Optical and microphysical parameters of the Mt. Pinatubo aerosol as determined from MIPAS-B mid-IR limb emission spectra, *J. Geophys. Res.*, D15, 19193-19211.

Moncet, J.-L. and S.A. Clough (1997): Accelerated monochromatic radiative transfer for scattering atmospheres: Application of a new model to spectral radiance observations. *J. Geophys. Res.*, 102, 21,853-21,866.

### 3.3.4 Solar Source Function

Gunson, M.R., M.M. Abbas, M.C. Abrams, M. Allan, L.R. Brown, T.L. Brown, A.Y. Chang, A. Goldman, F.W. Irion, L.L. Lowes, E. Mahieu, G.L. Manney, H.A. Michelsen, M.J. Newchurch, C.P. Rinsland, R.J. Salawitch, G.P. Stiller, G.C. Toon, Y.L. Yung, and R. Zander, The Atmospheric Trace Molecule Spectroscopy (ATMOS) experiment: Deployment on the ATLAS Space Shuttle missions, *Geophys. Res. Lett.*, 23, 2333-2336, 1996.

Kurucz, R.L., The solar spectrum: Atlases and line identifications, in *Laboratory and Astronomical High Resolution Spectra*, 81, edited by A.J. Sauval, R. Blomme, and N. Grevesse, Astron. Soc. of the Pacific Coast, 17-31, 1995.

Kurucz, R.L., Synthetic infrared spectra, in *Infrared Solar Physics*, IAU Symp. 154, edited by D.M. Rabin and J.T. Jefferies, Kluwer Acad., Norwell, MA, 1992a.

Kurucz, R.L., Atomic and molecular data for opacity calculations, *Revista Mexicana de Astronomia y Astrofisica*, 23, 45-48, 1992b.

Kurucz, R.L., Finding the missing solar ultraviolet opacity, *Revista Mexicana de Astronomia y Astrofisica*, 23, 181-186, 1992c.

Kurucz, R.L., Remaining line opacity problems for the solar spectrum, *Revista Mexicana de Astronomia y Astrofisica*, 23, 187-194, 1992d.

Kurucz, R.L., I. Furenlid, J. Brault, and L. Testerman, *Solar Flux Atlas from 296 to 1300 nm*, 240 pp., National Solar Observatory, Sunspot, New Mexico, 1984.

### 3.3.5 Instrumental Line shape Spectral Convolution and Apodization

Gallery, W. O, and S. A. Clough, FFTSCAN: A program for spectral smoothing using Fourier transforms. PL-TR-92-2131, Phillips Laboratory, Hanscom AFB, MA 01731-3010.

Bowman, K. W, H. M. Worden, and R. Beer, Instrument line-shape modeling and correction for off-axis detectors in Fourier-transform spectrometry, *Applied Optics*, 39, 3765-3773, 2000.

#### 3.3.7.1 ABSCO Table Generation

Anderson, G.P., S.A. Clough, F.X. Kneizys, J.H. Chetwynd, and E.P. Shettle, *AFGL atmospheric constituent profiles (0-120 km)*. AFGL-TR-86-0110, 1986.

National Aeronautics and Space Administration, (1976). *U.S. Standard Atmosphere Supplements*, U.S. Government Printing Office, Washington, D.C., 1976.

#### 3.3.7.2 TES Line-by-Line Code

Armstrong, B. H., Spectrum line profiles: The Voigt Function, *J. Quant. Spect. Rad. Trans.*, 7, 61-88, 1967.

Clough, S.A. and M.J. Iacono (1995): Line-by-Line Calculations of Atmospheric Fluxes and Cooling Rates II: Application to Carbon Dioxide, Ozone, Methane, Nitrous Oxide, and the Halocarbons. *J. Geophys. Res.*, 100, 16,519-16,535.

Clough, S.A., M.J. Iacono, and J.-L. Moncet, Line-by-line calculation of atmospheric fluxes and cooling rates: Application to water vapor. *J. Geophys. Res.*, 97, 15761-15785, 1992.

Hoke, M. L., S. A. Clough, W. Lafferty, and B. Olson, Line coupling in oxygen and carbon dioxide, in *IRS '88: Current Problems in Atmospheric Radiation*, edited by J. Lenoble and J. F. Geleyn, pp. 368-370, A. Deepak Publishing, Hampton, VA, 1989.

Mlawer, E.J., S.J. Taubman, P.D. Brown, M.J. Iacono and S.A. Clough, Radiative Transfer for Inhomogeneous Atmospheres: RRTM, a Validated correlated-k model for the longwave. *J. Geophys. Res.*, 102, 16,663-16,682, 1997.

Rothman, L. S., R. R. Gamache, R. Tipping, C. P. Rinsland, M. A. H. Smith, D. C. Benner, V. Malathy Devi, J.-M. Flaud, C. Camy-Peyret, A. Goldman, S. T. Massie, L. R. Brown, and R. A. Toth, HITRAN molecular database: Edition of 1991 and 1992, *J. Quant. Spectrosc. Radiat. Transfer*, 48, 469-507, 1992.

Strow, L.L., D. C. Tobin, and S. Hannon, A compilation of first-order line mixing coefficients for CO<sub>2</sub> Q-branches, *J. Quant. Spect. Rad. Trans.*, 52, 281-294, 1994.

Tjemkes, S.A., T. Patterson, R. Rizzi, M.W. Shephard, S.A. Clough, M. Matricardi, J. Haigh, M. Hopfner, S. Payan, A. Trotsenko, N. Scott, P. Rayer, J. Taylor, C. Clerbaux, L.L. Strow, S. DeSouza-Machado, D. Tobin, and R. Knuteson, The ISSWG Line-by-line Intercomparison Experiment, *Submitted to J. Quant. Spect. Rad. Trans.*, 2002.

Tobin, D. C., F. A. Best, P. D. Brown, S. A. Clough, R. G. Dedecker, R. G. Ellingson, R. K. Garcia<sup>1</sup>, H. B. Howell, R. O. Knuteson, E. J. Mlawer, H. E. Revercomb, J. F. Short, P. F. W van Delst, and V. P. Walden, Downwelling Spectral Radiance Observations at the SHEBA Ice Station: Water Vapor Continuum Measurements from 17-26 micrometer, *J. Geophys. Res.*, 1999, in press.

### 3.3.8 ABSCO Databases

National Aeronautics and Space Administration, (1976). *U.S. Standard Atmosphere Supplements*, U.S. Government Printing Office, Washington, D.C., 1976.

#### 3.3.8.1 Line Parameters

Brown, L. R., M. R. Gunson, R. A. Toth, F. W. Irion, C. P. Rinsland, and A. Goldman, The 1995 Atmospheric Trace Molecule Spectroscopy (ATMOS) Linelist. *Appl. Opt.*, 35, 2828-2848, 1996.

Rothman, L.S., C.P. Rinsland, A. Goldman, S.T. Massie, D.P. Edwards, J.-M. Flaud, A. Perrin, C. Camy-Peyret, V. Dana, J.-Y. Mandin, J. Schroeder, A. McCann, R.R. Gamache, R.B. Wattson, K. Yoshino, K.V. Chance, K.W. Jucks, L.R. Brown, V. Nemtchinov, and P. Varanasi, The HITRAN Molecular Spectroscopic Database and HAWKS (HITRAN Atmospheric Workstation): 1996 Edition, *J. Quant. Spectrosc. Radiat. Transfer*, 60, 665-710, 1998.

#### 3.3.8.2 Cross-Sections

Ballard, J., W.B. Johnston, M.R. Gunson, and P.T. Wassel, Absolute absorption coefficients of ClONO<sub>2</sub> infrared bands at stratospheric temperatures, *J. Geophys. Res.* 93, 1659-1665, 1988.

Camy-Peyret, C., J.-M. Flaud, L. Lechuga-Fossat, C. Laverdet and G. Le Bras, The Absorption of Gaseous Dinitrogen Pentoxide in the 8.1 and 5.7  $\mu\text{m}$  Spectral Regions, *Chem. Phys. Lett.* 139, 345-349, 1987.

Clerbaux, C., R. Colin, P.C. Simon and C. Granier, Infrared Cross Sections and Global Warming Potentials of 10 Alternative Hydrohalocarbons, *J. Geophys. Res.* 98, 10491-10497, 1993.

Cantrell, C.A., J.A. Davidson, A.H. McDaniel, R.E. Shetter, and J.G. Calvert, *Chem. Phys. Lett.* 148, 358-363, 1988; Erratum *Chem. Phys. Lett.* 152, 274, 1988.

Jacquinet-Husson, N., E. Ariè, J. Ballard, A. Barbe, L.R. Brown, B. Bonnet, C. Camy-Peyret, J.P. Champion, A. ChÈdin, A. Chursin, C. Clerbaux, G. Duxbury, J.M. Flaud, N. FourriÈ, A. Fayt, G. Graner, R. Gamache, A. Goldman, V.I. Golovko, G. Guelachvilli, J.M. Hartmann, J.C. Hillico, G. LefÈvre, O.V. Naumenko, V. Nemtchinov, D.A. Newnham, A. Nikitin, J. Orphal, A. Perrin, D.C. Reuter, L. Rosenmann, L.S. Rothman, N.A. Scott, J. Selby, L.N. Sinitisa, J.M. Sirota, A.M. Smith, K.M. Smith, V.I.G. Tyuterev, R.H. Tipping, S. Urban, P. Varanasi, M. Weber, The 1997 Spectroscopic GEISA Databank, *J. Quant. Spectrosc. Radiat. Transfer*, in press, 1998.

- Li, Z., and P. Varanasi, Measurement of the Absorption Cross-Sections of CFC-11 at Conditions Representing Various Model Atmospheres, *J. Quant. Spectrosc. Radiat. Transfer*, 52, 137-144, 1994.
- Massie, S.T., A. Goldman, D.G. Murcray and J.C. Gille, Approximate absorption cross sections of F12, F11, ClONO<sub>2</sub>, HNO<sub>3</sub>, CCl<sub>4</sub>, CF<sub>4</sub>, F21, F113, F114, and HNO<sub>3</sub>, *Appl. Opt.*, 24, 3426-3427, 1985.
- Massie, S.T., A. Goldman, A.H. McDaniel, C.A. Cantrell, J.A. Davidson, R.E. Shetter, and J.G. Calvert, Temperature Dependent Infrared Cross Sections for CFC-11, CFC-12, CFC-13, CFC-14, CFC-22, CFC-113, CFC-114, and CFC-115, *NCAR Technical Note/TN-358+STR*, 1991.
- Massie, S.T., and A. Goldman, Absorption Parameters of very Dense Molecular Spectra for the HITRAN Compilation, *J. Quant. Spectrosc. Radiat. Transfer*, 48, 713-719, 1992.
- McDaniel, A.H., C.A. Cantrell, J.A. Davidson, R.E. Shetter, and J.G. Calvert, The Temperature Dependent, Infrared Absorption Cross-Sections for the Chlorofluorocarbons: CFC-11, CFC-12, CFC-13, CFC-14, CFC-22, CFC-113, CFC-114, and CFC-115, *J. Atmos. Chem.*, 12, 211-227, 1991.
- Orlando, J.J., G.S. Tyndall, A. Huang, and J.G. Calvert, Temperature Dependence of the Infrared Absorption Cross Sections of the Carbon Tetrachloride, *Geophys. Res. Lett.*, 19, 1005-1008, 1992.
- Orphal, J., M. Morillon-Chapey, and G. Guelachvili, High-Resolution Absorption Cross Sections of Chlorine Nitrate in the  $\nu_2$  Band Region Around 1292 cm<sup>-1</sup> at Stratospheric Temperatures, *J. Geophys. Res.*, 99, 14,549-14,555, 1994.
- Rothman, L.S., C.P. Rinsland, A. Goldman, S.T. Massie, D.P. Edwards, J.-M. Flaud, A. Perrin, C. Camy-Peyret, V. Dana, J.-Y. Mandin, J. Schroeder, A. McCann, R.R. Gamache, R.B. Wattson, K. Yoshino, K.V. Chance, K.W. Jucks, L.R. Brown, V. Nemtchinov, and P. Varanasi, The HITRAN Molecular Spectroscopic Database and HAWKS (HITRAN Atmospheric Workstation): 1996 Edition, *J. Quant. Spectrosc. Radiat. Transfer*, 60, 665-710, 1998.
- Smith, K., D. Newnham, M. Page, J. Ballard, and G. Duxbury, Infrared Band Strengths and Absorption Cross-Sections of HFC-32 Vapor, *J. Quant. Spectrosc. Radiat. Transfer*, 56, 73-82, 1996.
- Smith, K., D. Newnham, M. Page, J. Ballard, and G. Duxbury, Infrared Absorption Cross-Sections and Integrated Absorption Intensities of HFC-134 and HFC-143a Vapour, *J. Quant. Spectrosc. Radiat. Transfer*, 59, 437-451, 1998.
- Varanasi, P., A. Gopalan, and J.F. Brannon Jr., Infrared Absorption Coefficient Data on SF<sub>6</sub> Applicable to Atmospheric Remote Sensing, *J. Quant. Spectrosc. Radiat. Transfer*, 48, 141-145, 1992a.

Varanasi, P., Absorption Coefficients of CFC-11 and CFC-12 needed for Atmospheric Remote Sensing and Global Warming Studies, *J. Quant. Spectrosc. Radiat. Transfer*, 48, 205-219, 1992b.

Varanasi, P., Absorption Spectra of HCFC-22 around  $829\text{ cm}^{-1}$  at Atmospheric Conditions, *J. Quant. Spectrosc. Radiat. Transfer*, 47, 251-255, 1992c.

Varanasi, P., and V. Nemtchinov, Thermal Infrared Absorption Coefficients of CFC-12 at Atmospheric Conditions, *J. Quant. Spectrosc. Radiat. Transfer*, 51, 679-687, 1994.

Varanasi, P., Z. Li, V. Nemtchinov, and A. Cherukuri, Spectral Absorption-Coefficient Data on HCFC-22 and SF<sub>6</sub> for Remote-Sensing Applications, *J. Quant. Spectrosc. Radiat. Transfer*, 52, 323-332, 1994.

Goody, R.M and Y.L. Yung, *Atmospheric Radiation, Theoretical Basis*, Second Edition, Oxford University Press, 1989.

### 3.3.8.3 Aerosols

Massie, S. T., Indices of refraction for the HITRAN compilation, *J. Quant. Spectrosc. Radiat. Transfer*, 52, 501-513, 1994.

Rinsland, C. P., G. K. Yue, M. R. Gunson, R. Zander, and M. C. Abrams, Mid-infrared extinction by sulfate aerosols from Mt. Pinatubo eruption, *J. Quant. Spectrosc. Radiat. Transfer*, 52, 241-252, 1994.

Rothman, L.S., C.P. Rinsland, A. Goldman, S.T. Massie, D.P. Edwards, J.-M. Flaud, A. Perrin, C. Camy-Peyret, V. Dana, J.-Y. Mandin, J. Schroeder, A. McCann, R.R. Gamache, R.B. Wattson, K. Yoshino, K.V. Chance, K.W. Jucks, L.R. Brown, V. Nemtchinov, and P. Varanasi, The HITRAN Molecular Spectroscopic Database and HAWKS (HITRAN Atmospheric Workstation): 1996 Edition, *J. Quant. Spectrosc. Radiat. Transfer*, 60, 665-710, 1998.

### 3.3.8.4 Continuum

Clough, S. A., F. X. Kneizys, and R. W. Davies: Line shape and the water vapor continuum, *Atmos. Res.*, 23, 229-241, 1980.

Clough, S.A. and M.J. Iacono, Line-by-Line Calculations of Atmospheric Fluxes and Cooling Rates II: Application to Carbon Dioxide, Ozone, Methane, Nitrous Oxide, and the Halocarbons. *J. Geophys. Res.*, 100, 16,519-16,535, 1995.

Clough, S.A., The water vapor continuum and its role in remote sensing, in *Optical Remote Sensing of the Atmosphere, Vol. 2, 1995, OSA Technical Digest Series*, Optical Society of America, Washington, DC, pp. 76-81, 1995.

Clough, S.A., M.J. Iacono, J.-L. Moncet, Line-by-Line Calculation of Atmospheric Fluxes and Cooling Rates: Application to Water Vapor. *J. Geophys. Res.*, 97, 15761-15785, 1992.

Clough, S.A., F.X. Kneizys, and R. W. Davies, Line shape and the water vapor continuum. *Atmospheric Research*, 23, 229-241, 1989.

Han, Y., J.A. Shaw, J.H. Churnside, P.D. Brown and S. A. Clough, Infrared spectral Radiance measurements in the tropical Pacific atmosphere, *J. Geophys. Res.*, 102, 4,353-4,356, 1997.

Lafferty, W.J., A.M. Solodov, A. Weber, W.B. Olson and J. M. Hartmann, Infrared collision-induced absorption by N<sub>2</sub> near 4.3 microns for atmospheric applications: measurements and empirical modeling, *Appl. Optics*, 35, 5911-5917, (1996).

Mlawer, E.J., S.A. Clough, P.D. Brown, and D.C. Tobin, A new formulation for the water vapor continuum, *Proceedings of the 8th Atmospheric Radiation Measurement (ARM) Science Team Meeting*, Tucson, Arizona, 1999 (in press).

Thibault, F., V. Menoux, R. Le Doucen, L. Rosenman, J.-M. Hartmann, and Ch. Boulet Infrared collision-induced absorption by O<sub>2</sub> near 6.4 microns for atmospheric applications: measurements and empirical modeling, *Appl. Optics*, 35, 5911-5917, 1996.

Tobin, D. C., F. A. Best, P. D. Brown, S. A. Clough, R. G. Dedeker, R. G. Ellingson, R. K. Garcia<sup>1</sup>, H. B. Howell, R. O. Knuteson, E. J. Mlawer, H. E. Revercomb, J. F. Short, P. F. W van Delst, and V. P. Walden, Downwelling Spectral Radiance Observations at the SHEBA Ice Station: Water Vapor Continuum Measurements from 17-26 micrometer, *J. Geophys. Res.*, 1999, in press.

Tobin, D.C., L.L. Strow, W.J. Lafferty and W.B. Olson, Experimental investigation of the self- and N<sub>2</sub>-broadened continuum within the  $\nu_2$  band of water vapor, *Appl. Opt.*, 35, 4274-4734, 1996.

### 3.5 Retrieval

Fletcher, R., *Practical Methods of Optimization*, 2<sup>nd</sup> Edition, John Wiley & Sons, 1993.

Gill, P. E., W. Murray, and M. H. Wright, *Practical Optimization*, Academic Press, 1981.

Lambert, A., R.G. Grainger, J.J. Remedios, W.J. Reburn, C.D. Rodgers, F.W. Taylor, J.L. Mergenthaler, J.B. Kumer, S.T. Massie and T. Deshler, Validation of Aerosol Measurements by the Improved Stratospheric And Mesospheric Sounder, *J. Geophys. Res.*, 101, 9811-9830, 1996.

Press, W. H., B. P. Flannery, S. A. Teukolsky, and W. T. Vetterling, *Numerical Recipes*, Cambridge University Press, New York, 1989.

Twomey, S. On the numerical solution of Fredholm integral equations of the first kind by the inversion of the linear system produced by quadrature. *J. Ass. Comput. Mach.*, 10, p 97, 1963.

Wylie, D.P., W.P. Menzel, H.M. Woolf, and K.I. Strabala: Four Years of Global Cirrus Cloud Statistics Using HIRS. *J. Climate*, 7, 1972-1986, 1994.

### **3.5.1.6 Strategy for Limb Pointing Retrieval**

Anderson, G.P., S.A. Clough, F.X. Kneizys, J.H. Chetwynd, and E.P. Shettle, *AFGL atmospheric constituent profiles (0-120 km)*. AFGL-TR-86-0110, 1986.

### **3.5.3 A Priori Constraints**

T. Steck, “Methods for determining regularization for atmospheric retrieval problems”, *Applied Optics*, Vol. 41, No. 9, March 2002. pp 1788.

T. Steck and T. von Clarmann, “Constrained profile retrieval applied to the observation mode of the Michelson Interferometer for Passive Atmospheric Sounding”. *Applied Optics*, Vol. 40, No. 21, pp 3559

### **3.5.4.1 The additive noise model and cost function**

Papoulis, A., *Probability, Random Variables, and Stochastic Processes*, McGraw-Hill, New York, 1984.

### **3.5.4.1 Initial Guess Refinement**

Bowman, K. W., Worden, J.R., Steck, T., Worden, H.M., Clough, S.A., Rodgers, C.D., “Capturing Time and Vertical Variability of Tropospheric Ozone: A Study using TES Nadir Retrievals”, *JGR-Atmospheres*, in press

Clough S. A., Worden, J.R., Brown, P.D., Shepard, M.W., Rinsland, C.P., Beer, R. “Retrieval of tropospheric ozone from simulations of limb spectral radiances as observed from space.”, *JGR-atmospheres*, in press

### **3.5.4.3 Numerical Solution**

Moré, J. Jorge, *The Levenberg-Marquardt Algorithm: Theory and Implementation*, *Numerical Analysis: Proceedings, Biennial Conference*, Dundee, 1977.

Marquardt, D., An algorithm for least squares estimation of nonlinear parameters., *J. Soc. Indust. Appl. Math* 11:431-441,1963.

### **3.5.5 Clear Pixel Identification (nadir)**

Wylie, D.P., W.P. Menzel, H.M. Woolf, and K.I. Strabala, 1994: Four Years of Global Cirrus Cloud Statistics Using HIRS. *J. Climate*, 7, 1972-1986.

Ackerman, S.A., K. Strabala, W.P. Menzel, R.A. Frey, C.C. Moeller and L.E. Gumley, “Discriminating clear sky from clouds with MODIS”, *J. Geophys. Res.*, 103, 32141-32157, 1998.

### 3.5.7 Retrieval Microwindow Selection

Rodgers, C. D. Information content and optimisation of high spectral resolution measurements, SPIE, Vol 2830, *Optical Spectroscopic Techniques and Instrumentation for Atmospheric and Space Research II*, Paul B. Hays and Jinxue Wang, eds., 136-147, 1996.

von Clarmann, T and G. Echle, Selection of optimized microwindows for atmospheric spectroscopy, *Appl Opt.*, 37, 7661-7669, 1998.

### 3.5.8 A Priori Database Generation

Heinemann, G., N.S. Chedin, N. Scott and C. Claud, Sensitivity studies of TOVS retrievals with 3I and ITPP retrieval algorithms. Application to the resolution of mesoscale phenomena in the Antarctic, *Meteorology and Atmospheric Physics*, v55, pp87-100, 1995.

Logan, J.A., An analysis of ozonesonde data for the troposphere: recommendations for testing 3-D models and development of a gridded climatology for tropospheric ozone, submitted to *J.Geophys. Res.*, July 1998.

Logan, J.A., An analysis of ozonesonde data for the lower stratosphere: recommendations for testing models, submitted to *J.Geophys. Res.*, July 1998.

# TROPOSPHERIC EMISSION SPECTROMETER (TES)

## LEVEL 2 ALGORITHM THEORETICAL BASIS DOCUMENT APPENDIX

Reinhard Beer	Jet Propulsion Laboratory
Kevin W. Bowman	Jet Propulsion Laboratory
Patrick D. Brown	Atmospheric and Environmental Research Inc.
Shepard A. Clough	Atmospheric and Environmental Research Inc.
Aaron Goldman	University of Denver
Daniel J. Jacob	Harvard University
Jennifer A. Logan	Harvard University
Mingzhao Luo	Jet Propulsion Laboratory
Frank J. Murcray	University of Denver
David M. Rider	Jet Propulsion Laboratory
Curtis P. Rinsland	NASA Langley Research Center
Clive D. Rodgers	University of Oxford
Stanley P. Sander	Jet Propulsion Laboratory
Eugene Ustinov	Jet Propulsion Laboratory
Helen M. Worden	Jet Propulsion Laboratory
Marguerite Syvertson, editor	Jet Propulsion Laboratory

---

Approved by:  
Reinhard Beer  
TES Principal Investigator

Version 1.15  
April 8, 2002

Jet Propulsion Laboratory  
California Institute of Technology  
Pasadena, California

## **TES Level 2 Algorithm Theoretical Basis Document**

---

This document was prepared at the Jet Propulsion Laboratory, California Institute of Technology, under a contract from the National Aeronautics and Space Administration

# TABLE OF CONTENTS

<b>TABLE OF CONTENTS</b>	<b>I</b>
<b>I. LIST OF FIGURES</b>	<b>I</b>
<b>II. LIST OF TABLES</b>	<b>II</b>
<b>APPENDICES</b>	<b>1</b>
A3.3.1: Radiative Transfer	1
A3.3.3 Radiative Transfer for Clouds and Aerosols	20
<b>A3.4: Analytic Jacobians</b>	<b>32</b>
A3.4.1 Partial with respect to layer optical depth (OD) $\frac{\partial L_{sat}}{\partial \tau_l}$	33
A3.4.2 Partial of optical depth with respect to gas species VMR $\frac{\partial \tau_l}{\partial x_l}$	36
A3.4.3 Partial with respect to layer Planck (or effective Planck) function $\frac{\partial L_{sat}}{\partial B_l}$	38
A3.4.4 Partial of layer Planck (or effective Planck) function with respect to temperature $\frac{\partial B_l}{\partial T_l}$	39
A3.4.5 Partial of optical depth with respect to temperature $\frac{\partial \tau_l}{\partial T_l}$	39
A3.4.6 Layer-to-Level Jacobians	42
A3.4.7 Pointing Jacobians	45
A3.4.8 Jacobian Validation	46
<b>A3.5.1 Retrieval Strategy</b>	<b>49</b>
<b>REFERENCES</b>	<b>52</b>

## I. LIST OF FIGURES

Figure A-1: Earth Geometric Model	1
Figure A-2: Propagation of a refracted ray through the limb	6
Figure A-3: NO kinetic, v=1, and v=2 vibrational temperatures in the daytime. Digitized from Funke and Puertas [2000].	14
Figure A-4: NO kinetic, v=1, and v=2 vibrational temperatures in the nighttime. Digitized from Funke and Puertas [2000].	15
Figure A-5: US standard atmosphere profiles of NO mixing ratio and temperature [Anderson et. al., 1986].	16

Figure A-6: TES LBLRTM computed spectra of NO under Non-LTE ( $v=1$ ) daytime conditions for a limb path with a tangent height of 15 km. The results are plotted in both brightness temperature (top) and radiance (bottom).	17
Figure A-7: Difference plot between TES LBLRTM calculated radiances under Non-LTE ( $v=1$ ) and LTE (kinetic temperature) conditions.	18
Figure A-8: Layer and level view for downwelling OD jacobian calculation	35
Figure A-9: Layer and level view for upwelling OD jacobian calculation	35
Figure A-10:	47
Figure A-11:	48
Figure A-12:	49

## **II LIST OF TABLES**

Table A-1: Summary of results for Non-LTE vs. LTE TES LBLRTM calculations.	19
Table A-2: USGS Land Use/Land Cover System Legend and Assignment of Material Type from the ASTER Spectral Library ( <a href="http://speclib.jpl.nasa.gov/">http://speclib.jpl.nasa.gov/</a> )	20
Table A-3: Nadir jacobian comparisons: Finite Difference (FD) to Analytic	47
TableA- 4: Limb jacobian comparisons: Finite Difference (FD) to Analytic	48

THIS PAGE INTENTIONALLY LEFT BLANK.

## APPENDICES

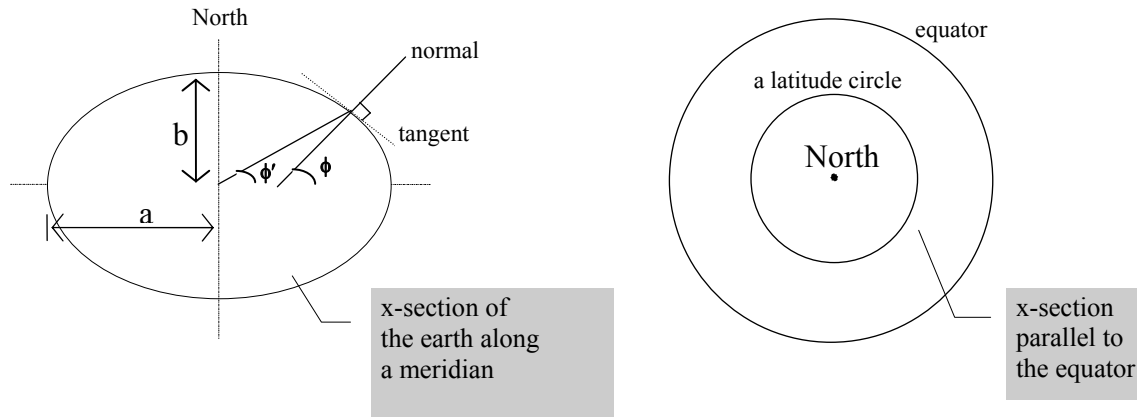
### A3.3.1: Radiative Transfer

The Radius of Curvature of the Earth’s Surface for a Given TES Limb Tangent Latitude and Viewing Direction

The ray-tracing step in Level 2 process uses Snell’s Law for a spherically symmetric atmosphere to determine the bending along the ray. The radius of the “sphere” is considered to be the sum of the altitude and the *radius of curvature of the Earth surface* (not the Earth-centered radius) at the given location in the given direction. This Appendix presents the equations for the radius of the Earth surface curvature at a given latitude (TES limb tangent latitude) for TES viewing direction.

A very commonly used Earth geometric model is an ellipsoidal shape as illustrated below.

**Figure A-1: Earth Geometric Model**



Definitions of some parameters:

- $a$  — equatorial radius (the semi-major axis of the meridian ellipse).
- $b$  — polar radius (the semi-minor axis of the meridian ellipse).
- $f$  — flattening factor.
- $e$  — Earth ellipsoid eccentricity.
- $\phi$  — geodetic latitude as illustrated above.
- $\phi'$  — geocentric latitude as illustrated above.

Their relationships:

$$\tan(\phi) = \frac{\tan(\phi')}{(1-f)^2}; \quad (\text{A.1})$$

$$f = \frac{a-b}{a}; \text{ and} \quad (\text{A.2})$$

$$e = \sqrt{2f - f^2} . \tag{A.3}$$

There are two principle curvatures on the model Earth surface at a given location, the meridian curvature (North-South curvature) and the East-West curvature. The tangents of these two curvature are perpendicular. The East-West curvature plane is defined by the tangent along a latitude circle and the local normal. The equations for the radius of these two principle curvature planes are:

Radius of curvature in the North-South plane:

$$R_{NS} = \frac{a(1-e^2)}{(1-e^2 \sin^2 \phi)^{3/2}} . \tag{A.4}$$

Radius of curvature in the East-West plane:

$$R_{EW} = \frac{a}{(1-e^2 \sin^2 \phi)^{1/2}} . \tag{A.5}$$

TES always looks straight backward along the orbit. The orbit has 98.21° inclination angle which is the angle between the equatorial plane and the orbital plane. The parameter to define the TES viewing direction at its limb tangent point or any point along its line of sight is the azimuth angle ( $A_z$ ). The azimuth angle is the angle between the local meridian plane (the N-S plane) and the plane defined by the local normal and the tangent along the TES viewing direction. Under the spherical approximation,  $A_z$  can be calculated as

$$\sin(A_z) = \frac{\cos(\text{inclination\_angle})}{\cos(\text{geocentric\_latitude}, \phi')} . \tag{A.6}$$

The EOS Toolkit provides a program to calculate a more rigorous azimuth without the spherical approximation (PGS\_CSC\_ZenithAzimuth). The viewing vector however, in the ECR (Earth Centered Rotating) coordinate system, needs to be defined.

The radius of the curvature in azimuth  $A_z$  ( $R_C$ ) can be calculated as

Radius of curvature in azimuth  $A_z$ :

$$\frac{1}{R_C} = \frac{\cos^2(A_z)}{R_{NS}} + \frac{\sin^2(A_z)}{R_{EW}} . \tag{A.7}$$

### A3.3.1.1: Ray Tracing and Path Integrals

For ray tracing and path integrals, we require the following elements from the retrieval vector, at a set of levels  $j=0..n$  in  $\ln(P)$ , and in the limb case when the atmosphere is not horizontally homogeneous, also at a set of locations along the line of sight:

- $T_j$  level temperatures
- $q_{jm}$  level mixing ratios for molecule  $m$
- $P_s$  surface pressure
- $T_s$  surface temperature

and the following forward model parameters:

- $z_s$  altitude of the surface relative to the geoid
- $R_c$  radius of the geoid at the measurement location
- $R_{cs}$  altitude of the spacecraft from the center of curvature of the geoid
- $\theta_s$  angle of ray at the satellite

The level quantities in the retrieval vector are interpolated at a finer spacing to give the full grid level values  $q_k^m$  and  $T_k$ .

#### A3.3.1.1.1 Hydrostatic Equation

The total air density  $\rho_k$  is computed from the gas equation at each full grid level. This must allow for the water content of the air, but the other minor constituents may be ignored [except possibly  $\text{CO}_2$ ] (see Appendix 3.3.1.1.7). The hydrostatic equation may be written

$$dz = -[P/\rho(P)g(z)] d \ln(P) \quad (\text{A.8})$$

As the quantity  $[P/\rho(z)g(z)]$  is close to  $RT/Mg$ , from the ideal gas equation, we take it to be linear in  $\ln(P)$  over each layer. Hence the layer thickness is

$$z_k - z_{k-1} = (P_{k-1}/r_{k-1}g_{k-1} + P_k/\rho_k g_k)[\ln(P_{k-1}) - \ln(P_k)]/2 \quad (\text{A.9})$$

from the trapezoidal rule. The acceleration due to gravity is given as a function of height and latitude, and it consists of gravitational and rotational parts,

$$g(\phi, z) = g_{\text{grav}}(\phi, 0)[(R_e)/(R_e + z)]^2 - \Omega^2 N[((N+z)/R_e)\cos\phi]^2 \quad (\text{A.10})$$

where  $\Omega$  is the Earth's rotational angular frequency;  $N = a^2 \sqrt{(a^2 - (a^2 - b^2)\sin^2 \phi)}$ ; and  $a$  and  $b$  is the semi-major and minor axis of earth respectively. The gravitational term at the earth surface is given by [International Gravity Formula, 1980]

$$g(\phi, 0) = 978.0327(1.0 + 0.0052790414 \sin^2 \phi + 0.0000232718 \sin^4 \phi + 0.0000001262 \sin^6 \phi) \quad (\text{A.11})$$

and,

$$g_{grav}(\phi, 0) = g(\phi, 0) - g_{rot}(\phi, 0). \quad (\text{A.12})$$

Note that equation (A.12) requires  $g_k = g(z_k)$  before  $z_k$  has been computed. The effect is small and can be accommodated by several different ways, of which the simplest might be to approximate  $g_k$  by its value at an altitude given by  $2z_{k-1} - z_{k-2}$ .

#### A3.3.1.1.2 Ray tracing in the nadir case.

The zenith angle of the ray at each level is given by Snell's law in spherical symmetry:

$$\sin \theta_k = [R_{cs} \sin \theta_s] / [(R_c + z_k) n_k] \quad (\text{A.13})$$

where the refractive index  $n_k$  is given in section A3.3.1.1.8. However as  $n_k \sim 1.0002$  at the surface, it may be ignored, incurring an error of only 0.02% in  $\sin \theta_k$ , and hence a similarly small amount in path length through  $\sec \theta_k$ .

#### A3.3.1.1.3 Path integrals in the nadir case

We need to evaluate the number of molecules per unit area in each layer, together with appropriately weighted mean pressures and temperatures of the layer. The mass per unit area of an element  $dP$  is  $dP/g$ , so the number of molecules of molecule  $m$  is

$$dn_m = N q_m dP / g [M_d + q^w M_w] \quad (\text{A.14})$$

where  $N$  is Avogadro's number,  $q_m$  is the volume mixing ratio of molecule  $m$ , defined as the ratio to the number of molecules of dry air,  $M_d$  and  $M_w$  are the molar masses of dry air and water, and  $q^w$  is the mixing ratio of water vapor. Hence the number of molecules of  $m$  in a layer along the line of sight is

$$u_{lm} = \int_{l_{l-1}}^{l_l} q_m(P) f(P) dP \quad (\text{A.15})$$

where

$$f(P) = \sec \theta N / g [M_d + q^w M_w] \quad (\text{A.16})$$

is very nearly constant over a layer. Interpolating  $\ln(f)$  as well as  $\ln(q_m)$  linearly in  $\ln(P)$ , we obtain integrals that can be evaluated analytically. Putting

$$q_m f = q_{ml-1} f_{l-1} (P / P_{l-1})^{\alpha_l} \quad (\text{A.17})$$

within the layer, where  $\alpha_l = \ln(q_{ml} f_l / q_{ml-1} f_{l-1}) / (\zeta_l - \zeta_{l-1})$ , we obtain

$$\begin{aligned}
 u_{lm} &= [q_{m-1} f_{l-1} P_{l-1} - q_m f_l P_l] / (1 + \alpha_l) \\
 &= q_{m-1} f_{l-1} P_{l-1} (\zeta_l - \zeta_{l-1}) E[(1 + \alpha_l)(\zeta_l - \zeta_{l-1})]
 \end{aligned}
 \tag{A.18}$$

where  $E(x) = [1 - \exp(-x)]/x$ , which will need special evaluation near  $x=0$ . The first form is simpler, but the second form is needed when  $(1 + \alpha_l) \sim 0$ . We also require the weighted mean pressure and temperature obtained from

$$u_{lm} \bar{P}_l = - \int_{l-1}^l q_m f P dP \tag{A.19}$$

$$u_{lm} \bar{T}_l = - \int_{l-1}^l q_m f T dP \tag{A.20}$$

in order to evaluate the optical depth

$$\tau_v = k_v(\bar{P}, \bar{T}) u \tag{A.21}$$

where  $k_v$  is the absorption coefficient (cross section) to be interpolated from a tabulation against pressure and temperature. We easily obtain

$$\begin{aligned}
 u_{lm} \bar{P}_l &= [q_{m-1} f_{l-1} P_{l-1}^2 - q_m f_l P_l^2] / (2 + \alpha_l) \\
 &= q_{m-1} f_{l-1} P_{l-1}^2 (\zeta_l - \zeta_{l-1}) E[(2 + \alpha_l)(\zeta_l - \zeta_{l-1})]
 \end{aligned}
 \tag{A.22}$$

The temperature integral can also be performed algebraically, but leads to slightly more complicated expressions.

For computational efficiency we wish to avoid a two dimensional interpolation in the absorption coefficient tables. The mean pressure is therefore approximated by its value at  $\alpha_l = 0$ , and the tabulation made at the corresponding set of layer mean pressures,  $\bar{P}_l = (P_l + P_{l-1})/2$ . This approximation is in error by 1.2% in pressure at  $\alpha = <1$  for a layer thickness of 1 UARS layer, and is quadratic in layer thickness.

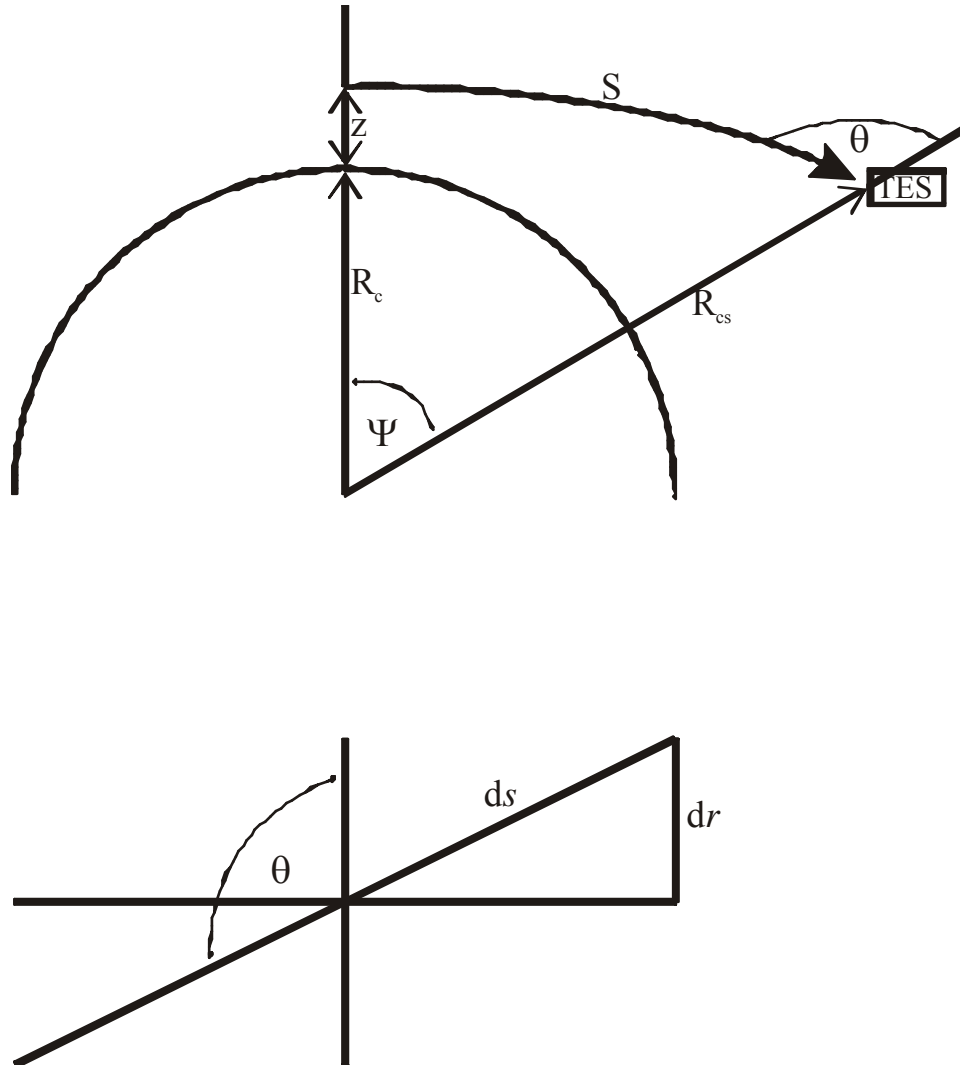
#### *A3.3.1.1.4 Ray Tracing in the Limb Case*

To avoid a pressure interpolation in the absorption coefficient table in the forward model, we need to predetermine the layer mean pressures in order to tabulate at the required pressures. Therefore we ray trace forward from a set of tangent points on the full grid (with given pressures) and evaluate the forward model for these rays, rather than tracing from the satellite in a set of directions related to the detector array. The ray trace will provide an angle of incidence at the satellite, so that a quadrature over the field of view of each detector can be carried out.

The use of a pressure grid involves an extra complication, because ray tracing is essentially a geometric procedure, best carried out in height coordinates, while the state vector is defined in pressure coordinates. In the case when horizontal homogeneity is assumed, the approach is relatively straightforward, following the principles of the method used in Kneizys *et al.* (1983). The quantities required from the ray trace are the angle of the ray at the satellite, and the pressure

as a function of distance along the ray, so that path integrals such as  $\int q\rho ds$ ,  $\int q\rho P ds$ , and  $\int \rho T ds$  can be evaluated for each layer.

**Figure A-2: Propagation of a refracted ray through the limb**



First we use the hydrostatic equation to obtain the heights  $z_k$  of the pressure levels for the full grid. These will not be equally spaced in height. We then trace a ray from each  $z_k$  as tangent height to the altitude of the satellite, relative to the center of curvature of the geoid. See Figure A-2 to define the terminology. For the refracted ray in the horizontally homogeneous case, the zenith angle of the ray at any altitude can be obtained from Snell's law:

$$n(r)r \sin \theta(r) = r_m \tag{A.23}$$

where  $r = z + R_c$  and  $r_g = n(r)r_t = R_{cs} \sin\theta_s$ , is a constant for the ray, the geometric tangent radius or the *impact parameter*. Using

$$dr = \cos\theta ds \quad (\text{A.24})$$

we obtain

$$ds = (1 - r_g^2/n^2r^2)^{-1/2} dr \quad (\text{A.25})$$

which cannot easily be integrated numerically to obtain  $s(r)$  because of the singularity at the tangent point. However by changing the variable of integration from  $r$  to  $x = r\cos\theta$  we can obtain

$$ds = dx/[1 - \gamma(r)\sin^2\theta(r)] \quad (\text{A.26})$$

where  $\gamma = -(r/n)\partial n/\partial r$ , a positive quantity, is an explicit function of  $r$ , as is  $\sin\theta$ . The coordinate  $x$  has the property that in the absence of refraction,  $x = s$ . To integrate over each full grid layer, we choose a set of quadrature points  $x_l$  within the layer, and use e.g. the trapezium rule:

$$\Delta s = \sum_i (x_i - x_{i-1}) (1/(1 - \gamma_i \sin^2\theta_i) + 1/(1 - \gamma_{i-1} \sin^2\theta_{i-1})) / 2 \quad (\text{A.27})$$

or some higher order integration rule. Note that it is not straightforward to find the altitudes of a set of points equally spaced in  $x$  because  $x^2 = r^2 - r_g^2/n^2(r)$  cannot be explicitly inverted to give  $r(x)$ , even though  $x$  can be evaluated at any given value of  $r$ . Either  $r^2(x) = x^2 + r_g^2/n^2(r)$  must be evaluated iteratively, or points chosen in  $r^2$  to make them approximately evenly spaced in  $x$ .

The refractive index of air is given in section A3.3.1.1.8 as an experimentally fitted function of pressure, temperature and water vapor. However it is close to being of the form  $n = 1 + \alpha\rho(r)$ , where  $\alpha$  is a constant, so that within each narrow layer, such as the full grid layer, it may be reasonably fitted to the form

$$n = 1 + \alpha\rho_0 \exp(-r/H_n) \quad (\text{A.28})$$

so that we can write

$$\partial n/\partial r = -(n - 1)/H_n \quad (\text{A.29})$$

where  $H_n$  is the scale height of refractivity,  $n-1$ , within the layer.

#### A3.3.1.1.5 Path Integrals for the Limb Case

The absorber amount of molecule  $m$  in a sublayer,  $\Delta u_m = \int q_m \rho ds$  can be evaluated in the same way as  $\Delta s$  by integrating with respect to  $x$  using the trapezium (or other) rule:

$$\Delta u_m = \sum_i (x_i - x_{i-1})(q_{lm}\rho_i/(1-\gamma_i\sin^2\theta_i) + q_{ml-1}\rho_{i-1}/(1-\gamma_{i-1}\sin^2\theta_{i-1}))/2 \quad (\text{A.30})$$

The effective pressure for a full grid layer is defined by

$$\bar{P} = \int \rho P \, ds / \int \rho \, ds \quad (\text{A.31})$$

where the two integrals are evaluated as sums over sublayers within the full grid layer, the elements of the sums being

$$\int \rho P \, ds = \Delta(uP) = \sum_i (x_i - x_{i-1})(P_i\rho_i/(1-\gamma_i\sin^2\theta_i) + P_{i-1}\rho_{i-1}/(1-\gamma_{i-1}\sin^2\theta_{i-1}))/2 \quad (\text{A.32})$$

and

$$\int \rho \, ds = \Delta u = \sum_i (x_i - x_{i-1})(\rho_i/(1-\gamma_i\sin^2\theta_i) + \rho_{i-1}/(1-\gamma_{i-1}\sin^2\theta_{i-1}))/2 \quad (\text{A.33})$$

The integral over the lowest sublayers (close to the tangent point) should be evaluated using a quadratic rule.

The effective temperature for a full grid layer is defined by

$$\bar{T} = \int \rho T \, ds / \int \rho \, ds \quad (\text{A.34})$$

in a similar way to the effective pressure. The elements of the sum for the numerator are

$$\Delta(uT) = \sum_i (x_i - x_{i-1})(T_i\rho_i/(1-\gamma_i\sin^2\theta_i) + T_{i-1}\rho_{i-1}/(1-\gamma_{i-1}\sin^2\theta_{i-1}))/2 \quad (\text{A.35})$$

Again, the integral over the lowest sublayers should be evaluated using a quadratic rule.

#### *A3.3.1.1.6 Ray tracing in the Inhomogeneous Limb Case.*

It is marginal whether the change in the refracted path due to horizontal inhomogeneities is significant. In the worst case, the slope of a pressure surface of 0.001, corresponding to a geostrophic wind of 100 m s<sup>-1</sup>, gives an error in tangent height at mid troposphere of order 40 m, or about 0.5% in pressure or density. Nevertheless we give the following analysis to describe a possible approach, should it be needed on further investigation.

In the general case the refraction equations do not have an explicit solution expressible as integrals, unlike the horizontally homogeneous case. A set of coupled ordinary differential equations can be derived, relating  $r(s)$ ,  $\theta(s)$  and  $\psi(s)$ :

$$d(\theta+\psi)/ds = -\sin\theta/n (\partial n/\partial r)_\psi + (\cos\theta/rn)(\partial n/\partial \psi)_r \quad (\text{A.36})$$

$$dr/ds = \cos\theta \quad (\text{A.37})$$

$$d\psi/ds = \sin\theta/r \quad (\text{A.38})$$

where  $\psi$  is the angle at the center of curvature relative to the instrument. The first equation states that the curvature of the ray is equal to the fractional gradient of the refractive index normal to the ray. The others are simple geometry. We can use (A.36) and (A.38) to obtain:

$$d\theta/ds = -\sin\theta[1/r + 1/n (\partial n/\partial r)_\psi] + (\cos\theta/rn)(\partial n/\partial \psi)_r \quad (\text{A.39})$$

Equations (A.36), (A.37) and (A.38) can be integrated by any standard differential equation solver such as Runge-Kutta to give  $r(s)$ ,  $\theta(s)$  and  $\psi(s)$ .

The boundary conditions cause difficulties, however. A single ray must pass through the instrument at a known location, and have a tangent point at a given pressure level:

- (i) at  $s = 0$ ,  $\psi(0) = 0$  and  $r(0) = R_{cs}$
- (ii) at  $r=r(\zeta_i)$ ,  $\cot\theta = - (1/r)(\partial r/\partial \psi)_\zeta$ , i.e the slope of pressure surface  $\zeta_i$

where  $\zeta = -\ln(P/P_0)$ . Here I have put the origins of  $\psi$  and  $s$  at the instrument for convenience. We do not know before the ray trace where  $\psi$  of the tangent point is relative to the satellite. (This does not matter in the case of the horizontally homogeneous atmosphere.) Therefore we must solve the problem iteratively by either:

- (a) finding the value of  $\psi$  at the tangent point for which the ray passes through the instrument, or
- (b) finding the scan angle  $\theta_s$  at the satellite which gives a tangent point at the right pressure level

To locate the tangent point relative to the satellite, it is most convenient to locate the origin of  $s$  at the tangent point and the origin of  $\psi$  at the instrument. The initial conditions are, at the tangent point

$$(i) s = 0 \quad (ii) r = r_t \quad (iii) \psi = \psi_t \quad (iv) \cot\theta = -(1/r)(\partial r/\partial \psi)_\zeta.$$

Integrate forward from the tangent point until the ray reaches satellite altitude  $R_{cs}$ . The ray will miss the instrument by an amount  $\psi(R_{cs})$ . This quantity is then subtracted from  $\psi_t$  for the next iteration. If there were no line of sight gradients, we would need to go no further, but one more iteration will probably be necessary for convergence.

The temperature, water and (hence) the refractive index are specified vertically on the full grid, and horizontally at some set of values of  $\psi$ . Use the hydrostatic equation to find  $r$  on this same grid. Then the table can be used to find the partial derivatives  $(\partial n/\partial r)_\psi$ ,  $(\partial n/\partial \psi)_r$  and  $(\partial r/\partial \psi)_\zeta$  where they are required.

There is the extra complication that we want to find quadrature points along the rays lying on the full grid. We are at liberty to choose the quadrature points for the integration so we will change them as we iterate so that a subset ends up lying on the pressure grid. The suggested process is as follows, for each full grid level within the range seen by the instrument:

Repeat:

- Select a set of quadrature points in  $s$ :
- First time round, use  $s = ih, i=0,1..$  for some constant spacing  $h$ .
- Subsequent times we will have a reasonable guess at the ray path, so use the tangent point, plus points where the ray intersects the full grid (inverse interpolate in  $\zeta(s)$ ), subdividing sections so that no interval is longer than  $h$ .
- Adjust the initial condition  $\psi_t$
- Integrate forward & backward through the atmosphere to give  $r(s), \theta(s)$  and  $\psi(s)$ .
- Use a straight line ray from just outside the atmosphere where  $n=1$  to the satellite altitude to calculate the angle  $\psi_s$  by which the ray misses the instrument
- Evaluate  $\zeta(s)$  at each quadrature point (use  $r, \psi$  to interpolate in the 2-D profile table). until converged (fixed number of times, probably 3 or 4)

Carry out the path integrals using the same quadrature points and e.g. Simpsons rule.

The fixed number of iterations is required so that we safely can do a numerical perturbation of the ray trace for the Jacobian calculation.

A reasonable initial value for  $\psi_t$  can be obtained by starting with the highest tangent point required, initialized with the geometric (unrefracted) value, and work downwards, each time using the final value for the previous level as the initial value for the current level.

We should probably check for pathological circumstances such as the ray being refracted below the tangent level, by at least checking whether  $r < r_t!$  This applies to the homogeneous case too.

The alternative approach of finding the scan angle  $\theta_s$  at the satellite which gives a tangent point at the right pressure level turns out to be more complicated, and not worth pursuing:

#### *A3.3.1.1.7 The gas equation for air*

The gas equation for air is given by Ciddor [1996] as

$$\rho = \frac{M_{dry}}{R^*T} p \cdot \frac{\left[ 1 - X_{H_2O} \left( 1 - \frac{M_{H_2O}}{M_{dry}} \right) \right]}{Y}, \quad (A.40)$$

where  $R^* = 8.31451 \text{ J mole}^{-1} \text{ K}^{-1}$ , the universal gas constant;

$M_{dry} = [28.9635 + 12.011 * 10^{-6} (X_{CO_2} - 400)] * 10^{-3} \text{ kg/mole}$ ;

$X_{CO_2} = 1.5202 * q_{CO_2}$ ;

$M_{H_2O} = 0.018015 \text{ kg/mole}$ ;

$$X_{H_2O} = 0.6223 * q_{H_2O}; \text{ and}$$

the compressibility factor  $Y$  is given by

$$Y = 1 - (P/T)[a_0 + a_1 t + a_2 t^2 + (b_0 + b_1 t)X_{H_2O} + (c_0 + c_1 t)X_{H_2O}^2] + (P/T)^2(d + eX_{H_2O}^2)$$

where

$$\begin{aligned} a_0 &= 1.58123e^{-6} \\ a_1 &= 2.9331e^{-8} \\ a_2 &= 1.1043e^{-10} \\ b_0 &= 5.707e^{-6} \\ b_1 &= 2.051e^{-8} \\ c_0 &= 1.9898e^{-4} \\ c_1 &= 2.376e^{-6} \\ d &= 1.83e^{-11} \\ e &= -0.765e^{-8} \\ \text{and } t &= T - 273.15 \end{aligned}$$

#### A3.3.1.1.8 Refractive index of air

The index of refraction of air ( $n$ ) depends on frequency ( $\nu$ ), pressure ( $P$ ), temperature ( $T$ ) and water vapor amount (partial pressure  $P_{H_2O}$ ). Since the original Edlén equation was published in the early 1960's [Edlén, 1966], many revised empirical formulas have been published based on the new measurements. We use a revision of Edlén by Birch and Downs [1993 and 1994]:

$$\begin{aligned} n &= n_{tp} - f \cdot (a_9 - a_{10}\nu^2) \cdot 10^{-10}; \\ n_{tp} - 1 &= \frac{P(n_s - 1)}{a_5} \cdot \frac{[1 + 10^{-8}(a_6 - a_7 t)P]}{(1 + a_8 t)}; \text{ and} \\ (n_s - 1) \cdot 10^{-8} &= a_0 + a_1 \cdot (a_2 - \nu^2)^{-1} + a_3 \cdot (a_4 - \nu^2)^{-1}; \end{aligned} \tag{A.41}$$

where  $a_0$  to  $a_{10}$  are constants ( $a_0 = 8342.54$ ;  $a_1 = 2406147.0$ ;  $a_2 = 130.0$ ;  $a_3 = 15998.0$ ;  $a_4 = 38.9$ ;  $a_5 = 96095.43$ ;  $a_6 = 0.601$ ;  $a_7 = 0.00972$ ;  $a_8 = 0.003661$ ;  $a_9 = 3.7345$ ;  $a_{10} = 0.0401$ ; ),  $\nu$  is frequency in  $\text{mm}^{-1}$ ,  $P$  is pressure in Pa,  $t$  is temperature in  $^{\circ}\text{C}$  ( $t = T - 273.15$ ), and  $f$  is the partial pressure of water vapor.

Although the above formula was derived from measurements of visible and near infrared region, other measurements suggest that it could be extrapolated to the infrared region [Coleman *et al.*, U.S. NBS, "Table of Wavenumbers", 1960]. Note that frequency ( $\nu$ ) only has a secondary effect on  $n$ , so that the ray-trace step simply uses the averaged frequency for the forward model spectrum range in the calculation.

A3.3.1.5: Non-LTE

The single-line volumetric absorption  $\kappa_\nu$  and local thermal radiance  $R_\nu$  is given by

$$\kappa_\nu = \frac{h\nu}{4} \bar{B} (g_u n_l - g_l n_u) \phi_\nu \quad (\text{A.42})$$

and

$$R_\nu = \frac{h^2 \nu^4}{2\pi c^2} g_l n_u \chi_\nu, \quad (\text{A.43})$$

where

$$\chi_\nu = \phi_\nu e^{-h(\nu-\nu_0)/kT}, \quad (\text{A.44})$$

where  $n_l$  and  $n_u$  are the number density populations of the lower and upper V-R states and the constant integers  $g_l$  and  $g_u$ , are the respective single state degeneracy factors.

This result is a general one for a two-level system. The lineshapes,  $\chi_\nu$  and  $\phi_\nu$ , are functions of the bulk thermodynamic quantities such as pressure, temperature, plus individual gas densities which can separately influence the lineshapes. The populations are given by the Boltzman distribution only under conditions of local thermodynamic equilibrium. In the presence of a strong radiation field, or under conditions for which the relaxation rates are slow with respect to physical processes influencing the state populations, the upper and lower state populations are not simply related through Boltzmann factors associated with a characteristic temperature for the system and the source function for the radiance is no longer given by the Planck function.

In the present case for TES observations, several assumptions can be made which significantly simplify the Non-LTE problem: (1) the relevant transitions occur at low pressure so that the Doppler shape is dominant with the line shape for emission and absorption being the same; (2) the system is in translational equilibrium with a characteristic kinetic temperature (affects only the Doppler width); and (3) the system is in rotational equilibrium with a characteristic rotational temperature. In the present formulation, the Non-LTE radiative transfer is developed as an extension of the LTE radiative transfer minimizing complexity and computational cost. The Non-LTE vibrational state population variables can be used to relate the Non-LTE single-line absorption and radiance to the same quantities calculated for an atmosphere in equilibrium at the characteristic temperature  $\bar{T}$ . The relationship between non-equilibrium and equilibrium radiative properties for a single line can be summarized by

$$\kappa_\nu = \left[ \frac{g_u n_l - g_l n_u}{g_u n_l^e - g_l n_u^e} \right] \kappa_\nu^e \quad (\text{A.45})$$

and

$$R_v = \frac{n_u}{n_u^e} R_v^e, \quad (\text{A.46})$$

which can also be written in terms of the Planck function as

$$R_v = \frac{n_u}{n_u^e} B_v(\bar{T}) K_v^e. \quad (\text{A.47})$$

The superscript  $e$  denotes the equilibrium values of the respective quantities.

The ratios of non-LTE vibrational populations to their equilibrium values are given as enhancement (or depletion) ratios,

$$r_l = \frac{n_l}{n_l^e} \quad \text{and} \quad r_u = \frac{n_u}{n_u^e}. \quad (\text{A.48})$$

The single-line contributions to  $K_v$  and  $C_v$  due to a transition with wavenumber value  $\nu_o$  can be expressed simply in terms of these ratios according to

$$K_v = \left[ \frac{r_l - r_u \Delta}{1 - \Delta} \right] K_v^e \quad (\text{A.49})$$

and

$$C_v = \left[ \frac{r_l - r_u}{1 - \Delta} \right] K_v^e \quad (\text{A.50})$$

where  $\Delta$  is the Boltzman factor,

$$\Delta = \frac{g_l n_u^e}{g_u n_l^e} = e^{-h\nu_o/k\bar{T}}. \quad (\text{A.51})$$

The factors in brackets can be viewed as Non-LTE line strength correction factors. The functions,  $K_v$  and  $C_v$ , are obtained from the equilibrium values of the spectral absorption coefficients tabulated for individual vibrational states of a given molecular species. The quantities required for the calculation are  $r_l$ ,  $r_u$  and  $\nu_o$  for each Non-LTE vibrational state.

The complete solution of the radiative transfer equation for a homogeneous layer with column amount,  $u$ , is given by

$$L_v = L_v^o e^{-K_v u} + B_v(\bar{T}) \left[ 1 - \frac{C_v}{K_v} \right] \left[ 1 - e^{-K_v u} \right] \quad (\text{A.52})$$

where  $L_v^o$  is the radiation at the path boundary. The effect of solving the non-equilibrium problem for a homogeneous layer is effectively to modify the line strengths (equilibrium absorption coefficients) contributing to the local absorption coefficient  $K_v$ , and to replace the Planck function  $B_v$  by the high resolution function  $B_v(\bar{T})[1 - C_v / K_v]$ .

A3.3.1.5.1: Non-LTE: NO Example

Non-LTE will occur under conditions for which relaxation rates are slow with respect to physical processes influencing the state populations. Initial testing and sensitivity studies using TES LBLRTM are performed using the method outline above in section A3.3.1.5. The Non-LTE vibrational temperatures for NO at  $v=1$  state were obtained from Funke and Puertas [2000] Non-LTE model (refer to Figure A-3 and Figure A-4), and the mixing ratio from the AFGL NO profile [Anderson, et. al, 1986] (refer to Figure A-5). The results from the Non-LTE model for NO( $v \leq 2, J, S$ ) in Figure A-3 show that there is significant departure from LTE for NO( $v \geq 1$ ) in the stratosphere daytime as low as 15 km due to the production by NO<sub>2</sub> photolysis. The issue of rotational and spin distributions of NO( $v=1,2$ ) shown to be in Non-LTE above ~110 km must also be evaluated.

Figure A-3: NO kinetic,  $v=1$ , and  $v=2$  vibrational temperatures in the daytime. Digitized from Funke and Puertas [2000].

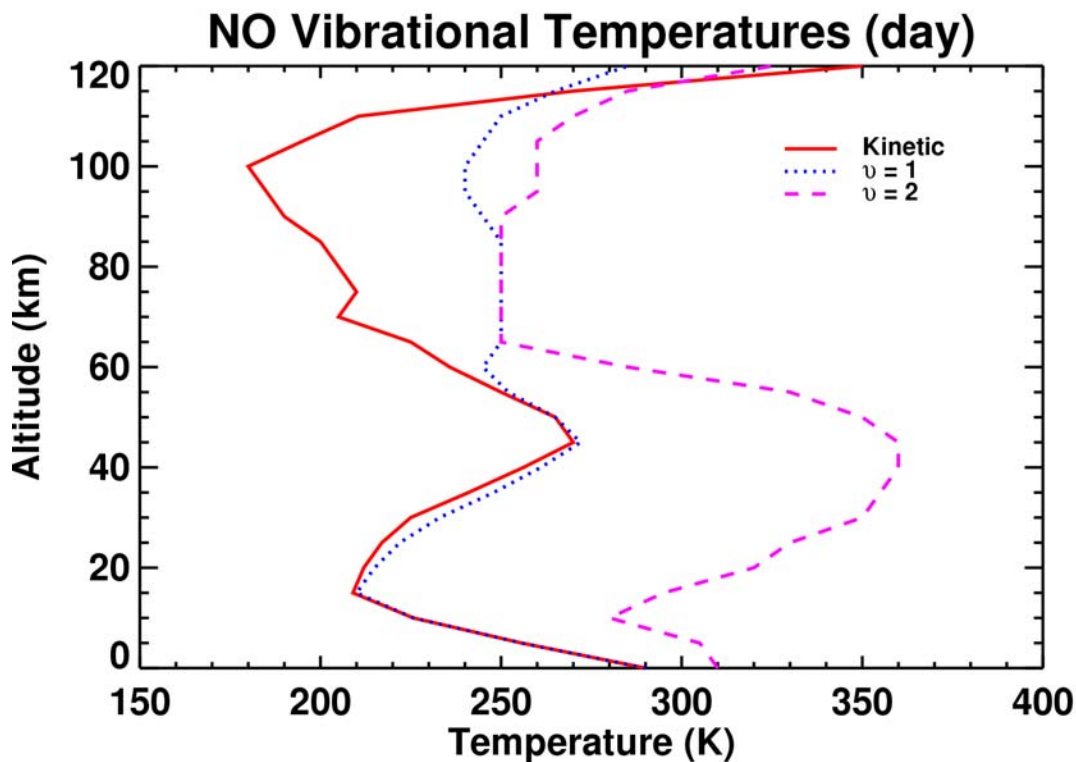


Figure A-4: NO kinetic,  $\nu=1$ , and  $\nu=2$  vibrational temperatures in the nighttime. Digitized from Funke and Puertas [2000].

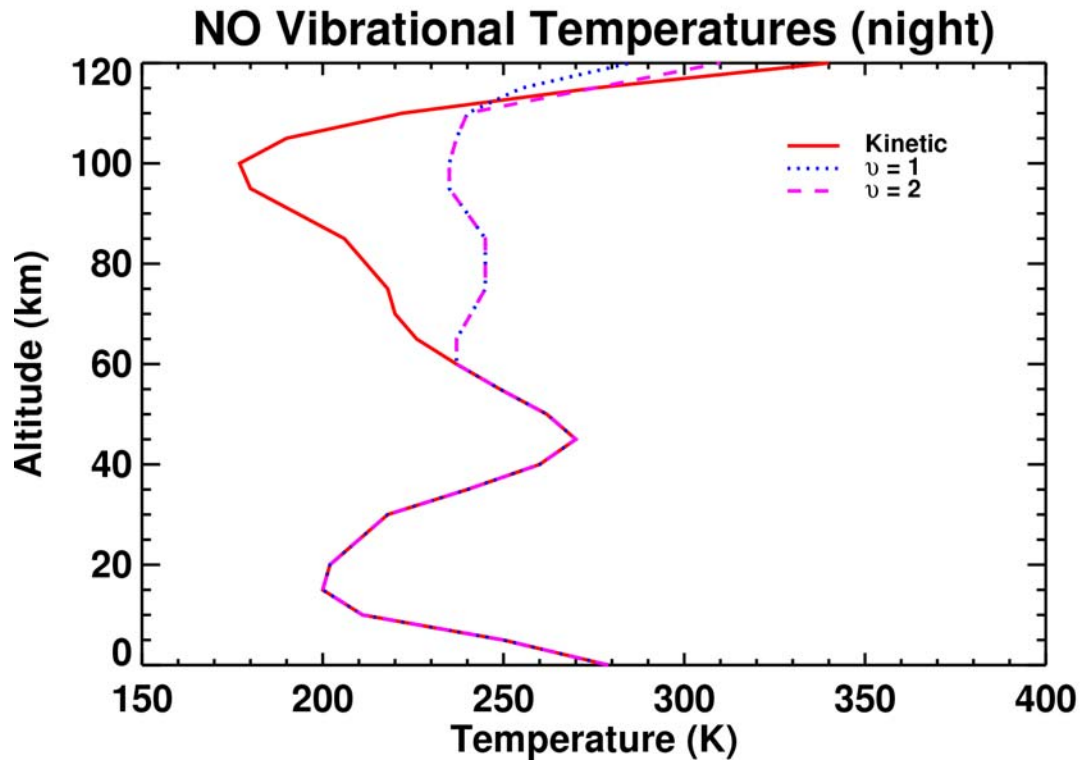


Figure A-5: US standard atmosphere profiles of NO mixing ratio and temperature [Anderson et. al., 1986].

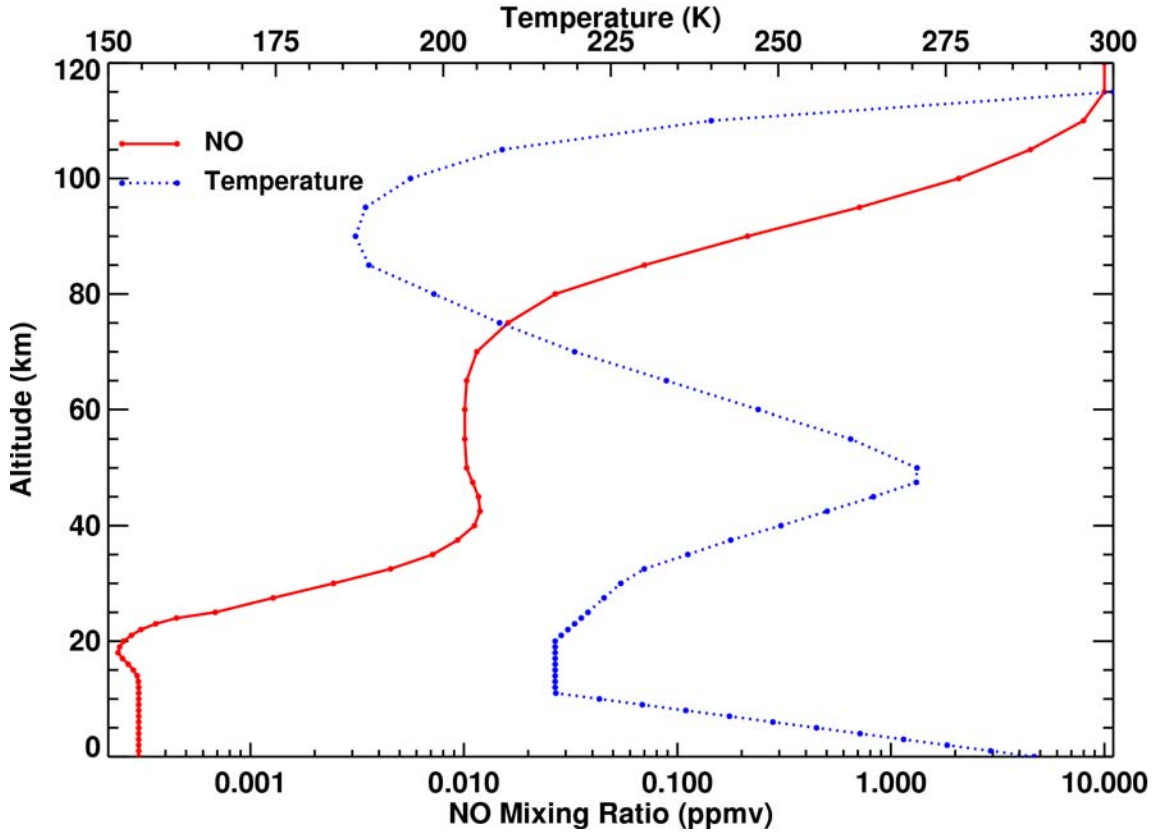


Figure A-6: TES LBLRTM computed spectra of NO under Non-LTE ( $v=1$ ) daytime conditions for a limb path with a tangent height of 15 km. The results are plotted in both brightness temperature (top) and radiance (bottom).

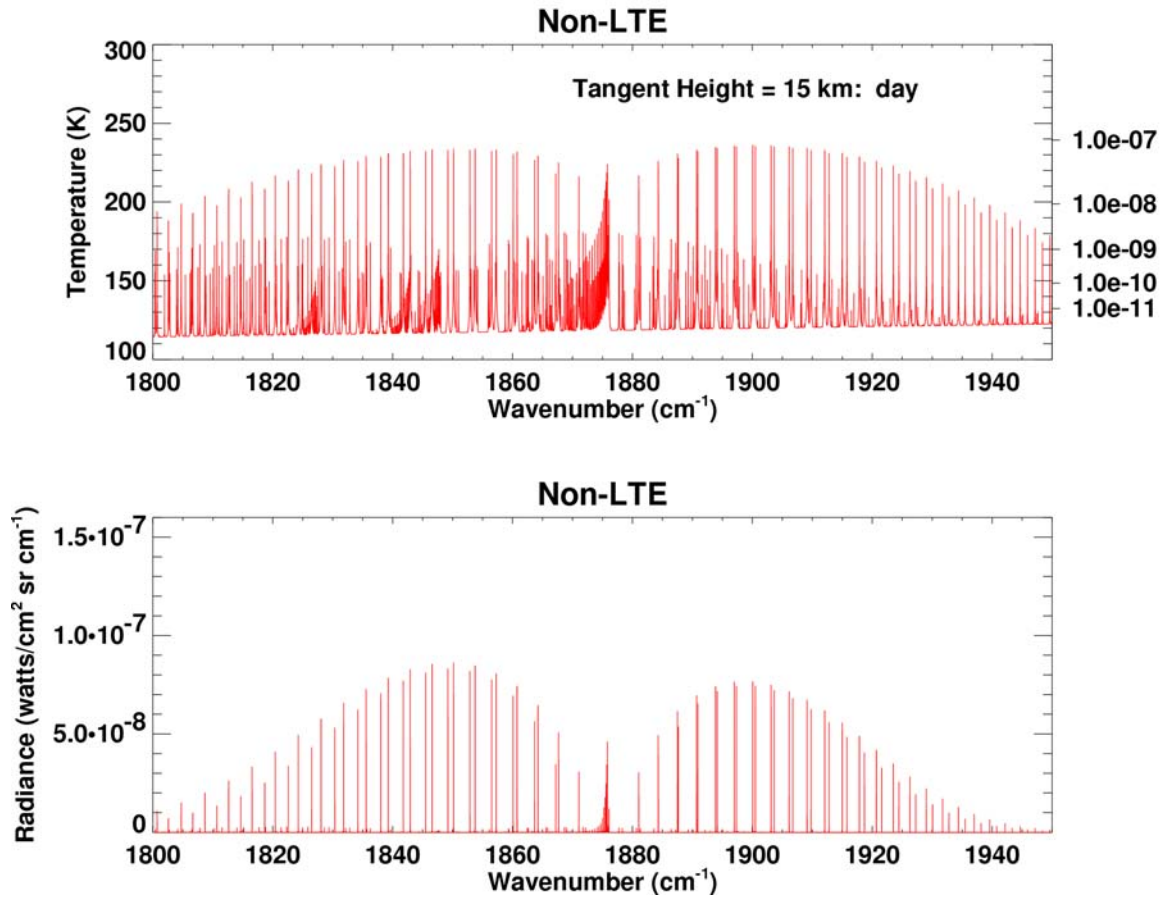
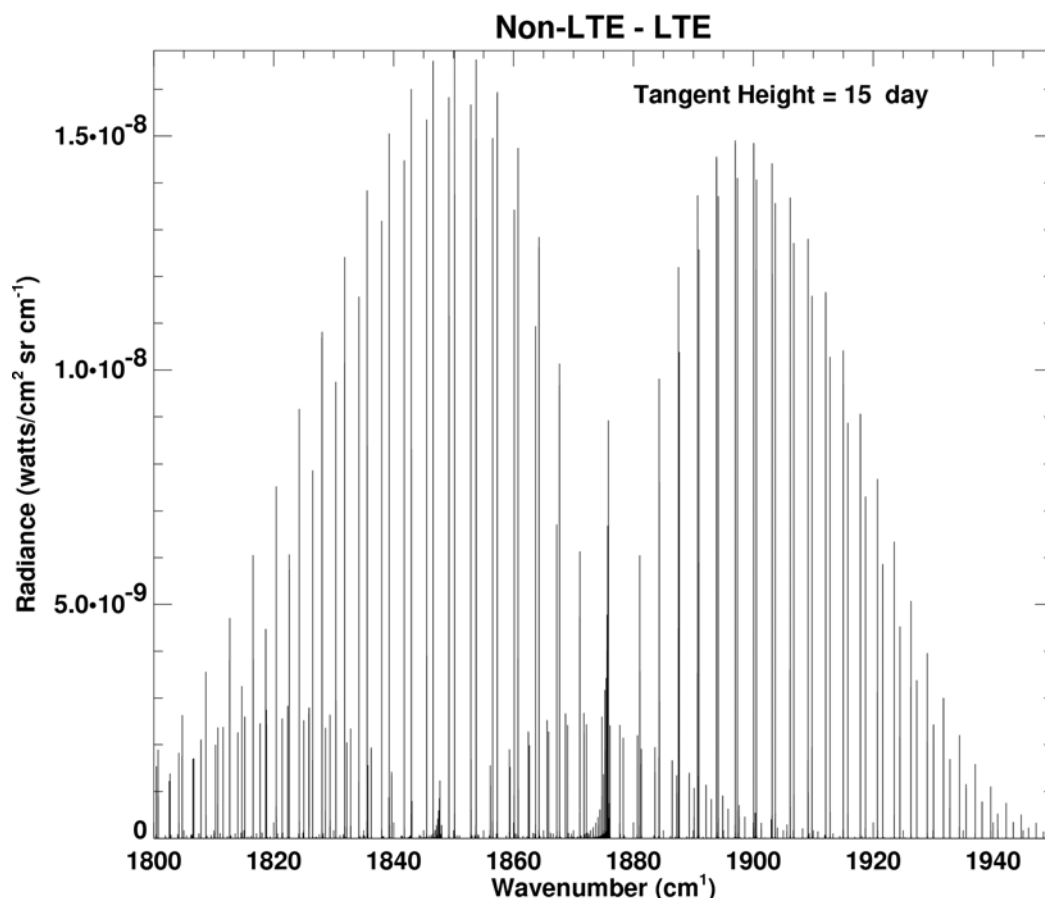


Figure A-7: Difference plot between TES LBLRTM calculated radiances under Non-LTE ( $\nu=1$ ) and LTE (kinetic temperature) conditions.



NO radiances have been computed under both LTE and Non-LTE( $\nu=1$ ) conditions for paths with tangent heights of 15 and 30 km during both day and night. Figure A-6 is the TES LBLRTM computed spectra of NO under Non-LTE daytime conditions for a tangent height of 15 km using inputs given in Figure A-3 and Figure A-5. The differences between the NO Non-LTE and LTE for this example are shown in Figure A-7 and have a maximum value of  $8.4 \times 10^{-8} \text{ W/cm}^2 \text{ sr cm}^{-1}$ . This difference corresponds to a percent maximum relative difference of  $\sim 20\%$ . These differences neglect the effect of of thermospheric rotational/spin Non-LTE. Similar calculations were performed for a tangent height of 30 km under both day and night conditions and summarized in Table A-1. This differences in radiation due to Non-LTE effects in the stratosphere and thermosphere will have a significant impact on TES tropospheric NO retrievals and will be taken into consideration in the retrieval process as outlined in Section 3.3.1.5.

**Table A-1: Summary of results for Non-LTE vs. LTE TES LBLRTM calculations.**

Day/Night	Tangent Height (km)	Maximum Non-LTE NO Radiance ( $\text{W}/\text{cm}^2 \text{ sr cm}^{-1}$ )	Non-LTE - LTE Radiance ( $\text{W}/\text{cm}^2 \text{ sr cm}^{-1}$ )	Maximum Relative Difference (%)
DAY	30	$1.27 \times 10^{-7}$	$2.65 \times 10^{-8}$	21
DAY	15	$8.4 \times 10^{-8}$	$1.7 \times 10^{-8}$	20
NIGHT	30	$8.5 \times 10^{-8}$	$9.6 \times 10^{-10}$	1.1
NIGHT	15	$5.9 \times 10^{-8}$	$8.8 \times 10^{-10}$	1.5

### A3.3.2.2: Map of Earth Surface Composition

#### **Global Land Cover Characteristics Data Base**

This appendix describes an existing source of global land cover maps with 1 km resolution and a choice of land classification schemes. This database was generated by the U.S. Geological Survey (USGS) Earth Resources Observation System (EROS) Data Center, the University of Nebraska-Lincoln (UNL) and the Joint Research Centre of the European Commission and is described in more detail at: <http://edcwww.cr.usgs.gov/landdaac/glcc/glcc.html>. Their maps are derived primarily from 1 km resolution composites of normalized difference vegetation index (NDVI) data from the Advanced Very High Resolution Radiometer (AVHRR) for the 12 month period of April 1992-March 1993. (NDVI values are the difference divided by the sum of the near infrared (channel 2) and visible (channel 1) reflectance values, after calibration and atmospheric corrections). The strategy for global land cover characterization is given in Loveland *et al* [1991, 1995] and Brown *et al* [1993] and an AVHRR data quality evaluation is described in Zhu and Yang [1996]. The global land cover maps are available in 6 different classification schemes with a range of 10 to 94 land cover types. These schemes are optimized to provide relevant information for research in areas such as atmospheric general circulation models and land use studies. Three of these classification schemes include urban/built-up areas as a land cover type, a useful distinction for our purposes. These are the Global Ecosystems classification (94 classes), Olson [1994 a&b]; the USGS Land Use/Land Cover System (24 classes), Anderson *et al* [1976]; and the International Geosphere Biosphere Programme (IGBP) Land Cover Classification (17 classes), Belward [1996]. Although we should not preclude the use of the more detailed Global Ecosystems classification, the USGS Land Use/Land Cover system (listed below) has been chosen for the initial algorithm development. The IGBP scheme, although simpler, was not chosen because there were no classes to distinguish moist vs. dry vegetation, an important distinction because of significant spectral IR reflectance differences. None of the land cover classifications in this database distinguished ice from snow, and an additional database may be needed for these areas.

**Table A-2: USGS Land Use/Land Cover System Legend and Assignment of Material Type from the ASTER Spectral Library (<http://speclib.jpl.nasa.gov/>)**

Value	Code	Description	Default material types to use for surface emissivity
1	100	Urban and Built-Up Land	construction asphalt, grass, deciduous
2	211	Dryland Cropland and Pasture	dry grass
3	212	Irrigated Cropland and Pasture	grass
4	213	Mixed Dryland/Irrigated Cropland and Pasture	grass, dry grass
5	280	Cropland/Grassland Mosaic	grass, dry grass
6	290	Cropland/Woodland Mosaic	grass, deciduous, conifer
7	311	Grassland	grass
8	321	Shrubland	deciduous
9	330	Mixed Shrubland/Grassland	deciduous, grass
10	332	Savanna	dry grass
11	411	Deciduous Broadleaf Forest	deciduous
12	412	Deciduous Needleleaf Forest	conifer
13	421	Evergreen Broadleaf Forest	conifer
14	422	Evergreen Needleleaf Forest	conifer
15	430	Mixed Forest	deciduous, conifer
16	500	Water Bodies	fresh or salt water
17	620	Herbaceous Wetland	conifer
18	610	Wooded Wetland	conifer
19	770	Barren or Sparsely Vegetated	brown gravelly sandy loam
20	820	Herbaceous Tundra	deciduous
21	810	Wooded Tundra	conifer
22	850	Mixed Tundra	deciduous, conifer
23	830	Bare Ground Tundra	dry grass
24	900	Snow or Ice	coarse granular snow

### **A3.3.3 Radiative Transfer for Clouds and Aerosols**

Aerosols and clouds (scattering materials) have the potential to impact TES measurements. This appendix will describe the overall strategy for dealing with scattering materials and refer the reader to the relevant sections in the ATBD.

The first step in dealing with scattering materials is to identify measurements that have been impacted. We will use the framework of sorting the data into cases of no clouds, broken or highly inhomogeneous clouds, optically thick clouds, and optically thin clouds. The basic strategy is to examine the brightness temperatures in the atmospheric window regions and use the values and variability of the values to classify the observations. This is discussed in detail in sections 3.5.5 and 3.5.6, pixel categorization.

Target scenes that are categorized as being free of clouds can be processed easily. If broken or highly inhomogeneous clouds are present, the target scene will be excluded from further processing. In the case of an optically thick cloud in the limb, detectors at and below the cloud will be excluded from further analysis. Light scattered into the field of view may need to be considered (see section 3.3.3.2). In nadir views, the cloud will be treated as the surface.

Cases with optically thin clouds in the nadir may be handled with gray body extinction cross sections. This is discussed in greater detail in section 3.3.3. Due to the horizontal inhomogeneity of clouds, attempting to include optically thick clouds in the limb is not recommended.

### A3.3.8.1: Line-by-Line Spectral Parameters

The line-by-line portion of the TES spectroscopic database contains transitions for individual infrared active molecular species and their isotopomers within the spectral range defined by the TES nadir and limb observations. The numbering of the species and format for the parameters are currently the same as in the HITRAN database. The HITRAN parameters are available through the internet or via an ftp site at the Smithsonian Astrophysical Observatory (<http://www.hitran.com>). The parameters and the contents of the HITRAN spectral parameters database were last reviewed for the 1996 HITRAN edition [Rothman et al., 1998]. Since that time, there have been significant improvements for some species. Here we describe the current status, updates, and known limitations of the current HITRAN parameters for the molecules and spectral regions of importance to TES. Laboratory work in progress, and published results not incorporated in HITRAN are also discussed. As was done for the ATMOS project [Brown et al., 1996], a TES spectroscopic database will be maintained to satisfy the specific needs of the TES project including all available sources (e.g. HITRAN, GEISA [Husson et al., 1999; 2000]). Status of current spectroscopy and anticipated needs proceeds on a molecule-by-molecule basis, with the description for each molecule in ascending wavenumber

#### *H<sub>2</sub>O (molecule 1)*

The significant deficiencies for water vapor on the HITRAN 1996 compilation in the thermal IR spectral region covered by TES have been greatly reduced as a result of the work of Toth (e.g. Toth [1998]). The major update includes the positions, intensities, air-broadening coefficients, self-broadening coefficients, and pressure-induced shifts and covers 500-2820 cm<sup>-1</sup>. Some transitions were found missing and were added from HITRAN 1996, so the update is not complete.

As was done for the ATMOS compilation [Brown et al., 1996], TES will treat HDO and a separate molecular species because of the large fractionation effects of HDO with respect to H<sub>2</sub>O [e.g., Moyer et al. 1996]. The current database does not include the updated positions and intensities of the HD<sup>16</sup>O v<sub>2</sub> band derived by Flaud et al. [1986] and the more recent v<sub>2</sub> HD<sup>16</sup>O,

HD<sup>17</sup>O, and HD<sup>18</sup>O position and intensity analysis results of Toth [1993]. The parameters of Flaud et al. [1986] have been regenerated (J.-M. Flaud, private communication) and are now available to the TES project with approximate air-broadened widths (C. P. Rinsland, private communication, 1998). Air-broadened pressure shifts are set to zero.

### *CO<sub>2</sub> (molecule 2)*

HITRAN infrared intensities require updating with a self-consistent calculation of energy levels including new measurements of positions, intensities, air-broadening width and air-broadened shift coefficients measured at Kitt Peak by the NASA Langley group in several spectral regions [Malathy Devi et al., 1998a,b,c] and new measurements in the 4500- to 8000 cm<sup>-1</sup> region by Miller [2001]. The 1996 HITRAN compilation parameters were based on a global least-squares fit of the energy levels of carbon dioxide [Rothman et al., 1998]. The new update should include the air-broadened pressure-shift coefficient measurements in the 10 μm laser bands, which have been demonstrated to be detectable in ground-based solar spectra [Malathy Devi et al., 1998c].

The update is of critical importance because of the use of CO<sub>2</sub> for temperature sounding by TES. Additional CO<sub>2</sub> measurements of intensities, broadening, and shift coefficients in the 4.2-4.5 μm region (<sup>12</sup>C<sup>16</sup>O<sub>2</sub>, <sup>13</sup>C<sup>16</sup>O<sub>2</sub>, and <sup>13</sup>C<sup>16</sup>O<sup>18</sup>O) and in the 10 μm laser bands are soon to be reported by the NASA Langley group (e.g. Malathy Devi et al. 2002]. The results were derived from room temperature 0.01-cm<sup>-1</sup> resolution laboratory spectra recorded at Kitt Peak. The spectroscopy of CO<sub>2</sub> in the infrared was reviewed by Malathy Devi et al. [1997].

### *O<sub>3</sub> (molecule 3)*

Simultaneous pure-rotation and 10-μm measurements of line intensities are needed to resolve the 3-4% discrepancy between measurements performed at Kitt Peak by the NASA Langley group [Smith et al., 2001] and values obtained at the Deutsches Zentrum für Luft und Raumfahrt (DLR) [Wagner et al., 2000] and at LPMA [Claveau et al., 2001]. The DLR and LPMA measurements are both lower than the Kitt Peak measurements, which are 1% higher than HITRAN 1996 [Rothman et al., 1998]. The Kitt Peak intensities agree with the current HITRAN values within experimental error. Field measurements indicate the current HITRAN values are accurate to better than 5% [Toon et al., 1999, plate 4]. If the 10-μm O<sub>3</sub> intensities are modified, the intensities in all other IR spectral regions must be scaled by the same factor to retain consistency. The DLR measurements from 16 spectra were at temperatures between 200 and 296 K and air pressures between 0.0 to 40 mbar were also analyzed to determine air-broadening coefficients, which were fitted with an empirical expansion in *m* and temperature [Wagner et al., 2000]. Those results differ significantly from values predicted by the current HITRAN compilation with important implications for the derivation of tropospheric ozone profiles from the TES nadir and limb-viewing spectra.

Updates of O<sub>3</sub> parameters on the 1996 HITRAN compilation have been summarized [Rinsland et al., 1998a]. Spectra of <sup>17</sup>O-enriched ozone samples recorded at 0.005-cm<sup>-1</sup> resolution were analyzed to derive the line positions and intensities for the *v*<sub>1</sub> and *v*<sub>3</sub> bands of <sup>16</sup>O<sup>17</sup>O<sup>16</sup>O [Heyart et al., 1992] and <sup>16</sup>O<sup>16</sup>O<sup>17</sup>O [Heyart et al., 1993]. As described by Rinsland et al. [1998a], these parameters, which were not included on HITRAN 1996 [Rothman et al., 1998] and are still not in that database. A combined list was used to identify isolated lines of the *v*<sub>3</sub> bands of <sup>16</sup>O<sup>17</sup>O<sup>16</sup>O and <sup>16</sup>O<sup>16</sup>O<sup>17</sup>O in both high resolution ground-based and balloon-borne stratospheric solar absorption

spectra. As shown in that work, they are detectable in atmospheric spectra, and hence should be added to the TES database.

Bands of O<sub>3</sub> at 4.7 μm are about one third as strong as those at 10 μm and are important absorbers in the region that will be used to retrieve CO profiles from the TES spectra. The first high-resolution analysis of the  $\nu_1 + \nu_3$  bands of <sup>16</sup>O<sup>16</sup>O<sup>18</sup>O and <sup>16</sup>O<sup>18</sup>O<sup>16</sup>O at 4.8 μm was performed by Flaud et al. [1994]. On the basis of that work, isolated lines of both heavy isotopic species were identified in high resolution ground-based solar absorption spectra by Arlander et al. [1994] and Goldman et al. [1998]. Line parameters for the  $\nu_1 + \nu_3$  bands of <sup>16</sup>O<sup>18</sup>O<sup>16</sup>O and <sup>16</sup>O<sup>16</sup>O<sup>18</sup>O [Flaud et al., 1994] and <sup>16</sup>O<sup>17</sup>O<sup>16</sup>O and <sup>16</sup>O<sup>16</sup>O<sup>17</sup>O [Perrin et al., 2001] should be added to the TES database. However, users must keep in mind that the corresponding intensities are not really accurate since they were calculated using the transition moments of the main isotopic species <sup>16</sup>O<sub>3</sub>.

Modeling of line mixing may be required for accurate simulations in Q-branch regions. As models suggest non-LTE may occur above 50 km, high vibrationally excited transitions should be added to the database, at least in the 10-μm region.

### *N<sub>2</sub>O (HITRAN molecule 4)*

Infrared measurements of positions, intensities, air-broadening coefficients and their temperature dependence, and pressure-shift coefficients obtained by Toth [2000] need to be made available to the public databases in HITRAN format. Additionally, an extensive set of line intensity measurements has been obtained from 4300-5200 cm<sup>-1</sup> [Daumont et al., 2001], and a linelist has been generated, though not in HITRAN format (J. Vander Auwera, private communication, 2001). There is good agreement with the results of Toth in regions of overlapping intensity data. Line intensities of <sup>14</sup>N<sub>2</sub><sup>16</sup>O measured in the 10-μm region agree well with those on the HITRAN 1996 [Rothman et al., 1998] and GEISA 1997 [Jacquinet-Husson et al., 1999] line-parameter compilations, except for some disagreements for the 0001-1000 and 0220-0000 bands [Daumont et al., 2001].

### *CO (HITRAN molecule 5)*

The new, self-consistent calculated set of ro-vibrational line intensities [Chackerian and Freedman, 2001] for the large range of vibrational quantum numbers need to replace current values in the public databases. This improvement is needed primarily for the intensities of the lines in the overtone bands.

### *CH<sub>4</sub> (HITRAN molecule 6)*

HITRAN contains a total replacement of the linelist for this molecule as of February 2001 with a four-fold increase in the number of lines. However, at present there is no documentation of the changes.

### *O<sub>2</sub> (HITRAN molecule 7)*

Spectroscopic parameters for both discrete electric quadrupole transitions and the pressure-induced (1-0) band exist on HITRAN 1996 [Rothman et al., 1998]. More precise measurements of the pressure-induced band (1-0) band have been reported recently by Lugez et al. [1998]. The

new results are in good agreement with the earlier less precise measurements of Orlando et al. [1991] on O<sub>2</sub> and O<sub>2</sub>/N<sub>2</sub> mixtures and Thibault et al. [1997] on pure O<sub>2</sub>.

### *NO (HITRAN molecule 8)*

As noted by Rothman et al. [1998], the total internal partition functions for NO are incorrect in the HITRAN 1996 database due to an error in the nuclear spin statistical weight factors.

### *NO<sub>2</sub> (HITRAN molecule 9)*

Progress in the analysis of NO<sub>2</sub> since the HITRAN 1996 database [Perrin et al., 1998] has been described by Perrin et al. [2000] with a focus on the 6.2 μm region, which contains the strongest band in the infrared, the ν<sub>3</sub>. The updates in that region include new measurements of positions and intensities of isotopic and hot bands. The hot band measurements may be important for modeling of non-LTE effects in the TES spectra of the upper atmosphere.

Dana et al. [1997] have reported self-, N<sub>2</sub>-, and O<sub>2</sub>-broadening coefficients of NO<sub>2</sub> lines in the ν<sub>1</sub> + ν<sub>3</sub> band at 3.4 μm. The study found a slight rotational dependence of the broadening coefficients versus N", whereas no significant dependence was observed versus K<sub>a</sub>". An empirical relation was derived to compute air-broadening coefficients at 296 K with an uncertainty of about ±10% for values of N" and K<sub>a</sub>" less than 40 and 10, respectively. The authors note that for typical lines used for atmospheric applications, the single value reported in earlier editions of the HITRAN database for all lines of all bands of NO<sub>2</sub> can differ by more than 20% from the measured values [Dana et al., 1997]. A preliminary analysis of unpublished spectra of the 1600 cm<sup>-1</sup> NO<sub>2</sub> band indicates that the widths of these lines are also too small in the previous HITRAN linelist with tests indicating that the changes produce a 10% increase in the retrieved mixing ratio of NO<sub>2</sub> at 25 km and little effect above 30 km [Sen et al., 1998]. The updated NO<sub>2</sub> parameters are available as a Sept. 2001 update from the HITRAN website.

### *HNO<sub>3</sub> (HITRAN molecule 12)*

Unpublished fits to Mark IV stratospheric balloon spectra with molecular constants derived by Toth (presented as a poster at the 2001 spectroscopic line parameters workshop in San Diego, CA) show improved fits in the region of the overlapping ν<sub>5</sub>, 2ν<sub>9</sub> bands at 11 μm. However, even if some progress were achieved recently (J.-M. Flaud, A. Perrin, and J. Orphal, private communication 2001), problems remain in simulating the narrow and very intense 885-cm<sup>-1</sup> hot band and other bands throughout the thermal IR. Retrievals from Mark IV balloon spectra indicate that the normalization of intensities in the HITRAN 2000/2001 database are inconsistent for the major bands at 5.7, 7.5, and 11 μm. Accurate and consistent absolute intensity measurements are still needed for all observable bands throughout the IR.

Perrin et al. [1998] have reanalyzed the ν<sub>8</sub> + ν<sub>9</sub> band at 1205 cm<sup>-1</sup> based on a 0.003-cm<sup>-1</sup> resolution laboratory spectrum recorded at the University of Denver. As in a recent analysis [Wang et al., 1997], the Hamiltonian for fitting the line positions takes into account the ΔK ± 2 anharmonic resonance linking the rotational levels of the ν<sub>8</sub>=1, ν<sub>9</sub>=1 "bright" vibrational state with those of the ν<sub>7</sub>=1, ν<sub>8</sub>=1 "dark" vibrational state. However, in contrast to previous work, ν<sub>8</sub> + ν<sub>9</sub> is noted to be a hybrid-type band with clearly identified B-type transitions among those of the strong A-type lines. The A- and B-type components of the transition moment operator of the ν<sub>8</sub> + ν<sub>9</sub> band were

determined through a least-squares fit of experimental line intensities measured from the spectrum. The new analysis extends the assignments for the  $\nu_8 + \nu_9$  band to maximum rotational quantum numbers of  $J=74$  and  $K_a=49$  as compared to a maximum  $J$  value of 57 [Wang et al, 1997].

### *OCS (HITRAN molecule 19).*

A recent study of high-resolution balloon-borne spectra [Goldman et al., 2000] showed that isotopic  $^{16}\text{O}^{12}\text{C}^{34}\text{S}$  lines are observable, and well as weak hot band transitions of  $\nu_3 + \nu_2 - \nu_2$  of  $^{16}\text{O}^{12}\text{C}^{32}\text{S}$ . The line positions and intensities for these bands have been already incorporated into the HITRAN database, but the air-broadening coefficients have not been updated to the level known about OCS.

### *HOCl (HITRAN molecule 21).*

The absolute intensities of lines in the  $\nu_2$  band need to be updated based on simultaneous measurements in the infrared with a tunable diode laser and the far infrared by a Fourier transform spectrometer [Vander Auwera et al., 2000].

### *HCN (HITRAN molecule 23).*

This molecule is now recognized as an important tracer of biomass burning with emissions that originate primarily in the smoldering phase of combustion [Rinsland et al. 1998b]. Positions and intensities on HITRAN were calculated more than 20 years ago. Air-broadening coefficients are taken as room-temperature  $\text{N}_2$ -broadening coefficients measured at  $0.06\text{-cm}^{-1}$  resolution over a decade ago [Smith et al., 1984]. A laboratory run at Kitt Peak in November 2001 has been completed to obtain HCN air-,  $\text{N}_2$ -, and  $\text{O}_2$ -broadening coefficients as a function of temperature for lines in the  $\nu_2$ ,  $2\nu_2$ , and  $\nu_1$  regions, which are observable with ground-based and space-borne instruments. Hot-band lines are missing in the  $\nu_1$  region on the 2001 HITRAN compilation.

### *HCOOH (HITRAN molecule 25).*

Formic acid is ubiquitous in the troposphere and an important tracer of biomass burning emissions. Spectral parameters have been generated for the  $\nu_6$  region, which contains the strongest band located in an atmospheric window [Perrin et al., 1999]. This feature is suitable for quantitative analysis based on absorption by the  $\nu_6$  band Q branch at  $1104.7\text{ cm}^{-1}$  but the feature is overlapped by a temperature-sensitive line of HDO at  $1104.87594\text{ cm}^{-1}$ , which was missing in earlier versions of HITRAN, but is now included.

### *C<sub>2</sub>H<sub>6</sub> (HITRAN molecule 27).*

Recently, assignments, improved positions, intensities, and air-broadening coefficients and their temperature dependence have been derived for the strong and sharp  $^{\text{P}}\text{Q}_3$  subbranch of the  $\nu_7$  band at  $2976.8\text{ cm}^{-1}$  [Pine and Stone; 1996; Rinsland et al., 1998c; Pine and Rinsland, 1998]. This strong and sharp feature is prominent in ground-based solar spectra [Rinsland et al., 1987; Rinsland et al., 1998c] and nearly free of atmospheric interferences. The new results were obtained from analysis of Doppler-limited and sub-Doppler molecular beam laboratory spectra. It may be possible to measure this  $\text{C}_2\text{H}_6$  feature in the TES nadir view spectra. Also, it should be noted that the TIPS program provided on the 1996 HITRAN CD ROM does not compute the  $\text{C}_2\text{H}_6$  total internal partition function correctly.

### *COF<sub>2</sub> (molecule 29)*

Line assignments in the  $\nu_1$  band at  $1943\text{ cm}^{-1}$  are incorrect (J.-M. Flaud, private communications, 2001) and have to be fixed.

### *ClONO<sub>2</sub> (HITRAN molecule 35).*

Current HITRAN absorption cross sections for the region of the  $\nu_4$  band Q branch at  $780.2\text{ cm}^{-1}$  should be replaced by temperature- and pressure-dependent  $0.0009\text{--}0.008\text{ cm}^{-1}$  resolution laboratory spectra measured between 190 and 296 K and 0.3 to 1.0 mbar measured by Birk and Wagner [2000]. Nearly 30 of these laboratory spectra have been analyzed with the JPL GFIT algorithm to generate the set of ClONO<sub>2</sub> “pseudolines” by simultaneously fitting transmission spectra produced from the laboratory absorption coefficient. Retrievals with the Mark IV spectra indicate a more consistent estimation of the stratospheric chlorine budget than earlier sets of parameters (G. C. Toon, private communication, 2001). A spectroscopic analysis of these bands is in progress and, if successful and validated, should be used in the future [Flaud et al., 2001b]. Additional measurements of low temperature absorption cross-sections are needed for the strong  $1700\text{-cm}^{-1}$  band.

### Additional species

#### *COClF (no HITRAN molecule number).*

At present, no parameters exist on the HITRAN database for this molecule, which possibly could be detected in lower stratospheric tropical regions from measurements of its  $\nu_1$  band near  $1800\text{ cm}^{-1}$ .

#### *COCl<sub>2</sub> (no HITRAN molecule number).*

The  $\nu_5$  band in the  $830\text{--}860\text{-cm}^{-1}$  region was recently reported from balloon-borne solar occultation spectra. This identification and the occurrence of the strong  $\nu_1$  band centered at  $1827\text{ cm}^{-1}$  [Toon et al., 2001] and the availability of limited spectroscopic parameters in both regions indicate a need for further studies to improve quantitative analysis for both bands.

#### *CH<sub>3</sub>OH (no HITRAN molecule number).*

The  $1033\text{-cm}^{-1}$  CO-stretch  $\nu_8$  band of ethanol is a prominent feature in spectra of biomass burning plumes (e.g. Worden et al., [1997]). Spectral features of this band are likely to be an important interference in retrievals of O<sub>3</sub> from TES spectra recorded under such conditions. To our knowledge, no line-by-line parameters are available for this band, though progress is being made on the analysis of all the IR bands [Xu and Lees, 2000].

### *IR Cross-Sections*

The HITRAN compilation includes infrared absorption cross sections for molecules that cannot be reliably modelled by line-by-line methods. They are C<sub>2</sub>F<sub>6</sub>, CCl<sub>4</sub>, CFC-11, CFC-113, CFC-114, CFC-115, CFC-12, CFC-13, CFC-14, ClONO<sub>2</sub>, HFC-123, HFC-124, HFC-141B, HFC-142B, HCFC-21, HCFC-22, HCFC-225, HFC-125, HFC-134, HFC-134a, HFC-143a, HFC-152a,

HFC-34, HNO<sub>4</sub>, N<sub>2</sub>O<sub>5</sub>, and SF<sub>6</sub>. Some species are included both as line-by-line and absorption cross section files on HITRAN, so care is required to avoid duplication.

### *Partition Functions*

It is important to note that the partition functions supplied by HITRAN have several significant deficiencies as discussed by Goldman *et al.* [1998].

A3.3.8.2: Cross-Section P-T Interpolation Program XSFINT

**1. P-T Point outside table of temperature-pressure values**

In this case the "distance" away from every point in the table is calculated and compared to find the closest point. The distance calculation is based on linear distance formulas where the pressure is divided by 10 to give similar units in temperature and pressure.

**2. P-T Point inside table of temperature-pressure values**

This program picks points based on temperature lines where all temperatures within 2 degrees are considered to be on the same temperature line. A temperature line could look like

Temperature	Pressure
216	50.6
214.1	70.8
215.8	100.0

A table of pressures on temperature lines is constructed from which to pick points. There are four basic cases in the interpolate point outside table of temperature values; four points around target; three points around target; two points around target. The new cross-section records interpolated from the above cases are all written to a new cross-section file. The user can also select the points and interpolation method by hand rather than letting the program select the points and interpolation method.

**Four points around target**

In this case 2 points on the temperature line before and after the target temperature are found where the points surround the target pressure.

216.6,70.5	217.1,90.2 (temp line after)
210.0,80.0 (target point)	
200.1,69.9	201.0,89.9 (temp line before)

The corner pressures must be within 10% of each other (216.6,70.5 with 200.1,69.9 & 217.1,90.2 with 201.0,89.9) or the tightest diagonal line is picked and the 2 point temperature interpolate is activated, otherwise the 4 point interpolate is activated.

**Three points around target**

In this case either the temperature line above or below the target contains only one point.

216.6,70.5	217.1,90.2 (temp line after)
210.0,80.0 (target point)	
200.1,69.9	(temp line before)

or

216.6,70.5    217.1,90.2 (temp line after)  
210.0,80.0 (target point)  
201.0,89.9    (temp line before)

If the target temperature is within 5 degrees of the temperature line with 2 points, then a 2 point pressure interpolate is activated between those two points. If the target temperature is not close enough to the temperature line with two points, then two points are chosen that create a diagonal (200.1,69.9 with 217.1,90.2 or 216.6,70.5 with 201.0,89.9) then the two point temperature interpolate is activated.

### **Two points around target**

In this case one point on the temperature line before and after the target are used. If both points are either greater or smaller in pressure than the target, then the closest in pressure is used as the new point. If one of the two points are within 4% in temperature and 15% in pressure of the target, then that point is used as new point. If both points are within the 4% and 15% then the closest in temperature is used. If none of the above special cases occur then the 2 point temperature interpolate is activated.

### **Two point Temperature Interpolate**

Two point temperature interpolate does a linear interpolate in temperature between the two pressure/temperature cross-section points for each point in the cross-sections.

### **Two point Pressure Interpolate**

Two point pressure interpolate does a log interpolate in pressure between the two pressure/temperature cross-section points for each point in the cross-sections. (Note In the code the two point pressure interpolate is noted as a 3 point interpolate since two point temperature interpolate is noted as a 2 point interpolate)

### **Four point Interpolate**

Four point interpolate does a linear interpolate in temperature between the side pressure/temperature cross-section points, then a log interpolate in pressure between the two new temperature points resulting from the linear temperature interpolate.

### **XSFINT Source Code**

Xsfint has been compiled and tested on roma in /home/goldman/xsctions/interp. The source code for xsfint is all in one FORTRAN90 file called xsfint.F90. It contains two modules and one main code. The main code is at the end of the file, and must be there for it to use the two modules. The program has code to create plots using NCAR GKS graphics. The graphics code is currently disabled using conditional compilation with #define, #ifdef, #endif. All sections of graphics code are bracketed in #ifdef NCARGKSOUTPUT, #endif NCARGKSOUTPUT. The first line in the source code has a comment line

```
!#define NCARGKSOUTPUT
```

Uncommenting this line, (removing the "!"), activates the graphics code. The source file is named with .F90 instead of .f90 to activate the pre-processor that processes the NCARGKSOUTPUT lines. To compile xsfint, activate f90 as follows

```
f90 -o xsfint xsfint.F90
```

### XSFINT Input

The input file format is as follows

line1 -input cross-section filename

line 2 -output cross-section filename

line 3 -target temperature target pressure interpolate select  
interpolate select

0 = Automatic pick of points to interpolate and interpolate method

1 = Use the temperature, pressure shown on line 4 to select a record from the cross-section file as the new point. (manual pick nearest point)

2 = Use the temperature, pressure shown on line 4 and 5 to select 2 records from the cross-section file to do a two point temperature interpolate on.

3 = Use the temperature, pressure shown on line 4 and 5 to select 2 records from the cross-section file to do a two point pressure interpolate on.

4 = Use the temperature, pressure shown on line 4, 5, 6 and 7 to select 4 records from the cross-section file to do a four point interpolate on.

Lines to specify manual selections contain  
temperature pressure

There can be multiple target points selected in a run, each possibly with different interpolation selectors.

There is an example case on roma in /home/goldman/xsctions/interp and is named cfc22.test.input. It contains

```
../cfc22.xsect (cross-section file to read)
cfc22.test.output (cross-section file to create)
220.0 50.0 3 (target 220.0,50.0 manual select points)
216.0 176.8 (point 1 for 2 point pressure interp)
216.0 40.9 (point 2 for 2 point pressure interp)
240.0 300.0 0 (target 240.,300. auto select points & interp)
226.0 223.0 2 (target 226.0, 223.0 manual select points)
237.0 270.4 (point 1 for 2 point temperature interp)
216.0 176.8 (point 2 for 2 point temperature interp)
```

### Running XSFINT

To run xsfint on the test case on roma type

```
xsfint <cfc22.test.input >& cfc22.test.output
```

This reads cfc22.test.input and creates cfc22.new.xsect and cfc22.test.output.

### List of files

All files are on ms are in /GOLDMAN/VARANAS/XSEC.JUNE.97 except where noted otherwise.

#### CCL4

Xsection file - ccl4.tar  
Resolution -  $0.03 \text{ cm}^{-1}$   
Fixed  $0.0025 \text{ cm}^{-1}$  Spc file -ccl4.xsect.25  
Avg Spc file - ccl4.xsect.avgspc  
Table - table.ME0216 in goldman output subdirectory  
Number of Files 32  
Wavenumber range  $750.0100\text{-}811.9900 \text{ cm}^{-1}$

#### CFC11

Xsection file - cfc11.tar  
Resolution -  $0.01, 0.03 \text{ cm}^{-1}$   
Fixed  $0.0025 \text{ cm}^{-1}$  Spc file -cfc11.xsect.A.25  
cfc11.xsect.B.25  
Avg Spc file - cfc11.xsect.avgspc.A  
cfc11.xsect.avgspc.B  
Table - table.ME0131 (part a) in goldman output subdirectory  
table.ME7904 (part b) in goldman output subdirectory  
Number of Files 55  
Wavenumber range  $810.0060\text{-}879.9930 \text{ cm}^{-1}$   
 $1050.0000\text{-}1119.9930 \text{ cm}^{-1}$

#### CFC12

Xsection file - cfc12.tar  
Resolution -  $0.01, 0.02, 0.03 \text{ cm}^{-1}$   
Fixed  $0.0025 \text{ cm}^{-1}$  Spc file -cfc12.xsect.A.25  
cfc12.xsect.B.25  
Avg Spc file - cfc12.xsect.avgspc.A  
cfc12.xsect.avgspc.B  
Table - table.ME8745 (part a) in goldman output subdirectory  
table.ME6165 (part b) in goldman output subdirectory  
Number of Files 51  
Wavenumber range  $850.0050\text{-}949.9950 \text{ cm}^{-1}$   
 $1050.0060\text{-}1199.9850 \text{ cm}^{-1}$

#### CFC22

Xsection file - cfc22.tar  
Resolution -  $0.03 \text{ cm}^{-1}$   
Fixed  $0.0025 \text{ cm}^{-1}$  Spc file -cfc22.xsect.25

Avg Spc file - cfc22.xsect.avgspc  
 Table - table.ME0088 in goldman output subdirectory  
 Number of Files 7  
 Wavenumber range 760.0300-860.000 cm<sup>-1</sup>

SF6

Xsection file - sf6.tar  
                     Resolution - 0.03 cm<sup>-1</sup>  
 Fixed 0.0025 cm<sup>-1</sup> Spc file -sf6.xsect.25  
 Avg Spc file - sf6.xsect.avgspc  
 Table - table.ME0112 in goldman output subdirectory  
 Number of Files 7  
 Wavenumber range 925.0100-955.000 cm<sup>-1</sup>

CF4

Xsection file - cfc14.tar  
                     Resolution - 0.01, 0.03 cm<sup>-1</sup>  
 Fixed 0.0025 cm<sup>-1</sup> Spc file -cfc14.xsect  
 Avg Spc file - cfc14.xsect.avgspc  
 Table - table.ME0132 in goldman output subdirectory  
 Number of Files 54  
 Wavenumber range 1250.0050-1289.9975 cm<sup>-1</sup>

**A3.4: Analytic Jacobians**

The radiance at the satellite in terms of component contributions from the atmosphere and the surface, but neglecting the solar contribution may be written as

$$L_{sat} = L_L^\uparrow + (\epsilon B(T_{sfc}) + \alpha L_0^\downarrow) \mathcal{T}_{0,L} \quad (A.53)$$

where  $L_L^\uparrow$  is the upwelling radiance contribution of the atmosphere from the surface to the level at the top of the atmosphere (TOA),  $\mathcal{T}_{0,L}$  is the transmittance of the atmosphere and  $L_0^\downarrow$  is the downwelling radiance at the surface. For a specularly reflecting surface,  $L_0^\downarrow$  is calculated for the same zenith angle as  $L_L^\uparrow$  and  $\alpha$  is the appropriate bi-directional reflectance. For a Lambertian surface,  $L_0^\downarrow$  is calculated at the diffusivity angle, the downwelling radiation scattered by the surface is taken to be isotropic and  $\alpha$  is the albedo.

Due to the form of the radiative transfer equation (equation 3.8), the analytic derivative of the radiance at the satellite with a change in parameter  $x_l$  at level  $l$ , is most expeditiously obtained in terms of associated layer quantities, so that we have

$$\frac{\partial L_{sat}}{\partial x_l} = \sum_j \frac{\partial L_{sat}}{\partial \bar{x}_j} \frac{\partial \bar{x}_j}{\partial x_l} \quad (\text{A.54})$$

in which  $x_l$  is an element of the retrieval vector associated with level  $l$  and  $\bar{x}_j$  is the associated layer quantity for layer  $j$ . Note that in general,  $x$  may be mixing ratio (log mixing ratio) or temperature in this context.

For the layer quantities, it is useful to separate the jacobian calculation into partial derivatives with respect to layer total optical depth ( $\tau_l$ ) and Planck function ( $B_l$ ) via the chain rule. Differentiating Equation (A.54), we obtain

$$\frac{\partial L_{sat}}{\partial x_l} = \frac{\partial L_{sat}}{\partial \tau_l} \frac{\partial \tau_l}{\partial x_l} \quad (\text{A.55})$$

for gas species, and

$$\frac{\partial L_{sat}}{\partial T_l} = \frac{\partial L_{sat}}{\partial \tau_l} \frac{\partial \tau_l}{\partial T_l} + \frac{\partial L_{sat}}{\partial B_l} \frac{\partial B_l}{\partial T_l} \quad (\text{A.56})$$

for layer temperature  $T_l$ .

The next 5 sections of this appendix give (abbreviated) derivations for each of the terms in equations (A.55) and (A.56). This is followed by section A3.4.6, which gives the layer-to-level partials used in equation (A.54), section A3.4.7 where analytic pointing jacobians are derived and finally section A3.4.8 with results of analytic jacobian validation using finite difference jacobian calculations.

### A3.4.1 Partial with respect to layer optical depth (OD) $\frac{\partial L_{sat}}{\partial \tau_l}$

Differentiating (A.53), we obtain

$$\frac{\partial L_{sat}}{\partial \tau_l} = \frac{\partial L_L^\uparrow}{\partial \tau_l} + \alpha \frac{\partial L_0^\downarrow}{\partial \tau_l} \mathcal{T}_{0,L} + \left( \varepsilon B(T_{sfc}) + \alpha L_0^\downarrow \right) \frac{\partial \mathcal{T}_{0,L}}{\partial \tau_l} \quad (\text{A.57})$$

Since

$$\mathcal{T}_{0,L} = \prod_{k=0}^L e^{-\tau_k}, \quad \frac{\partial \mathcal{T}_{0,L}}{\partial \tau_l} = -e^{-\tau_l} \prod_{k \neq l} e^{-\tau_k} \Rightarrow \frac{\partial \mathcal{T}_{0,L}}{\partial \tau_l} = -\mathcal{T}_{0,L} \quad (\text{A.58})$$

equation (A.57) becomes

$$\frac{\partial L_{sat}}{\partial \tau_l} = \frac{\partial L_L^\uparrow}{\partial \tau_l} + \left[ \alpha \frac{\partial L_0^\downarrow}{\partial \tau_l} - \left( \varepsilon B(T_{sfc}) + \alpha L_0^\downarrow \right) \right] \mathcal{T}_{0,L} \quad (\text{A.59})$$

where  $\varepsilon=0$  and  $\alpha=1$  for limb calculations. We now need to evaluate the separate upwelling and downwelling terms.

A3.4.1.1 Downwelling OD partials  $\frac{\partial L_0^\downarrow}{\partial \tau_l}$

For any layer  $l$ , the downwelling radiance at the corresponding level  $l$  is given by

$$L_l^\downarrow = L_{l+1}^\downarrow \mathcal{T}_l + B(\overline{T}_l)(1 - \mathcal{T}_l) \quad (\text{A.60})$$

Where  $L_{l=L}^\downarrow$  is initialized to zero radiance for the top of the atmosphere. Differentiating equation (A.60) we have

$$\frac{\partial L_l^\downarrow}{\partial \tau_l} = (B(\overline{T}_l) - L_{l+1}^\downarrow) \mathcal{T}_l \quad (\text{A.61})$$

At any stage in the recursive calculation, we can write the downwelling radiance at level 0,  $L_0^\downarrow$ , as the sum of two terms:

$$L_0^\downarrow = L_l^\downarrow \mathcal{T}_{l,0} + L_{l,0}^\downarrow \quad (\text{A.62})$$

*i.e.*, the downwelling radiance down to level  $l$  attenuated by the transmission from level  $l$  to level 0 plus the radiance contribution between levels  $l$  and 0, (see Figure A-8: Layer and level view for downwelling OD jacobian calculation). Thus

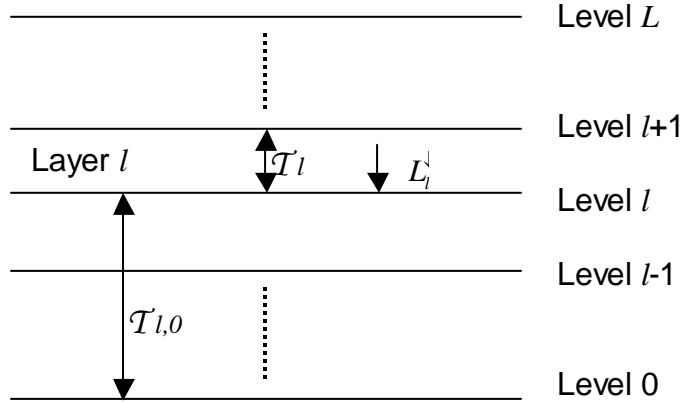
$$\frac{\partial L_0^\downarrow}{\partial \tau_l} = (B(\overline{T}_l) - L_{l+1}^\downarrow) \mathcal{T}_{l+1,0} \quad (\text{A.63})$$

A3.4.1.2 Upwelling OD partials  $\frac{\partial L_L^\uparrow}{\partial \tau_l}$

We can write the upwelling radiance in terms of layer  $l$  as

$$L_L^\uparrow = \left[ L_l^\uparrow \mathcal{T}_l + B_{\text{eff}}(\overline{T}_l, T_{l+1}, \tau_l)(1 - \mathcal{T}_l) \right] \mathcal{T}_{l+1,L} + L_{l+1,L}^\uparrow \quad (\text{A.64})$$

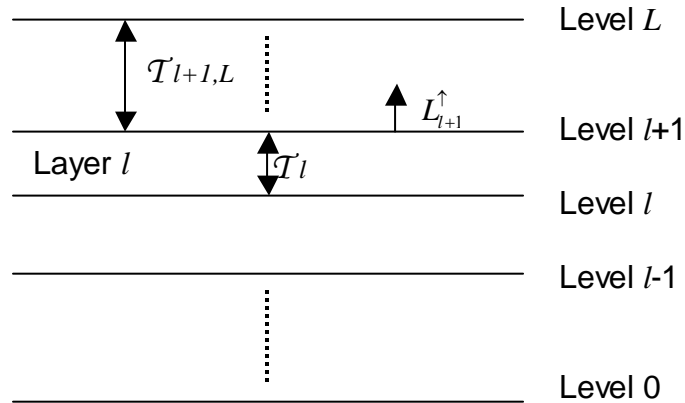
Figure A-8: Layer and level view for downwelling OD jacobian calculation



When  $L_{l=0}^\uparrow$  is initialized to the surface term:  $L_0^\uparrow = \varepsilon B(T_{sfc}) + \alpha L_0^\downarrow$  for nadir and to the “backside” or downwelling term:  $L_0^\uparrow = L_0^\downarrow$  for limb, equation (A.64) becomes the total radiance at the satellite,  $L_{sat}$ , as given in equation (A.53). For the upwelling radiative transfer, we apply the linear-in-tau approximation described in section 3.3.1.4. Differentiating equation (A.64) gives

$$\frac{\partial L_L^\uparrow}{\partial \tau_l} = \left( B_{eff}(\bar{T}_l, T_{l+1}, \tau_l) - L_l^\uparrow \right) \mathcal{T}_{l,L} + \frac{\partial B_{eff}}{\partial \tau_l} (1 - \mathcal{T}_l) \mathcal{T}_{l+1,L} \quad (\text{A.65})$$

Figure A-9: Layer and level view for upwelling OD jacobian calculation



Since  $B_{eff}(\bar{T}_l, T_{l+1}, \tau_l) = B(\bar{T}_l) + \beta(\bar{T}_l, T_{l+1})F(\tau_l)$  where  $\beta(\bar{T}_l, T_{l+1}) = B(T_{l+1}) - B(\bar{T}_l)$  and  $F(\tau_l) = 1 - 2 \left[ \frac{1}{\tau_l} + \frac{\tau_l}{1 - \tau_l} \right]$ ; (with  $F(\tau_l) = \frac{\tau_l}{6}$  for small values of  $\tau_l$ ), we have

$$\frac{\partial B_{eff}}{\partial \tau_l} = \beta \frac{\partial F}{\partial \tau_l} \quad (\text{A.66})$$

where  $\frac{\partial F}{\partial \tau_l} = \frac{2}{\tau_l^2} - \frac{2\tau_l}{(1 - \tau_l)^2}$ ; (with  $\frac{\partial F}{\partial \tau_l} = \frac{1}{6}$  for small  $\tau_l$ ) is pre-computed and tabulated in the same way as  $F(\tau_l)$ .

Combining the downwelling and upwelling terms, equation (A.59) becomes:

$$\frac{\partial L_{sat}}{\partial \tau_l} = \left( B_{eff}(\bar{T}_l, T_{l+1}, \tau_l) - L_l^\uparrow \right) \mathcal{T}_{l,L} + \beta(\bar{T}_l, T_{l+1}) \frac{\partial F}{\partial \tau_l} (1 - \tau_l) \mathcal{T}_{l+1,L} + \alpha \left( B(\bar{T}_l) - L_{l+1}^\downarrow \right) \mathcal{T}_{l+1,0} \mathcal{T}_{0,L} \quad (\text{A.67})$$

Note that the term  $-\left( \varepsilon B(T_{sfc}) + \alpha L_0^\downarrow \right) \mathcal{T}_{0,L}$  in equation (A.59) is accounted for since the upwelling radiance is initialized with  $L_{l=0}^\uparrow = \varepsilon B(T_{sfc}) + \alpha L_0^\downarrow$ , for nadir, ( $\varepsilon=0$ ,  $\alpha=1$  for limb).

### A3.4.2 Partial of optical depth with respect to gas species VMR $\frac{\partial \tau_l}{\partial x_l}$

The layer optical depth is given by

$$\tau_l = \sum_m u_{l,m} \kappa_{l,m} = u_l \sum_m \kappa_{l,m} \bar{q}_{l,m} = u_l \kappa_l \quad (\text{A.68})$$

where  $u_{l,m}$  is the integrated path amount in layer  $l$  for species  $m$ ,  $\kappa_{l,m}$  is the absorption coefficient and  $\bar{q}_{l,m} = u_{l,m} / u_l$  is the layer average volume mixing ratio (VMR). For  $m \neq 1$ , i.e., all species except H<sub>2</sub>O,

$$\frac{\partial \tau_l}{\partial q_{l,m}} = u_l \kappa_{l,m} \quad \text{or} \quad \frac{\partial \tau_l}{\partial \ln \bar{q}_{l,m}} = \bar{q}_{l,m} u_l \kappa_{l,m} = \tau_{l,m} \quad (\text{A.69})$$

We then have the simple result that the optical depth (OD) partial with respect to log VMR is simply the species optical depth.

A3.4.2.1 Partial derivatives of optical depth with respect to H<sub>2</sub>O VMR  $\frac{\partial \tau_l}{\partial \bar{q}_{l,m=1}}$

For H<sub>2</sub>O ( $m=1$ ), we cannot neglect the dependence of H<sub>2</sub>O VMR on self-broadening for absorption coefficients  $\left(\frac{\partial \kappa_{l,1}}{\partial \bar{q}_{l,1}}\right)$  or the integrated path amount  $\left(\frac{\partial u_l}{\partial \bar{q}_{l,1}}\right)$  and we must separate the absorption ( $\kappa_{l,1}$ ) into both line ( $\kappa^{line}$ ) and continuum ( $\kappa^{cont}$ ) contributions. Including all these terms, we have

$$\frac{\partial \tau_l}{\partial \ln \bar{q}_{l,1}} = \tau_{l,1} + \tau_{l,1}^{line} \frac{\partial \ln \kappa_{l,1}^{line}}{\partial \ln \bar{q}_{l,1}} + \tau_{l,1}^{cont} \frac{\partial \ln \kappa_{l,1}^{cont}}{\partial \ln \bar{q}_{l,1}} + \tau_l \frac{\partial \ln u_l}{\partial \ln \bar{q}_{l,1}} \quad (A.70)$$

Thus H<sub>2</sub>O VMR jacobians have three additional terms that are computed, compared to the other gas species VMR jacobians. These terms are described in the following sub-sections.

A3.4.2.1.1 H<sub>2</sub>O line self-broadening dependence  $\tau_{l,1}^{line} \frac{\partial \ln \kappa_{l,1}^{line}}{\partial \ln \bar{q}_{l,1}}$

We account for the self-broadening of H<sub>2</sub>O absorption lines by tabulating two sets of absorption coefficients,  $\kappa^{wet}$  and  $\kappa^{dry}$ , for pressures > 100 mb. Line absorption for H<sub>2</sub>O is then given by

$$\kappa_{l,1}^{line} = \kappa_l^{dry} + \left( \frac{\kappa_l^{wet} - \kappa_l^{dry}}{q_l^{wet} - q^{dry}} \right) (\bar{q}_{l,1} - q^{dry}) \quad (A.71)$$

where  $q_l^{wet}$  is 90% of saturation vmr for the layer and  $q^{dry}$  is 1.0e-08 (layer independent). We then have

$$\tau_{l,1}^{line} \frac{\partial \ln \kappa_{l,1}^{line}}{\partial \ln \bar{q}_{l,1}} = \bar{q}_{l,1} u_{l,1} \left( \frac{\kappa_l^{wet} - \kappa_l^{dry}}{q_l^{wet} - q^{dry}} \right) \quad (A.72)$$

A3.4.2.1.2 H<sub>2</sub>O continuum dependence  $\tau_{l,1}^{cont} \frac{\partial \ln \kappa_{l,1}^{cont}}{\partial \ln \bar{q}_{l,1}}$

From equation 3.27, the absorption coefficient for water vapor continuum is given by:

$$\kappa_{l,1}^{cont} = \nu \tanh\left(\frac{h\nu}{2k_B T_l}\right) \left[ \frac{\bar{P}_l \bar{T}_o}{\bar{P}_o \bar{T}_l} \right] \left( \bar{q}_{l,1} C_s (\bar{T}_l) + (1 - \bar{q}_{l,1}) C_f \right) \quad (A.73)$$

where  $C_s$  and  $C_f$  are the self and foreign broadened coefficients, respectively. We then have:

$$\tau_{l,1}^{cont} \frac{\partial \ln \kappa_{l,1}^{cont}}{\partial \ln \bar{q}_{l,1}} = u_{l,1} \kappa_{l,1}^{cont} \left( \frac{\bar{q}_{l,1} (C_s - C_f)}{\bar{q}_{l,1} C_s + (1 - \bar{q}_{l,1}) C_f} \right) \quad (A.74)$$

**A3.4.2.1.3 Layer integrated path amount dependence on H<sub>2</sub>O VMR**  $\tau_l \frac{\partial \ln u_l}{\partial \ln q_{l,1}}$

Because water vapor at altitudes below 100mb is abundant enough to affect the integrated path amount through those layers, we account for this dependence in the H<sub>2</sub>O VMR jacobians. For nadir and most limb layers (all but the tangent and next to tangent layers), we can assume a straight path through the layer, *i.e.*, refraction can be neglected over the layer height. In these cases, we can write

$$g(M_{dry} u_l + M_{H_2O} \bar{q}_{l,1} u_l) = c \Delta p = \text{constant} \quad (\text{A.75})$$

since we have a fixed pressure grid with  $\Delta p$  and we can assume gravitational acceleration,  $g$ , is constant over the layer.  $M_{dry}$  and  $M_{H_2O}$  are the molecular weights of dry air and water respectively. The constant  $c$  is the geometric correction for any straight path with respect to vertical ( $c=1$  for a vertical path). Differentiating this expression gives

$$\frac{\partial \ln u_l}{\partial \ln \bar{q}_{l,1}} = \frac{-1}{1 + \left( \frac{M_{dry}}{\bar{q}_{l,1} M_{H_2O}} \right)} \quad (\text{A.76})$$

where  $\frac{M_{dry}}{M_{H_2O}} = \frac{28.96}{18} = 1.609$ . In general, the contribution from this term is small (<1%) compared to the other corrections for H<sub>2</sub>O VMR jacobians.

The values of equation (A.76) have been compared to finite difference calculations with the ray-tracing code. For nadir and non-tangent layers for limb, the differences between this expression and the finite difference calculations are at most 3%. For limb tangent layers, the differences are around 30%. However, the effects of this correction are further reduced since it is subsequently multiplied by total transmission, which will be small in the limb case for layers near the surface where this correction is largest, due to water vapor continuum. Since we do not detect significant differences in the overall comparison of analytic to finite difference for limb H<sub>2</sub>O VMR jacobians due to the presence or absence of this term, we are not planning to modify the calculation in the limb tangent layers at this time.

**A3.4.3 Partial with respect to layer Planck (or effective Planck) function**  $\frac{\partial L_{sat}}{\partial B_l}$

Differentiating (A.53), we obtain

$$\frac{\partial L_{sat}}{\partial B_l} = \frac{\partial L_l^\uparrow}{\partial B_l} + \alpha \frac{\partial L_0^\downarrow}{\partial B_l} \mathcal{T}_{0,L} \quad (\text{A.77})$$

**Downwelling term**

Following equation (A.62),  $L_0^\downarrow = [L_{l+1}^\downarrow \mathcal{T}_l + B_l (1 - \mathcal{T}_l)] \mathcal{T}_{l,0} + L_{l,0}^\downarrow$  and

$$\frac{\partial L_0^\downarrow}{\partial B_l} = (1 - \tau_l) \mathcal{T}_{l,0} \quad (\text{A.78})$$

### Upwelling term

From equation (A.64),  $L_L^\uparrow = [L_l^\uparrow \tau_l + B_l^{\text{eff}} (1 - \tau_l)] \mathcal{T}_{l+1,L} + L_{l+1,L}^\uparrow$  and

$$\frac{\partial L_L^\uparrow}{\partial B_l^{\text{eff}}} = (1 - \tau_l) \mathcal{T}_{l+1,L} \quad (\text{A.79})$$

where  $B_l^{\text{eff}}$  is the layer effective Planck function for upwelling radiance calculations, assuming the linear-in-tau approximation, as discussed in section 3.3.1.4.

### A3.4.4 Partial derivatives of layer Planck (or effective Planck) function with respect to temperature

$$\frac{\partial B_l}{\partial T_l}$$

The Planck function (in  $\text{W/m}^2/\text{sr/cm}^{-1}$ ) is given by  $B_l = \frac{2hc^2\nu^3}{\exp\left(\frac{hc\nu}{k_B\bar{T}_l}\right) - 1}$  with partial:

$$\frac{\partial B_l}{\partial \bar{T}_l} = \frac{B_l^2 \exp\left(\frac{hc\nu}{k_B\bar{T}_l}\right)}{2c\nu^2 k_B \bar{T}_l^2} \quad (\text{A.80})$$

For the effective Planck function  $B_l^{\text{eff}} = B_l + \beta(\bar{T}_l, T_{l+1})F(\tau_l)$  with  $\beta = B(T_{l+1}) - B(\bar{T}_l)$ , (see equation (A.66) for  $F(\tau_l)$ ), we have

$$\frac{\partial B_l^{\text{eff}}}{\partial \bar{T}_l} = \frac{\partial B_l}{\partial \bar{T}_l} + F(\tau_l) \left[ \frac{\partial B}{\partial T_{l+1}} \frac{\partial T_{l+1}}{\partial \bar{T}_l} - \frac{\partial B_l}{\partial \bar{T}_l} \right] \quad (\text{A.81})$$

where  $\frac{\partial T_{l+1}}{\partial \bar{T}_l}$  is the inverse layer-to-level partial for temperature given in section A3.4.6, with  $T_{l+1} = T_U$ , i.e., the temperature at the upper level of layer  $l$ .

### A3.4.5 Partial derivatives of optical depth with respect to temperature $\frac{\partial \tau_l}{\partial \bar{T}_l}$

Accounting directly for both line and continuum absorption, equation (A.68) becomes

$$\tau_l = \sum_m u_{l,m} (\kappa_{l,m}^{\text{line}} + \kappa_{l,m}^{\text{cont}}) \quad (\text{A.82})$$

with

$$\frac{\partial \tau_l}{\partial \bar{T}_l} = \sum_m u_{l,m} \left( \frac{\partial \kappa_{l,m}^{line}}{\partial \bar{T}_l} + \frac{\partial \kappa_{l,m}^{cont}}{\partial \bar{T}_l} \right) + \kappa_{l,m} \frac{\partial u_{l,m}}{\partial \bar{T}_l} \quad (\text{A.83})$$

Note that we are neglecting the dependence of the integrated path amounts in layers  $k$  where  $k > l$  on  $\bar{T}_l$ , which is small, but may need further study.

#### A3.4.5.1 Partial of line absorption with respect to temperature $\frac{\partial \kappa_{l,m}^{line}}{\partial \bar{T}_l}$

Line absorption coefficients are determined by a 3-point Lagrange interpolation in temperature, with  $\kappa_{l,m}^{line} = \sum_{i=0}^2 c_i(\bar{T}_l) \kappa_{i,(l,m)}$  where  $\kappa_{i,(l,m)}$  is the absorption coefficient tabulated at temperature  $T_i$ , in layer  $l$  for species  $m$ . Lagrange interpolation gives

$$c_i(x) = \frac{(x - x_0) \dots (x - x_{i-1})(x - x_{i+1}) \dots (x - x_n)}{(x_i - x_0) \dots (x_i - x_{i-1})(x_i - x_{i+1}) \dots (x_i - x_n)} \text{ and for 3-point interpolation, we have}$$

$$c_0(\bar{T}_l) = \left[ (T_1 - T_2) \bar{T}_l^2 + (T_2^2 - T_1^2) \bar{T}_l + (T_1^2 T_2 - T_1 T_2^2) \right] / D$$

$$c_1(\bar{T}_l) = \left[ (T_2 - T_0) \bar{T}_l^2 + (T_0^2 - T_2^2) \bar{T}_l + (T_2^2 T_0 - T_2 T_0^2) \right] / D$$

$$c_2(\bar{T}_l) = \left[ (T_0 - T_1) \bar{T}_l^2 + (T_1^2 - T_0^2) \bar{T}_l + (T_0^2 T_1 - T_0 T_1^2) \right] / D$$

where  $D$  is the common denominator:  $D = T_0^2(T_1 - T_2) + T_1^2(T_2 - T_0) + T_2^2(T_0 - T_1)$

The temperature partials are then

$$\frac{\partial \kappa_{l,m}^{line}}{\partial \bar{T}_l} = \sum_{i=0}^2 \frac{\partial c_i}{\partial \bar{T}_l} \kappa_{i,(l,m)} \quad (\text{A.84})$$

where

$$\begin{aligned} \frac{\partial c_0}{\partial \bar{T}_l} &= \left[ 2(T_1 - T_2) \bar{T}_l + (T_2^2 - T_1^2) \right] / D \\ \frac{\partial c_1}{\partial \bar{T}_l} &= \left[ 2(T_2 - T_0) \bar{T}_l + (T_0^2 - T_2^2) \right] / D \\ \frac{\partial c_2}{\partial \bar{T}_l} &= \left[ 2(T_0 - T_1) \bar{T}_l + (T_1^2 - T_0^2) \right] / D \end{aligned} \quad (\text{A.85})$$

A3.4.5.2 Partial of continuum absorption with respect to temperature  $\frac{\partial \kappa_{l,m}^{cont}}{\partial T_l}$

For species  $m$ , ( $m=H_2O, CO_2, N_2, O_2$ ), the CKD v3.0 continuum model (see section 3.3.8.4 and references therein) has tabulated coefficients for use in the following expression for continuum absorption:

$$\kappa_{l,m}^{cont}(\nu, \bar{T}_l, \bar{P}_l) = R(\nu, \bar{T}_l) C_m(\nu, \bar{T}_l, \bar{P}_l) \quad \text{where} \quad R(\nu, \bar{T}_l) = \nu \tanh\left(\frac{hc\nu}{2k_B \bar{T}_l}\right) \quad (\text{A.86})$$

For any  $m$ ,

$$\frac{\partial \kappa_{l,m}^{cont}}{\partial T_l} = \frac{\partial R}{\partial T_l} C_m + R \frac{\partial C_m}{\partial T_l} \quad (\text{A.87})$$

and

$$\frac{\partial R}{\partial T_l} = \frac{hc}{2k_B \bar{T}_l^2} (R^2 - \nu^2) \quad (\text{A.88})$$

A3.4.5.2.1 Temperature partials for water vapor continuum coefficient  $\frac{\partial C_{H_2O}}{\partial T_l}$

For  $H_2O$ ,  $C_{H_2O} = \left( C_S(\bar{T}_l) \bar{q}_l + C_F(1 - \bar{q}_l) \right) \frac{\bar{P}_l T_o}{P_o \bar{T}_l}$  where  $P_o = 1013$  hPa,  $T_o = 296$  K and

$$C_S(\bar{T}_l) = C_{S_{296}} \left( \frac{C_{S_{260}}}{C_{S_{296}}} \right)^{T_{fac}} ; T_{fac} = \frac{\bar{T}_l - T_o}{260 - T_o} \quad \text{with temperature partial}$$

$$\frac{\partial C_{H_2O}}{\partial T_l} = -\frac{C_{H_2O}}{\bar{T}_l} + \bar{q}_l \frac{\bar{P}_l T_o}{P_o \bar{T}_l} \left( \frac{C_S \ln C_S}{260 - T_o} \right) \quad (\text{A.89})$$

A3.4.5.2.2 Temperature partials for carbon dioxide continuum coefficient  $\frac{\partial C_{CO_2}}{\partial T_l}$

For the  $CO_2$  continuum,  $C_{CO_2} = C_F \frac{\bar{P}_l T_o}{P_o \bar{T}_l}$  with temperature partial

$$\frac{\partial C_{CO_2}}{\partial T_l} = -\frac{C_{CO_2}}{\bar{T}_l} \quad (\text{A.90})$$

A3.4.5.2.3 Temperature partials for nitrogen continuum coefficient  $\frac{\partial C_{N_2}}{\partial T_l}$

For the N<sub>2</sub> continuum,  $C_{N_2} = C_F \frac{\bar{P}_l T_o}{P_o \bar{T}_l}$  with temperature partial \

$$\frac{\partial C_{N_2}}{\partial \bar{T}_l} = -\frac{C_{N_2}}{\bar{T}_l} \quad (\text{A.91})$$

A3.4.5.2.4 *Temperature partials for oxygen continuum coefficient*  $\frac{\partial C_{O_2}}{\partial \bar{T}_l}$

For the O<sub>2</sub> continuum,  $C_{O_2} = C_F \frac{\bar{P}_l}{P_o} \exp\left(C_1(\bar{T}_l - 220) + C_2(\bar{T}_l - 220)^2\right)$  with temperature partial

$$\frac{\partial C_{O_2}}{\partial \bar{T}_l} = C_{O_2} \left[ C_1 + 2C_2(\bar{T}_l - 220) \right] \quad (\text{A.92})$$

A3.4.5.3 *Partials of layer integrated path amounts with respect to temperature*  $\frac{\partial u_{l,m}}{\partial \bar{T}_l}$

This term is only important in the tangent and next-to-tangent layers in the limb mode where neglecting the term results in about a 10% difference between analytic and finite difference jacobians for the TES detectors and about 25% difference for individual rays. It has a negligible

contribution to nadir temperature jacobians. An analytic expression for  $\frac{\partial u_{l,m}}{\partial \bar{T}_l}$  where  $u_{l,m}$  is

calculated in the ray-tracing module would be quite difficult given the dependence of density, altitude (*via* the hydrostatic equation) and index of refraction on temperature. We therefore propose a finite difference calculation using the ray-tracing algorithm only. Since this partial does not depend on frequency, this should not be too expensive computationally. Also, we will not need to compute this term for all layers in each limb ray, only those closest to and including the tangent layer. The necessary number of layers will be determined by prototyping the ray-tracing finite difference calculation for this term.

### **A3.4.6 Layer-to-Level Jacobians**

The frequency independent partials that relate layer average quantities to the parameters specified on and retrieved on levels must be computed in the same manner as the layer average quantities in the ray-tracing algorithm. Simpler approximations to this mapping, such as linear-in-in log pressure interpolation were found to be unacceptably inaccurate.

These jacobians have rather lengthy derivations, which are given in TES Algorithm & Science DFM #217 by H. Worden & S. Sund, July, 2001. Only the results of the derivations will be repeated here. Following equation (A.54), for both limb and nadir cases, we are interested in the following partials:

$$\frac{\partial \ln \bar{q}_{l,m}}{\partial \ln \bar{q}_{L,m}} \text{ and } \frac{\partial \ln \bar{q}_{l,m}}{\partial \ln \bar{q}_{U,m}}; \quad \frac{\partial \bar{T}_l}{\partial T_L} \text{ and } \frac{\partial \bar{T}_l}{\partial T_U}$$

where levels  $L$  (lower) and  $U$  (upper) bound layer  $l$ . For limb cases, path-weighted layer average quantities are computed using a sum over sub-layers, the number and size of which are determined dynamically, with the tangent layer having the most sub-layers. For nadir cases, given our relatively fine forward model pressure grid, it is sufficient to use single layers (*i.e.*, no sub-layers) to compute the path-weighted layer average quantities.

#### A3.4.6.1 Limb layer-to-level VMR Jacobians

The layer vmr,  $\bar{q}_{l,m}$ , for species  $m$  is the integrated species amount divided by the total path amount  $u_l$ :

$$\bar{q}_{l,m} = \frac{H_{\rho,m}}{u_l} \sum_{i=L}^{U-1} \frac{\Delta s_i}{\Delta r_i} (\rho_{i,m} - \rho_{i+1,m}) \quad (\text{A.93})$$

where  $H_{\rho,m}$  is the species density scale height:  $H_{\rho,m} = -\frac{r_U - r_L}{\ln\left(\alpha \frac{q_{U,m}}{q_{L,m}}\right)}$  with  $\alpha = \frac{\rho_U}{\rho_L} = \frac{P_U/T_U}{P_L/T_L}$  and

spherical layer upper and lower radii  $r_U$  and  $r_L$ .  $\frac{\Delta s_i}{\Delta r_i}$  is the ratio of line-of-sight distance through sub-layer  $i$  over sub-layer height, and the sub-layer species density is given by:

$$\rho_{i,m} = \rho_{L,m} \exp\left(-\frac{r_i - r_L}{H_{\rho,m}}\right).$$

The layer-to-level VMR jacobians are:

$$\frac{\partial \ln \bar{q}_{l,m}}{\partial \ln q_{L,m}} = \frac{H_{\rho,m}}{q_{l,m} u_l} \left[ \sum_{i=L}^{U-1} \frac{\Delta s_i}{\Delta r_i} \left\{ \rho_{i,m} \left( \frac{r_U - r_i}{r_U - r_L} \right) - \rho_{i+1,m} \left( \frac{r_U - r_{i+1}}{r_U - r_L} \right) \right\} \right] + \frac{1}{\ln\left(\alpha \frac{q_{U,m}}{q_{L,m}}\right)} \quad (\text{A.94})$$

$$\frac{\partial \ln \bar{q}_{l,m}}{\partial \ln q_{U,m}} = \frac{H_{\rho,m}}{q_{l,m} u_l} \left[ \sum_{i=L}^{U-1} \frac{\Delta s_i}{\Delta r_i} \left\{ \rho_{i,m} \left( \frac{r_i - r_L}{r_U - r_L} \right) - \rho_{i+1,m} \left( \frac{r_{i+1} - r_L}{r_U - r_L} \right) \right\} \right] - \frac{1}{\ln\left(\alpha \frac{q_{U,m}}{q_{L,m}}\right)} \quad (\text{A.95})$$

It is easily verified that equation (A.94) and (A.95) add to 1, which they must in order to have

$$\bar{q}_{l,m} = \frac{\partial \bar{q}_{l,m}}{\partial q_L} q_L + \frac{\partial \bar{q}_{l,m}}{\partial q_U} q_U = \frac{\bar{q}_{l,m}}{q_L} \left( \frac{\partial \ln \bar{q}_{l,m}}{\partial \ln q_L} \right) q_L + \frac{\bar{q}_{l,m}}{q_U} \left( \frac{\partial \ln \bar{q}_{l,m}}{\partial \ln q_U} \right) q_U$$

#### A3.4.6.2 Limb layer-to-level Temperature Jacobians

The layer temperature,  $\bar{T}_l$ , is given by:

$$\bar{T}_l = \frac{H_p}{k_B u_l} \sum_{i=L}^{U-1} \frac{\Delta s_i}{\Delta r_i} (P_i - P_{i+1}) \quad (\text{A.96})$$

with pressure scale height  $H_p = -\frac{r_U - r_L}{\ln(P_U/P_L)}$  and sub-layer pressure given by

$P_i = P_L \exp\left(-\frac{r_i - r_L}{H_p}\right)$ . The dependence on  $T_U$  and  $T_L$  is in the expression for  $u_l$ , where

$$u_l = H_p \sum_{i=L}^{U-1} \frac{\Delta s_i}{\Delta r_i} (\rho_i - \rho_{i+1}) \quad \text{with} \quad H_p = -\frac{r_U - r_L}{\alpha} \quad \text{and} \quad \rho_i = \frac{P_L}{k_B T_L} \exp\left(-\frac{r_i - r_L}{H_p}\right).$$

Recall that  $\alpha = \frac{P_U/T_U}{P_L/T_L}$ .

The layer-to-level temperature jacobians are:

$$\frac{\partial \bar{T}_l}{\partial T_L} = \frac{\bar{T}_l}{T_L} \left( \frac{H_p}{u_l} \left[ \sum_{i=L}^{U-1} \frac{\Delta s_i}{\Delta r_i} \left\{ \rho_i \left( \frac{r_U - r_i}{r_U - r_L} \right) - \rho_{i+1} \left( \frac{r_U - r_{i+1}}{r_U - r_L} \right) \right\} \right] + \frac{1}{\ln \alpha} \right) \quad (\text{A.97})$$

$$\frac{\partial \bar{T}_l}{\partial T_U} = \frac{\bar{T}_l}{T_U} \left( \frac{H_p}{u_l} \left[ \sum_{i=L}^{U-1} \frac{\Delta s_i}{\Delta r_i} \left\{ \rho_i \left( \frac{r_i - r_L}{r_U - r_L} \right) - \rho_{i+1} \left( \frac{r_{i+1} - r_L}{r_U - r_L} \right) \right\} \right] - \frac{1}{\ln \alpha} \right) \quad (\text{A.98})$$

It is easily verified that  $\frac{\partial \bar{T}_l}{\partial T_U} T_U + \frac{\partial \bar{T}_l}{\partial T_L} T_L = \bar{T}_l$ .

#### A3.4.6.3 Nadir layer-to-level VMR Jacobians

When sub-layers are not applied, the layer average quantities reduce to simpler expressions. We then have layer-to-level VMR jacobians:

$$\frac{\partial \ln \bar{q}_{l,m}}{\partial \ln q_{L,m}} = \frac{q_{L,m}}{q_{L,m} - \alpha q_{U,m}} + \frac{1}{\ln\left(\alpha \frac{q_{U,m}}{q_{L,m}}\right)} \quad (\text{A.99})$$

$$\frac{\partial \ln \bar{q}_{l,m}}{\partial \ln q_{U,m}} = \frac{-\alpha q_{U,m}}{q_{L,m} - \alpha q_{U,m}} - \frac{1}{\ln\left(\alpha \frac{q_{U,m}}{q_{L,m}}\right)} \quad (\text{A.100})$$

#### A3.4.6.4 Nadir layer-to-level Temperature Jacobians

Likewise, the layer average temperature expression becomes simpler and the layer-to-level temperature jacobians are:

$$\frac{\partial \bar{T}_l}{\partial T_L} = \frac{\bar{T}_l}{T_L} \left[ \frac{1}{\ln \alpha} + \frac{1}{1 - \alpha} \right] \quad (\text{A.101})$$

$$\frac{\partial \bar{T}_l}{\partial T_U} = \frac{\bar{T}_l}{T_U} \left[ \frac{-1}{\ln \alpha} - \frac{\alpha}{1 - \alpha} \right] \quad (\text{A.102})$$

### A3.4.7 Pointing Jacobians

The field of view integration for the radiance measured with detector  $d$ , from section 3.3.6 is given by

$$L_{sat}(\theta_d) = \sum_{j=0}^{N_{FOV}} L(\theta_j) \mathbf{R}_{FOV}(\theta_j - \theta_d) \Delta \theta_j \quad (\text{A.103})$$

Writing this as an integral,

$$L_{sat}(\theta_d) = \int_{\theta_{\min}}^{\theta_{\max}} L(\theta) \mathbf{R}_{FOV}(\theta - \theta_d) d\theta \quad (\text{A.104})$$

Since  $\frac{\partial \mathbf{R}_{FOV}}{\partial \theta_d} = -\frac{\partial \mathbf{R}_{FOV}}{\partial \theta}$ , we have

$$\frac{\partial L_{sat}}{\partial \theta_d} = \int_{\theta_{\min}}^{\theta_{\max}} L(\theta) \left( -\frac{\partial \mathbf{R}_{FOV}}{\partial \theta} \right) d\theta \quad (\text{A.105})$$

Integration by parts gives

$$\frac{\partial L_{sat}}{\partial \theta_d} = -L(\theta) \mathbf{R}_{FOV}(\theta - \theta_d) \Big|_{\theta_{\min}}^{\theta_{\max}} + \int_{\theta_{\min}}^{\theta_{\max}} \left( \frac{\partial L}{\partial \theta} \right) \mathbf{R}_{FOV}(\theta - \theta_d) d\theta \quad (\text{A.106})$$

Assuming we have chosen  $\theta_{\min}$  and  $\theta_{\max}$  to be angles where the detector response is negligible, the first term in equation (A.106) is zero. This leaves the second term, which we write as a sum:

$$\frac{\partial L_{sat}}{\partial \theta_d} = \sum_{j=0}^{N_{FOV}} \left( \frac{\partial L}{\partial \theta_j} \right) \mathbf{R}_{FOV}(\theta_j - \theta_d) \Delta \theta_j \quad (\text{A.107})$$

This now has the same form as equation (A.103) with  $L(\theta_j)$  replaced by  $\frac{\partial L}{\partial \theta_j}$ . The  $\frac{\partial L_{sat}}{\partial \theta_d}$  partials

are then computed in the same way we compute detector radiances, with the switch to ray indices as described in section 3.3.6.

For 4-point Lagrange interpolation,  $L(\theta_j) = \sum_{m=-1}^2 a_{j,m} L(\theta_{k+m})$  and we have

$$\frac{\partial L}{\partial \theta_j} = \sum_{m=-1}^2 \frac{\partial a_{j,m}}{\partial \theta_j} L(\theta_{k+m}) \quad (\text{A.108})$$

Since the interpolation coefficients are defined with respect to the variable  $p$ , with  $p = \frac{\theta_j - \theta_k}{\theta_{k+1} - \theta_k}$ , we have

$$\frac{\partial a_{j,m}}{\partial \theta_j} = \frac{\partial a_{j,m}}{\partial p} \frac{\partial p}{\partial \theta_j} = \frac{\partial a_{j,m}}{\partial p} \left( \frac{1}{\theta_{k+1} - \theta_k} \right) \quad (\text{A.109})$$

where

$$\begin{aligned} \frac{\partial a_{j,-1}}{\partial p} &= (-1 + 4p - 3p^2) / (1 + c_1) \\ \frac{\partial a_{j,0}}{\partial p} &= 6p(p-1) + p(2-3p) / (1 + c_2) \\ \frac{\partial a_{j,1}}{\partial p} &= 6p(1-p) + (1-4p+3p^2) / (1 + c_1) \\ \frac{\partial a_{j,2}}{\partial p} &= (3p^2 - 2p) / (1 + c_2) \end{aligned} \quad (\text{A.110})$$

with  $c_1 = (\theta_k - \theta_{k-1}) / (\theta_{k+1} - \theta_k)$  and  $c_2 = (\theta_{k+2} - \theta_{k+1}) / (\theta_{k+1} - \theta_k)$ .

As noted above, these partials of the interpolation coefficients are then propagated along with the interpolation coefficients to obtain both detector radiances and pointing jacobians.

### **A3.4.8 Jacobian Validation**

**\*\*\*NOTE: THIS SECTION IS UNDER CONSTRUCTION\*\*\***

We validate our analytic jacobians by comparing to jacobians computed by the finite difference (FD) method described in section 3.4.1.

A3.4.8.1 Nadir Jacobian Validation

**Table A-3: Nadir jacobian comparisons: Finite Difference (FD) to Analytic**

Retrieved Parameter	Frequency Range (cm <sup>-1</sup> )	Max FD value	Max  FD-Analytic	RMS  FD-Analytic
Temperature at 619 mb	760-785	2.37e-08	1.1e-10	2.0e-11
H <sub>2</sub> O at 750 mb	1202-1214	1.80e-07	4.8e-09	8.7e-10

**Figure A-10:**

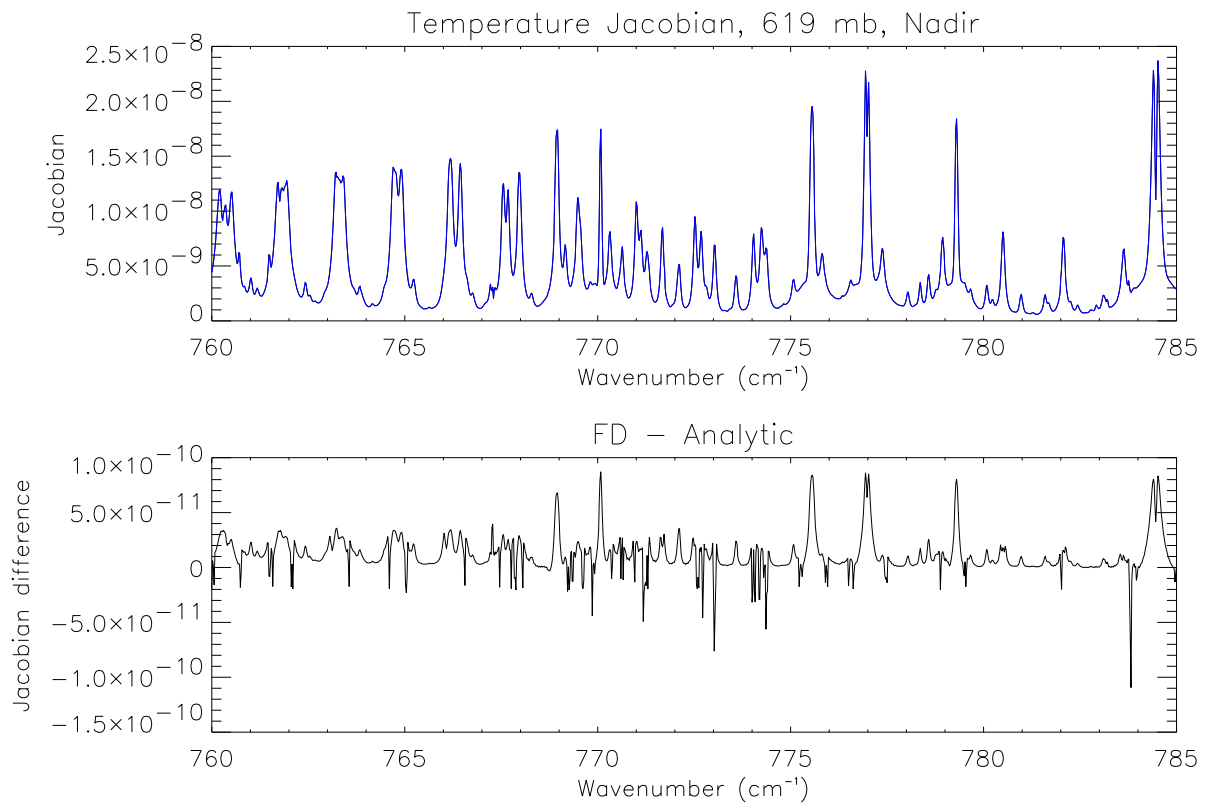
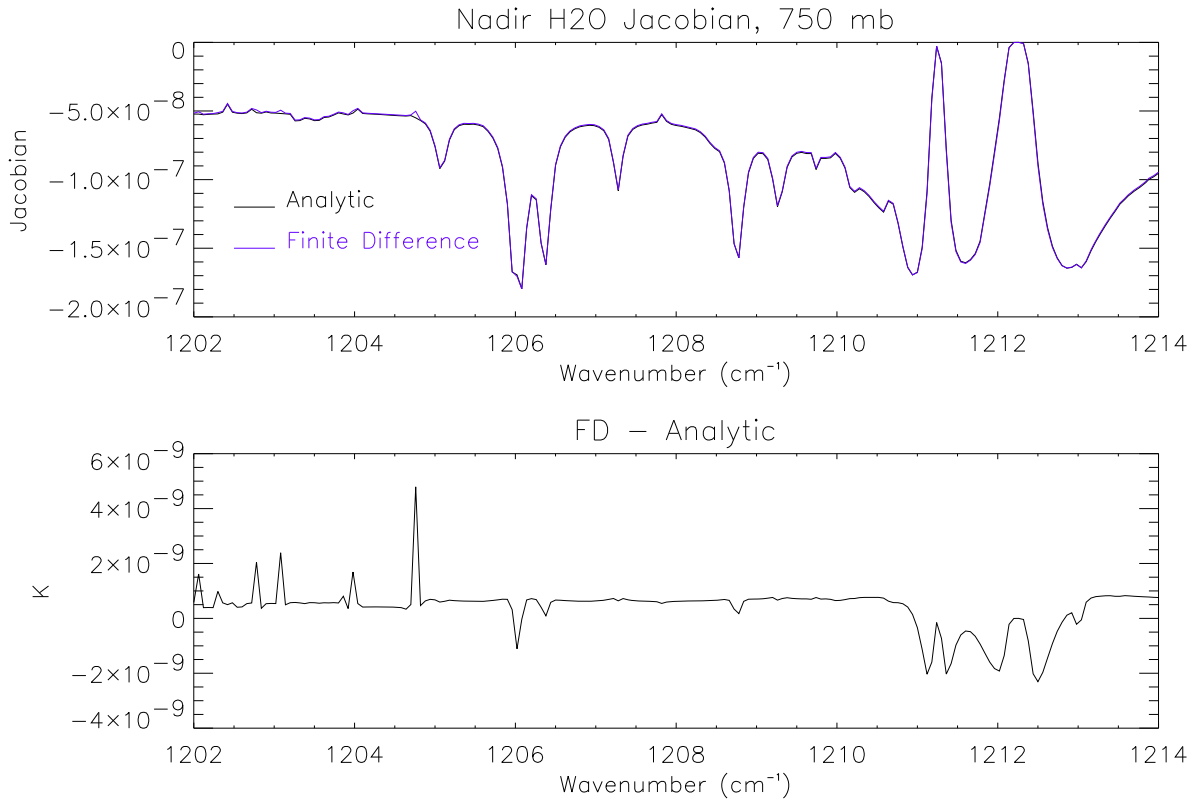


Figure A-11:

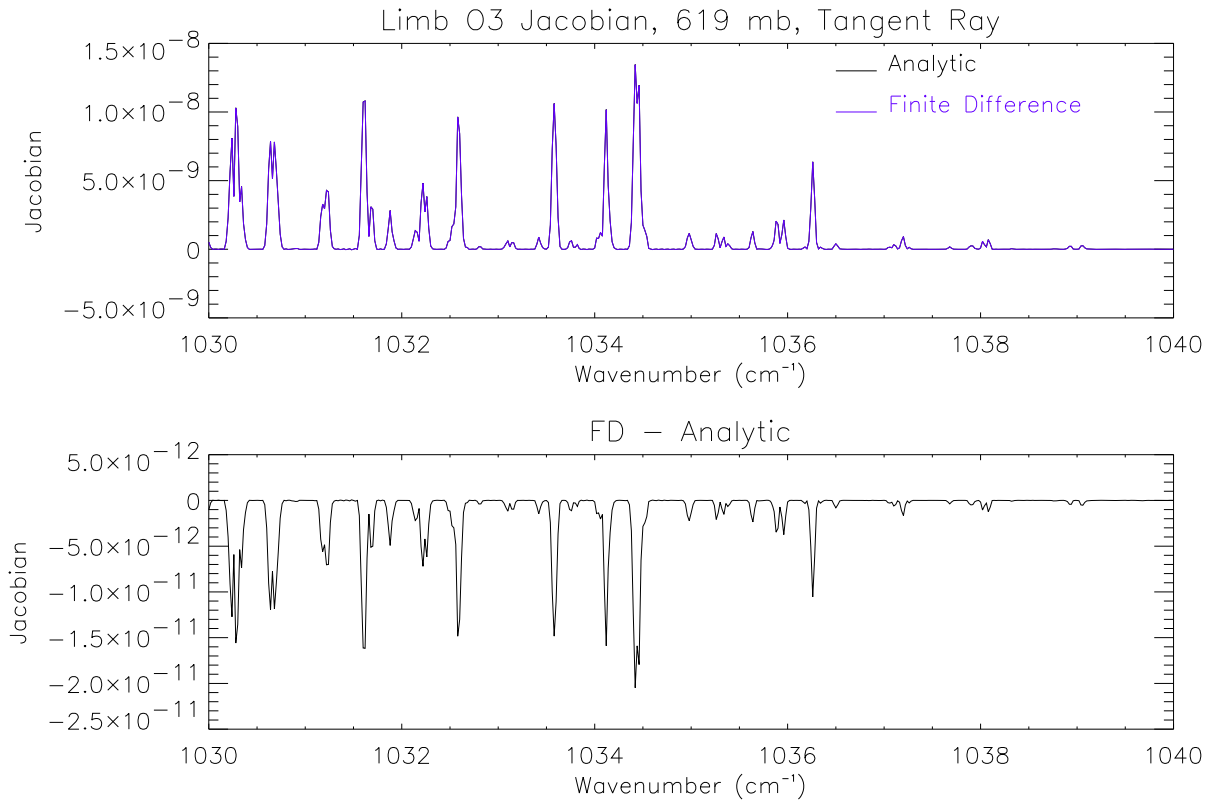


A3.4.8.2 Limb Jacobian Validation

TableA- 4: Limb jacobian comparisons: Finite Difference (FD) to Analytic

Retrieved Parameter	Frequency Range (cm <sup>-1</sup> )	Limb Ray Tangent Pressure	Max FD value	Max  FD-Analytic	RMS  FD-Analytic
O <sub>3</sub> at 619 mb	1030-1040	1000 mb	2.71e-08	3.6e-11	6.4e-12
		909 mb	2.47e-08	3.0e-11	5.6e-12
		825 mb	2.20e-08	2.1e-11	4.6e-12
		750 mb	1.78e-08	1.7e-11	3.8e-12
		681 mb	6.79e-09	6.0e-12	1.2e-12
		619 mb	1.34e-08	2.0e-11	3.3e-12
H <sub>2</sub> O at 750 mb	1204-1214	1000 mb	2.06e-07	1.2e-09	5.8e-10
		909 mb	2.02e-07	3.3e-10	1.3e-10
		825 mb	1.08e-07	1.7e-10	1.0e-10
		750 mb	4.61e-07	6.4e-10	2.2e-10

Figure A-12:



### A3.5.1 Retrieval Strategy

This appendix gives descriptions of the retrieval strategy suppliers listed in section 3.5.1.2 and 3.5.1.3.

#### Target level suppliers:

##### *Strategy Table.*

Strategy table parameters are read and organized so that strategy table information is easily accessed by the other suppliers.

##### *Surface pressure.*

If the level 1b cloud flag indicates low intrapixel variability, the scene may be either cloud free or cloud filled. To distinguish between cloud free or cloud filled, the difference between the surface temperature and the brightness temperature in a particular part of the spectrum will be calculated, which may require a RT calculation to account for transmission through the water vapor continuum (See also the pixel categorization section, 3.5.5 for nadir, or 3.5.6 for limb). (1) If this difference is small, the scene is considered clear; the surface pressure is calculated at the surface altitude (an input) using the hydrostatic equation and the sea surface pressure, lowest atmospheric temperature, and lowest atmospheric water values. (2) If this difference is large

and the intrapixel variability of BT11 is low, this will be identified as a retrievable cloud filled scene. BT11 will then be compared against the temperature profile to determine the pressure level of the new surface, which will have the emissivity of a cloud. Note: cloud height top may be determined by an adaptation of CO<sub>2</sub> slicing rather than a simple comparison of BT and the temperature profile.

### *Forward model pressure.*

Once the surface pressure has been determined, the FMPressure vector is created starting from the standard pressure grid: (1) Cut off the levels below the surface pressure on the standard pressure grid. (2) Add a level at the surface pressure. (3) Possibly remove the pressures adjacent to the surface pressure if they are too close (the current cutoff is .1%).

### *Sequence level full state vector (initial guess).*

Gather information for the initial state vector described in section 3.2.2. For each species, use one or multiple sources (specified in the strategy table) to create a single profile. For an atmospheric species: (1) interpolate from the pressure levels of the sources to FMPressures. (2) If the control parameter specifies it, project the initial guess to within the span of the retrieval vector using the maps created in the map supplier. (3) Also, have the capability of creating hybrid profiles using meteorological data and other specified parameters, for example interpolate from a profile to the meteorologically specified surface value.

### *True full state vector.*

This is only used for data simulation and error analysis of simulated data. The true full state needs all of the functionality of the Sequence Level Full State Vector and can use the same class as the Sequence Level Full State Vector, but with different sources provided by the strategy table.

### *Target level emissivity.*

Create a vector of emissivity vs. frequency. If there are no clouds, access the land cover database to determine the land cover types and amount of each type in the target scene footprint, and access the emissivity database to get the emissivity of the footprint based on the land cover types and amount of each type in the footprint. If there are clouds, get the cloud emissivity from a cloud database.

### *Target level map.*

Create maps from retrieval parameters to forward model levels and vice versa. (see section 3.5.2.1). Calculate (from retrieval levels) or read in a map and inverse map for each atmospheric species in all steps. If maps are read in, they will be on the standard pressure grid and must be modified to the FMPressures grid. Although conceptually this is a step-level supplier, the maps are needed for projecting the initial guess before the first step. See section 3.5.2.1 for a more detailed description of mapping)

### *Simulated spectrum.*

Simulates radiance data using the true state. This is only used for data simulation. The output data is formatted exactly like real data.

### *Measured spectrum.*

Average spectra information (for scans and pixels, nadir only) and RMS the noise over pixels and scan, depending on the view mode (nadir vs. limb) and control information (bad pixel or bad scan information).

### *Target level Microwindows definitions.*

Access a database of microwindow ranges to select the correct list of microwindows for each step or combined microwindows for all steps. The database of microwindows are arranged by retrieval species and view mode, and may be arranged by location or season. For each microwindow, it must also get the list of forward model species, filter, and detector mask (occupation matrix). Although conceptually this is a step-level supplier, all the microwindows are needed for simulating data, if data is simulated on an as-needed basis.

### **Step level suppliers:**

#### *Step level map.*

Get maps for this step for all atmospheric species from the Target Level Map Supplier.

#### *Step level Microwindows definitions.*

Get relevant information from Target Level Microwindows Definitions Supplier for this step.

#### *A priori $x_a$ .*

This supplier has the same requirements as the Target level full state supplier, with different source instances. It must also map to the retrieval parameters in the case of an atmospheric species. It must get have access to the results of the emissivity supplier to get the retrieval parameters for emissivity.

#### *A priori constraint.*

Create the full constraint matrix (which is square with dimension = # retrieval parameters) as described in section 3.5.3.

#### *A priori covariance.*

Create the full covariance matrix (which is square with dimension = # retrieval parameters) to be used in error analysis as described in section 3.5.9.

#### *Microwindows radiances.*

Pick out the radiances in the given microwindows. Use the noise vector to deweight particular frequencies with the occupation matrix. Provides the radiances and noise for the retrieval microwindows in this step.

### *Emissivity a priori.*

Select the emissivity retrieval frequencies based on the microwindow information, results of the target level emissivity supplier, and control parameters. Create the constraint matrix and true covariance for emissivity similarly to the other constraint matrices but with perhaps different control parameters. Create the a priori vector of emissivity by selecting the initial guess values at the retrieval frequencies.

### *Step level full state vector.*

Get the information from the updated target level full state vector needed for the step level full state vector.

### *Retrieval levels.*

Access a database of retrieval levels to get the retrieval levels for the specified view mode, location, species, and maptype. The retrieval levels in the database are associated with the pressures in StandardPressureLevels and must be adjusted to the FMPressures by the following steps:

- (1) Remove levels outside of FMPressures.
- (2) Reindex levels so that the level corresponding to the lowest FMPressures is level 1.
- (3) Add or move levels so that there is always a retrieval level associated with the lowest and highest FMPressures. There is a threshold for when to add a new level versus move an existing level.

## REFERENCES

### **A3.3.1.1: Ray Tracing**

Allen, C.W., *Astrophysical Quantities*. Athlone Press, 1976.

Ciddor, P.E. Refractive index of air: new equations for the visible and near infrared. *Applied Optics*, 35, 1566-1573, 1996.

Edlén, B., The Refractive Index of Air, *Metrologia*, 2, 71-80, 1966.

Birch, K. P., and M. J. Downs, An Updated Edlén Equation for the Refractive Index of Air, *Metrologia*, 30, 155-162, 1993.

Birch, K. P., and M. J. Downs, Correction to the Updated Edlén Equation for the Refractive Index of Air, *Metrologia*, 31, 315-316, 1994.

Coleman, C. D., W. R. Bozman, and W. F. Meggers, *Table of Wavenumbers*, US Department of Commerce, NBS Monograph3, May, 1960.

### **A.3.1.5 Non-LTE**

Funke, B. and M. Lopez-Puertas, Nonlocal thermodynamic equilibrium vibrational, rotational, and spin state distribution of NO(v=0,1,2) under quiescent atmospheric conditions, *J. Geophys. Res.*, 105, 4409-4426, 2000.

### **A3.3.2.3: Global Land Cover Characteristics Data Base**

Anderson, J.R., E.E. Hardy, J.T. Roach and R.E. Witmer, A land use and land cover classification system for use with remote sensor data, *U.S. Geological Survey Professional Paper 964*, 28, 1976.

Belward, A.S., ed., The IGBP-DIS global 1 km land cover data set (DISCover)-proposal and implementation plans, *IGBP-DIS Working Paper No. 13*, Toulouse, France, 1996.

Brown, J.F., T.R. Loveland, J.W. Merchant, B.C. Reed, and D.O. Ohlen, Using multisource data in global land cover characterization: concepts, requirements and methods, *Photogrammetric Engineering and Remote Sensing*, 59, 977-987, 1993.

Brown, J.F., B.C Reed, and L. Huewe, Advanced strategy for multi-source analysis and visualization in land cover characterization, *Proceedings, Pecora 13, Human Interactions with the Environment: Perspectives From Space*, in press.

Loveland, T.R., J.W. Merchant, J.F. Brown, D.O., Ohlen, B.C. Reed, P. Olson, and J. Hutchinson, Seasonal land-cover regions of the United States, *Annals of the Association of American Geographers*, 85, 2, 339-355, 1995.

Loveland, T.R., J.W. Merchant, D.O. Ohlen, and J.F. Brown, Development of a land-cover characteristics database for the conterminous U.S., *Photogrammetric Engineering and Remote Sensing*, 57, 11, 1453-1463, 1991.

Loveland, T.R., D.O. Ohlen, J.F. Brown, B.C. Reed, Z. Zhu, J.W. Merchant, and L. Yang, Western hemisphere land cover-progress toward a global land cover characteristics database, *Proceedings, Pecora 13, Human Interventions with the Environment: Perspectives From Space*, in press.

Olson, J.S., 1994a, *Global ecosystem framework-definitions*, USGS EROS Data Center Internal Report, Sioux Falls, SD, 1994.

Olson, J.S., 1994b, *Global ecosystem framework-translation strategy*, USGS EROS Data Center Internal Report, Sioux Falls, SD, 1994.

Zhu, Z., and L. Yang, Characteristics of the 1-km AVHRR data set for North America, *International Journal of Remote Sensing*, 17, 1915-1924, 1996.

### **A3.3.8.1: ABSCO DATABASES: Line Parameters**

Arlander, D. W., Barbe, A., Bourgeois, M. T., Hamdouni, A., Flaud, J.-M., Camy-Peyret, C. and Demoulin, Ph., The identification of  $^{16}\text{O}^{18}\text{O}^{16}\text{O}$  and  $^{16}\text{O}^{16}\text{O}^{18}\text{O}$  ozone isotopes in high resolution

ground-based FTIR spectra, *Journal of Quantitative Spectroscopy & Radiative Transfer*, 52, 267-271, 1994.

Birk, M. and G. Wagner, A new spectroscopic database for chlorine nitrate, poster session 2, Sixth Biennial HITRAN Database Conference, Harvard-Smithsonian Center for Astrophysics, Cambridge, MA, 19-21 June 2000.

Brown, L. R.; Gunson, M. R.; Toth, R. A.; Irion, F. W.; Rinsland, C. P.; and Goldman, A.: The 1995 Atmospheric Trace Molecule Spectroscopy (ATMOS) Linelist. *Appl. Opt.*, 35, 2828-2848, 1996.

Chackerian, C. and R. Freedman, New Electric Dipole Moment Function for CO and Update of HITRAN CO Line Intensities, poster presentation, Workshop on laboratory spectroscopic needs for atmospheric sensing, San Diego, CA, 2001.

Cleveau, C.; Camy-Peyret, C.; Valentin, A. and Flaud, J.-F.: Absolute intensities of the  $\nu_1$  and  $\nu_3$  bands of  $^{16}\text{O}_3$ , *J. Mol. Spectrosc.*, 206, 115-125, 2001.

Dana, V.; Mandin, J.-Y.; Allout, M.-Y.; Perrin, A.; Régalia, L.; Barbe, A.; Plateaux, J.-J.; and Thomas, X.: Broadening parameters of  $\text{NO}_2$  Lines in the 3.4  $\mu\text{m}$  Spectral Region, *J. Quant. Spectrosc. Radiat. Transfer*, 57, 445-457, 1997.

Daumont, L.; Vander Auwera, J.; Teffo, J.-L.; Perevalov, V. I.; and Tashkun, S. A.: Line intensity measurements in  $^{14}\text{N}_2^{16}\text{O}$  and their treatment using the effective dipole moment approach. *J. Mol. Spectrosc.*, 208, 281-291, 2001.

Flaud, J.-M.; Camy-Peyret, C.; A. Mahmoudi, and Guelachvili, G.: The  $\nu_2$  band of  $\text{HD}^{16}\text{O}$ , *Internat. J. Infrared and Millimeter Waves*, 7, 1063-1090, 1986.

Flaud, J.-M.; Bougeois, M. T.; Barbe, A.; Plateaux, J. J.; and Camy-Peyret, C.: The  $\nu_1 + \nu_3$  bands of  $^{16}\text{O}^{18}\text{O}^{16}\text{O}$  and  $^{16}\text{O}^{16}\text{O}^{18}\text{O}$ , *J. Molec. Spectrosc.*, 165, 464-469, 1994.

Goldman, A.; Schoenfeld, W.G.; Stephen, T. M.; Murcray, F. J.; Rinsland, C.P.; Barbe, A.; Hamdouni, A.; Flaud, J.-M.; and Camy-Peyret, C.: Isotopic ozone in the 5  $\mu\text{m}$  Region from High Resolution Balloon-Borne and Ground-Based FTIR Solar Spectra. *J. Quant. Spectrosc. Radiative Transfer* 59, 231-244, 1998.

Goldman, A.; Coffey, M. T.; Stephen, T. M.; Rinsland, C. P.; Mankin, W. G. and Hannigan, J. W.: Isotopic OCS from high-resolution balloon-borne and ground-based infrared solar absorption spectra. *J. Quant. Spectrosc. Radiative Transfer*, 67, 447-455, 2000.

Heyart, M.; Perrin, A.; Flaud, J.-M.; Camy-Peyret, C.; Rinsland, C. P.; Smith, M. A. H.; and Malathy Devi, V., The  $\nu_1$  and  $\nu_3$  bands of  $^{16}\text{O}^{17}\text{O}^{16}\text{O}$  line positions and intensities, *J. Molec. Spectrosc.*, 156, 210-216, 1992.

Heyart, M., Perrin, A., Flaud, J.-M., Camy-Peyret, C., Rinsland, C. P., Smith, M. A. H. and Malathy Devi, V., The hybrid-type bands  $\nu_1$  and  $\nu_3$  of  $^{16}\text{O}^{16}\text{O}^{17}\text{O}$  line positions and intensities, *J. Molec. Spectrosc.*, 157, 524-531, 1993.

Jacquinet-Husson, N., et al., The 1997 spectroscopic GEISA databank. *J. Quant. Spectrosc. Radiative Transfer*, 62, 205-254, 1999.

Jacquinet-Husson, N.; Scott, N.; Chédin, A.; and Chursin, A.: The current Geisa spectroscopic database system and Its Evolution. 6<sup>th</sup> Biennial HITRAN database conference, Harvard-Smithsonian Center for Astrophysics, Cambridge, MA 2000.

Maté, B.; Lugez, C. L.; Solodov, A. M.; Fraser, G. T.; and Lafferty, W. J.: Investigation of the Collision-induced absorption by  $\text{O}_2$  near 6.4  $\mu\text{m}$  in pure  $\text{O}_2$  and  $\text{O}_2/\text{N}_2$  mixtures. *J. Geophys. Res.* 105 22,225-22,230, 2000.

Malathy Devi, V.; Benner, D. C.; Rinsland, C. P.; Smith, M. A. H.; and Parmar, D. S.: Infrared Spectroscopy of the  $\text{CO}_2$  Molecule: *Research Signpost: Recent Research Developments in Geophysical Research*, Vol. 1, pp. 119-148, S. G. Pandalai, editor, 1997.

Malathy Devi, V.; Benner, D. C.; Rinsland, C. P.; and Smith, M. A. H.: Absolute Rovibrational Intensities of  $^{12}\text{C}^{16}\text{O}_2$  Absorption Bands in the 3090 to 3800- $\text{cm}^{-1}$  Spectral Region. *J. Quant. Spectrosc. Radiat. Transfer*, 60, 741-770, 1998a.

Malathy Devi, V.; Benner, D. C.; Smith, M. A. H.; and Rinsland, C. P.: Pressure-Broadening and Pressure Shift Coefficients in the  $2\nu_2^0$  and  $\nu_1$  Bands of  $^{16}\text{O}^{13}\text{C}^{18}\text{O}$ . *J. Quant. Spectrosc. Radiat. Transfer*, 60, 771-783, 1998b.

Malathy Devi, V.; Benner, D. C.; Smith, M. A. H.; and Rinsland, C. P.: Air- and  $\text{N}_2$  Broadening Coefficients and Pressure-shift Coefficients in the  $^{12}\text{C}^{16}\text{O}_2$  Laser Bands. *J. Quant. Spectrosc. Radiat. Transfer*, 59, 137-150, 1998c.

Malathy Devi, V., Benner, D.C. Smith, M.A.H., Rinsland, C.P., and Dulick, M., Pressure-broadening and Pressure-Shift Coefficients in the  $^{12}\text{C}^{16}\text{O}_2$  and  $^{13}\text{C}^{16}\text{O}_2$  Laser Bands, *J. Mol. Spectrosc.*, in preparation, 2002.

Moyer, M. J.; Irion, F. W.; Gunson, M. R.; Rinsland, C. P.; Yung, Y. L.; and Gunson, M. R.: ATMOS stratospheric deuterated water and implications for tropospheric stratospheric exchange, *J. Geophys. Res. Lett.*, 23, 2385-2388, 1996.

Miller, C., High-resolution spectroscopy of  $\text{CO}_2$  in the 4500- to 8000- $\text{cm}^{-1}$  region, poster presentation, Workshop on laboratory spectroscopic needs for atmospheric sensing, San Diego, CA, 2001.

Perrin, A.; Flaud, J.-M.; Goldman, A.; Camy-Peyret, C.; Lafferty, W. J.; Arcas, Ph.; and Rinsland, C.P.:  $\text{NO}_2$  and  $\text{SO}_2$  Line Parameters: 1996 HITRAN update and New Results, *J. Quant. Spectrosc. Radiat. Transfer*, 60, 839-850, 1998.

Perrin, A.; Rinsland, C. P. and Goldman, A.: Spectral parameters for the  $\nu_6$  Region of HCOOH and its measurement in the infrared tropospheric spectrum, *J. Geophys. Res.*, *104*, 18,661-18,666, 1999.

Perrin, A.; Orphal, J., Flaud, J.-M.; Himmelmann, S.; Voigt, S.; Burrows, J.P.; Stephen, T. M. Goldman, A.; and Rinsland, C. P.: Recent Progress Achieved in the 6.2  $\mu\text{m}$  Region for Nitrogen Dioxide. 6<sup>th</sup> Biennial HITRAN database conference, poster P22, Harvard-Smithsonian Center for Astrophysics, Cambridge, MA 2000.

Perrin, A., Flaud, J.-M.; Keller, F.; Goldman, A.; Blatherwick, R. D.; Murcray, F. J.; and Rinsland, C. P.: New analysis of the  $\nu_8 + \nu_9$  band of HNO<sub>3</sub>: Line positions and intensities, *J. Molec. Spectrosc.*, *194*, 113-123, , 1999.

Perrin, A., J.-M.; Flaud, J.-M.; Keller, F.; Smith, M. A. H.; Rinsland, C. P. Malathy Devi, V.; Benner, D. C.; Stephen, T. M.; and Goldman, A.; The  $\nu_1 + \nu_3$  bands of <sup>16</sup>O<sup>17</sup>O<sup>16</sup>O and <sup>16</sup>O<sup>16</sup>O<sup>17</sup>O isotopomers of ozone, *J. Mol. Spectrosc.*, *207*, 54-59 , 2001.

Pine, A. S., and C. P. Rinsland, The role of torsional hot bands in modeling atmospheric ethane, 53rd International Symposium on Molecular Spectroscopy Symposium, Columbus, OH, paper TF17, 1998.

Orlando, J.; Tyndall, G. S.; Nickerson, K.; and Calvert, J. G.: The Temperature Dependence of Collision-Induced Absorption by Oxygen near 6  $\mu\text{m}$ . *J. Geophys. Res.* *96*, 20,775-20,760, 1991.

Rinsland, C. P.; Flaud, J.-M.; Goldman, A.; Perrin, A.; Camy-Peyret, C.; Smith, M. A. H.; Malathy Devi, V.; Benner, D. C.; Barbe, A.; Stephen, T. M.; and Murcray, F. J.: Spectroscopic Parameters for Ozone and Its Isotopes: Current Status, Prospects for Improvement, and the Identification of <sup>16</sup>O<sup>16</sup>O<sup>17</sup>O and <sup>16</sup>O<sup>17</sup>O<sup>16</sup>O Lines in Infrared Ground-Based and Stratospheric Solar Absorption Spectra. *J. Quant. Spectrosc. Radiat. Transfer*, *60*, 803-814, 1998a.

Rinsland, C. P.; Gunson, M. R.; Wang, P.-H.; Arduini, R. F.; Baum, B. A. Minnis, P.; Goldman, A.; Abrams, M. C.; Zander, R.; Mahieu, E.; Salawitch, R. J.; Michelsen, H. A.; Irion, F. W.; and Newchurch, M. J.: ATMOS-ATLAS-3 Infrared Profile Measurements of Trace Gases in the November 1994 Tropical and Subtropical Upper Troposphere, *J. Quant. Spectrosc. Radiat. Transfer*, *60*, 803-814, 1998b.

Rinsland, C. P.; Jones, N. B.; Connor, B. J.; Logan, J. A.; Pougatchev, N. S.; Goldman, A.; Murcray, F. J.; Stephen, T. M.; Pine, A. S.; Zander, R.; Mahieu, E.; and Demoulin, E.: Northern and Southern Hemisphere Ground-Based Infrared Spectroscopic Measurements of Tropospheric Carbon Monoxide and Ethane, *J. Geophys. Res.*, *103*, 28,197-28,218, 1998c.

Rothman, L. S.; Rinsland, C. P.; Goldman, A.; Massie, S. T.; Edwards, D. P.; Flaud, J.-M.; Perrin, A.; Camy-Peyret, C.; Dana, V., Mandin, J.-Y.; Schroeder, J.; McCann, A.; Gamache, R. R.; Wattson, R. B.; Yoshino, K.; Chance, K. V.; Jucks, K. W.; Brown, L. R.; Nemtchinov, V.; and Varanasi, P.: *J. Quant. Spectrosc. Radiat. Transfer*, *60*, 665-710, 1998.

Sen, B.; Toon, G. C.; Osterman, G. B.; Blavier, J.-F.; Margitan, J. J.; Salawitch, R. J.; and Yue, G. K. Measurements of reactive nitrogen in the stratosphere, *J. Geophys. Res.*, **103**, 3571-3585, 1998.

Smith, M. A. H.; Harvey, G. A.; Pellett, G. L.; Goldman, A.; and Richardson, D. J.: Measurements of the HCN  $\nu_3$  band broadened by N<sub>2</sub>. *J. Mol. Spectrosc.*, **105**, 105-112, 1984.  
Smith, M. A. H.; Malathy Devi, V.; Benner, D. C.; and Rinsland, C. P.: Absolute intensities of <sup>16</sup>O<sub>3</sub> lines in the 9-11  $\mu\text{m}$  region, *J. Geophys. Res.*, **106**, 9909-9921, 2001.

Toth, R. A.: Water vapor measurements between 590 and 2582  $\text{cm}^{-1}$ : Line Positions and Strengths. *J. Mol. Spectrosc.*, **190**, 379-396, 1998.

Thibault, F.; Menoux, V.; Doucen, R.; Rosenmann, L.; Hartmann, J.-M.; and Boulet, C.: Infrared collision-induced absorption by O<sub>2</sub> near 6.4  $\mu\text{m}$  for atmospheric applications: Measurements and empirical modeling. *Appl. Opt.* **36**, 563-567, 1997.

Toon, G. C., J.-F. Blavier, B. Sen, and B. J. Drouin, Atmospheric COCl<sub>2</sub> measured by solar occultation spectroscopy. *Geophys. Res. Lett.*, **28**, 2835-2838, 2001.

Wang, W. F., Ong, P. P.; Tan, T. L.; Looi, E. C.; and Teo, H. H., Infrared Analysis of the Anharmonic Resonance between  $\nu_8 + \nu_9$  and the Dark State  $\nu_6 + \nu_7$  of HNO<sub>3</sub>. *J. Mol. Spectrosc.* **183**, 407-412, 1997.

Worden, H., Beer, R.; Rinsland, C. P.: Airborne infrared spectroscopy of western wildfires, *J. Geophys. Res.*, **102**, 1287-1299, 1997.

Xu, L.-H.; Lees, R. M., Benchmark Laboratory Methanol Data at the University of New Brunswick, Canada. Session 4, Spectroscopic Parameters, 6<sup>th</sup> Biennial HITRAN database conference, Harvard-Smithsonian Center for Astrophysics, Cambridge, MA 2000.

LAST PAGE